AERODYNAMICS

A TIME DEPENDENT FLOW MODEL FOR THE INNER REGION OF A TURBULENT BOUNDARY LAYER

by

Ho-Chen Chien and V. A. Sandborn

Department of Civil Engineering
Colorado State University

April 1981

This research was carried out under the Naval Sea Systems Command General Hydromechanics Research Program Subproject SR 023 01 01, administered by the David W. Taylor Naval Ship Research and Development Center, Contract N00014-80-C-0183.

CER 80-81-HCC-VAS 45

ABSTRACT OF DISSERTATION

A TIME DEPENDENT FLOW MODEL FOR THE INNER REGION

OF A TURBULENT BOUNDARY LAYER

Response of the flow variables to external driving forces is non-linear for shear flows. For the turbulent boundary layer case, surface shear stress fluctuations of magnitude as great as the mean value are observed. For flow near the surface Prandtl's turbulent boundary layer approach of employing averaged Reynolds equation and a turbulence closure model is insufficient to account for surface shear fluctuations. A model which incorporates a discrete time dependent solution for the inner region of the turbulent boundary layer is proposed. The model requires stochastic averaging of the time dependent solution to account for the random aspect of the flow.

The physical model for the flow near the surface is based on the bursting cycle observed in the inner region of a turbulent boundary layer. Localized pressure gradients created in the valleys of the large scale structures of the outer region of the flow are assumed to be the origin of the bursting process. This model treats the sweep motion as an impulsively started flow over a flat plate. An averaging technique is demonstrated to predict the important features of the surface shear stress.

In order to confirm the time dependent model assumptions, measurements of the probability distribution and cross-correlation of the longitudinal turbulent velocity and the surface shear stress were evaluated. The sweep-scale, sweep-direction, and origin of the

instability are determined from isocorrelation maps. The shape of the probability density distributions of the velocity near the surface and the surface shear stress are found to be similar. However, the velocity probability distribution changes rapidly with increasing distance from the surface.

As implied by the time dependent model for the surface shear stress, the magnitude of the large surface shear stress would be substantially changed if the sweep motion could be modified. A series of thin, metal plates were employed to block the instability from reaching the surface. Results show that the mean value of surface shear and the large magnitude fluctuations of surface shear stress were reduced significantly. The variation in surface shear was found to be extremely sensitive to slight angle of attacks of the plates.

Ho-Chen Chien
Civil Engineering Department
Colorado State University
Fort Collins, Colorado 80523
Spring, 1981

TABLE OF CONTENTS

TABLE OF CONTENTS (CONTINUED)

LIST OF SYMBOLS

Symbol	Definition	Dimension
C_f	Skin friction coefficient	
f	Transformed velocity defined in Equation (11)	
f	Frequency	1/T
f_0'	$\equiv \partial f/\partial \eta \ \eta=0$ defined in Equation (32)	
F_0, F_1	Series solution assumed for f, Equation (17)	
F(f)	One-dimensional frequency spectrum function	T
g	Transformed velocity defined in Equation (11)	
G_1, G_2	Series solution assumed for g, Equation (18)	
H	Form factor	
h	High-pass filtered frequency signal	
L	Characteristic length in x direction	L
l	Low-pass filtered frequency signal	
N_i	Number of Δt^* intervals corresponding to f_o' within ith f_o' window	
N_o	Total number of Δt^* invervals used	
P( )	Probability density function	
Δp	Pressure difference	M/LT^2
R_e	Reynolds number based on U_c and L	
R_θ	Reynolds number based on momentum thickness	
$R_{\tau_w u}$	Cross-correlation coefficient between surface shear stress and velocity u	
$(R_{\tau_w u})_{max}$	Maximum $R_{\tau_w u}$ value for a cross-correlation curve	
T	Mean bursting period	T
$\bar{T}$	Non-dimensional mean bursting period, TU_∞/δ	T
T_s	Total summation time used for correlation measurements	T
t	Time	T

LIST OF SYMBOLS (CONTINUED)

Symbol	Definition	Dimension
t^*	Transformed time = $1/\phi$	
t^o	Non-dimensionalized time	
Δt	Time increment used in correlation measurements	T
Δt_{max}	Maximum time delay when $(R_{\tau_w u})_{max}$ is obtained	T
U, V	Mean velocity components in the x and y directions	L/T
U_c	Characteristic velocity	L/T
$(U_c)_{mp}$	Most probable characteristic velocity	L/T
U_{conv}	Convective velocity	L/T
U_τ	Shear velocity	L/T
U_∞	Freestream velocity	L/T
u,v	Instantaneous velocity component in x, y direction	L/T
u',v'	Velocity fluctuations in x, y direction	L/T
u^o,v^o	Non-dimensionalized velocity in x, y direction	L/T
$\overline{u'v'}$	Time mean value of product u' and v'	L^2/T^2
ΔW	Longitudinal separation between the lead wire and the rear wire of a dual hot wire probe	L
$\bar{x}$	Averaged x-coordinate of the location of instability origin measured upstream from the surface sensor	L
x	Streamwise coordinate along the surface of the test model	L
y	Coordinate normal to the surface of the test model	L
z	Lateral coordinate normal to x and y measured from center of tunnel	L
x^o,y^o,z^o	Non-dimensionalized coordinate in x, y and z direction	
x^*	Non-dimensional x coordinate, = xU_τ/ν	

LIST OF SYMBOLS (CONTINUED)

Symbol	Definition	Dimension
y^*	Non-dimensional y coordinate, = yU_τ/ν	
z^*	Non-dimensional z coordinate, = zU_τ/ν	
γ	Intermittency	
δ	Boundary layer thickness	L
δ^*	Displacement thickness of boundary layer	L
η	Transformed independent variable define in Equation (10)	
θ	Momentum thickness of boundary layer	L
ν	Kinematic viscosity	L^2/T
ξ	Transformed independent variable defined in Equation (16)	
ρ	Mass density	M/L^3
τ_w	Surface shear stress	M/LT^2
$\overline{\tau_w}$	Mean surface shear stress	M/LT^2
$(\tau_w)_{mp}$	Most probable surface shear stress measured	M/LT^2
ϕ	Transformed independent variable defined in Equation (10)	
ω	An empirical constant defined in Equation (36)	

CHAPTER I

INTRODUCTION

Since Prandtl introduced the concept of a boundary layer in 1904, the viscous effects on the flow adjacent to a solid boundary have received a great deal of attention. The laminar boundary layer problem has been solved numerically for a wide range of flow condition. However, the turbulent boundary layer problem is still far from being solved due to its complex nature. Attempts which paralleled the techniques employed in solving the laminar boundary layer problem were also applied to the turbulent cases. The eddy viscosity (or mixing length) concept still is viewed as an engineering technique to evaluate turbulent shear flows. Conventionally, a model which divided the turbulent boundary layer into an inner region and an outer region was hypothesized. Considerable amount of effort has been made to obtain better estimates of the mixing length and eddy viscosity for the two distinct regions of a turbulent boundary layer. The introduction of the idea of eddy viscosity substitutes long-time averaged statistical quantities for the time dependent properties which are inherent to turbulent flow. While of value in limited engineering applications, the early models have for the most part required a great deal of empirical input.

In the last two decades, as a result of the improvement of experimental techniques and the advance of electronic computer technology, a great deal of information about the turbulent boundary layer has been obtained. The new information has led to a better understanding about the structure of the turbulent boundary layer. Detailed investigation of flow properties in the near wall region, and the outer region, have been made. Different dominant flow features exist in the

two regions. A large scale motion prevails in the outer region, while the bursting phenomenon is the most important feature in the near wall region. However, the relationship between the large scale motion and the bursting phenomenon is not well understood. It is also necessary to relate the features to the important properties, such as surface shear stress.

In the present study, a physical model which describes a possible connection between the large scale motion and the bursting phenomenon is hypothesized. Following this complex model, a simplified time dependent model for the surface shear stress under a turbulent boundary layer was employed to illustrate the importance of time dependent solution of a turbulent flow. A stochastic averaging technique was developed to account for the random aspect of flow in predicting the surface shear stress. Predicted surface shear was compared with experimental results by assuming a Gaussian or a modified Rayleigh probability distribution of the sweep motion. Experimental evidence was obtained to support the time dependent model. Experiments were performed over a nearly zero pressure gradient surface in a small wind tunnel. Time dependent data evaluated include; convective velocity, probability and correlation of the turbulent velocity and surface shear stress. A simple, thin plate devices was used to modify the structure of the flow near the surface, which in turn reduced the surface shear stress. The device was based on the implication of the model for the flow in the inner region and its relation to the surface shear stress. The results appear to justify the assumed model.

CHAPTER II

REVIEW OF THE TURBULENT BOUNDARY LAYER STRUCTURE

2.1 Early Model

Since Prandtl introduced the concept of a boundary layer in 1904, the viscous effects on the flow adjacent to a solid boundary have received a great deal of attention. A boundary layer could be either laminar or turbulent. The laminar boundary layer problem can be solved numerically, however, the turbulent boundary layer problem is still far from being solved due to its complex nature. Pioneer studies made by Prandtl, von Karman and others contributed considerably to the early understanding of turbulent boundary layer characteristics. Conventionally, two distinct regions in a turbulent boundary layer were hypothsized. In the "wall", or "inner" region, the viscous effects are important; while in the "outer" region, the turbulent transport of momentum is dominant.

Attempts which apply the same technique employed in solving the laminar boundary layer problem were also used to evaluate the turbulent cases. One of the earliest approaches was the concept of eddy viscosity introduced by Boussinesq. Prandtl constructed the mixing length hypothesis to relate the turbulent shear term to the mean veocity gradient. Followed the two-region model of the turbulent boundary layer, numerical evaluation of the mixing length assumed that it increased nearly linear with distance from the wall in the wall region, and that it remained nearly constant over the outer region.

Over the ensuing years, certain refinements of the model were made, mainly regarding the evaluation of the mixing length hypothesis. Van Driest (1956) forsaw the fluctuating nature of the fluid near the

wall and suggested a damping factor for the eddy viscosity in this area. Townsend (1956) suggested the use of a mixing length which was corrected in accordance with the intermittency factor in the outer region. Other refinements, such as considering the entrainment properties of turbulent boundary layer, Head (1958), have led to some improvements in predicting the boundary layer properties.

Parallel to the above model, Clauser (1956) suggested that the outer region of the turbulent boundary layer could be treated as a laminar boundary layer having a thin sublayer of a different fluid with much lower viscosity next to the wall. Measurements of flow variables in the sublayer region, which reflected the random aspect of turbulent shear flow, made before 1957 was summarized by Corrsin (1957). These measurements revealed the existence of large magnitude fluctuations of surface shear stress, surface static pressure and boundary layer thickness.

2.2 Detailed Evaluation of the Turbulent Boundary Layer Structure

In the last decade more detailed information about the turbulent boundary layer structure has been obtained. This new information has led to a better understanding of the structure of turbulent boundary layers; however, a consistent, workable model for the flow has proven elusive. Recently developed, special, photographic techniques have made visualization of the developing turbulent boundary layer possible. Figure 1 is a sketch of observations and Figure 2 shows a photograph of a turbulent boundary layer developing along flat plates with zero pressure reported by Falco (1977) and Nagib et al. (1979), respectively.

Different aspects of the flow can be seen in the two figures. Figure 1 shows the overall view of the general shape of the large scale

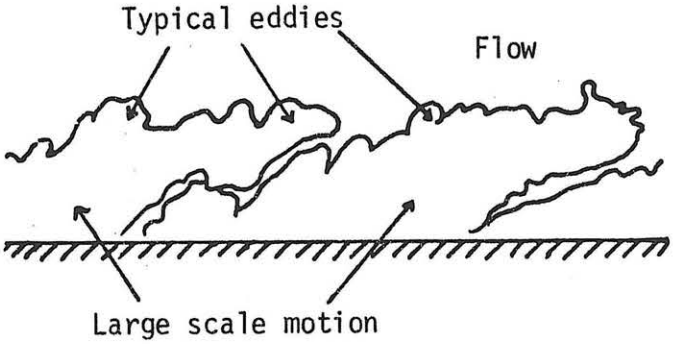

Figure 1. Sketch of turbulent boundary layer obtained by smoke visualization by Falco (1977) at $R_\theta \simeq 4000$.

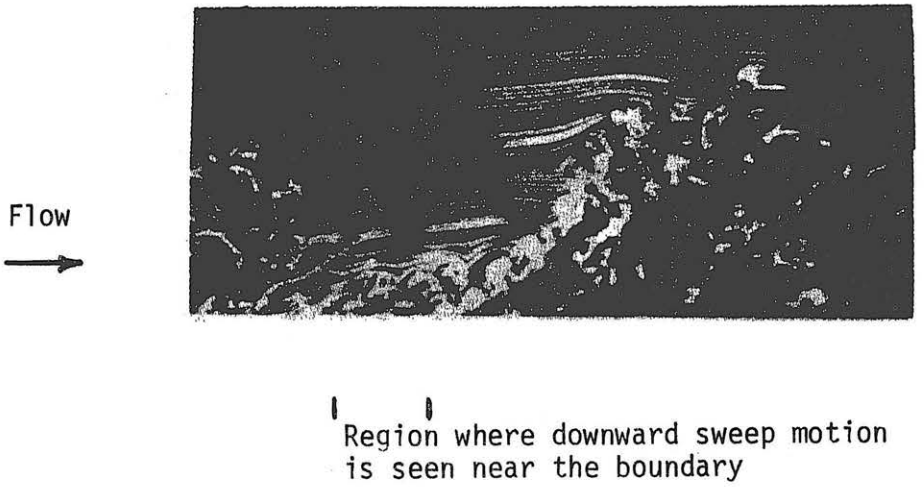

Figure 2. Photograph of smoke in a turbulent boundary layer reported by Nagib et al. (1979).

motion and the typical smaller eddies rolling over it. Figure 2 illustrates the interface between the large scale turbulent motion and the non-turbulent outer flow. The streamlines of irrotational, non-turbulent flow in the valley between two consecutive large scale turbulent bulges is shown in Figure 2.

A qualitative picture of the velocity distribution in a large scale bulge and its surrounding fluid was obtained by Blackwelder and Kovasznay (1972), using conditional sampling techniques to evaluate the hot wire signals. Figure 3 shows their results, wherein $U_c = 0.93\ U_\infty$ represents the mean velocity of the turbulent bulge. The rotational nature of the large scale motion in the bulge was demonstrated by Blackwelder and Kovasznay (1972). The local velocities at the front and back of the interfaces, measured by Kaplan and Laufer (1969) using a ten-hot-wire rake across the boundary layer, are shown in Figure 4. It was found that the downstream side of the interface moves faster than the upstream side. Kovasznay et al. (1970) reported zone averages of the fluctuating and streamwise mean velocity components, as shown in Figures 5 and 6. Within the non-turbulent zone the fluid moves faster than it does in the turbulent zone. The turbulent intensity in the non-turbulent region is lower than in the turbulent zone, though it was not zero.

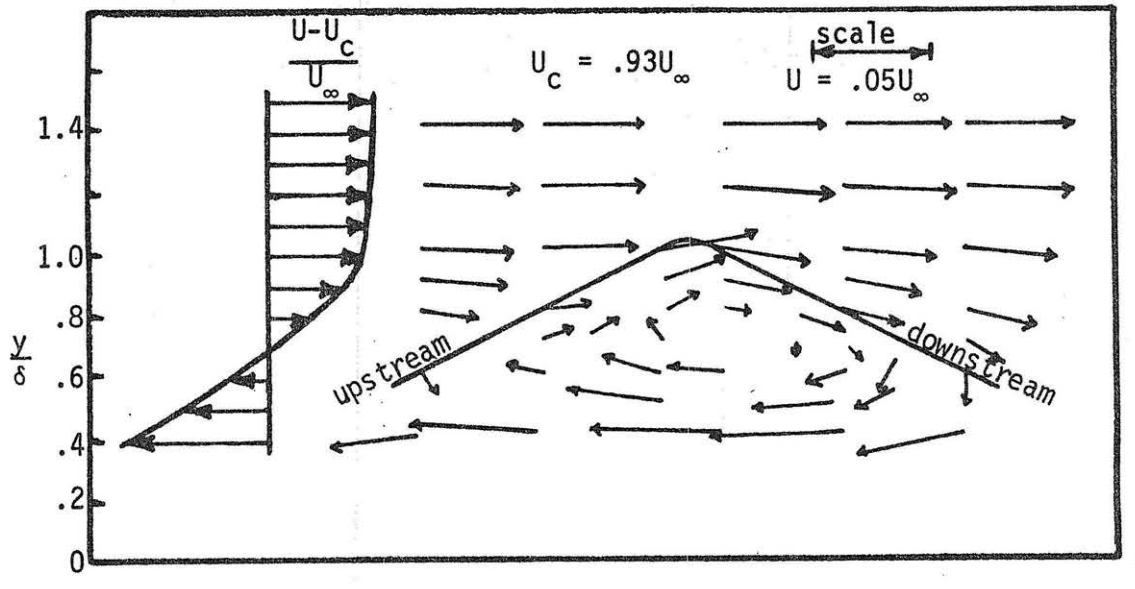

Figure 3. Velocity distribution in the outer region of the boundary layer obtained by Blackwelder and Kovasznay (1972).

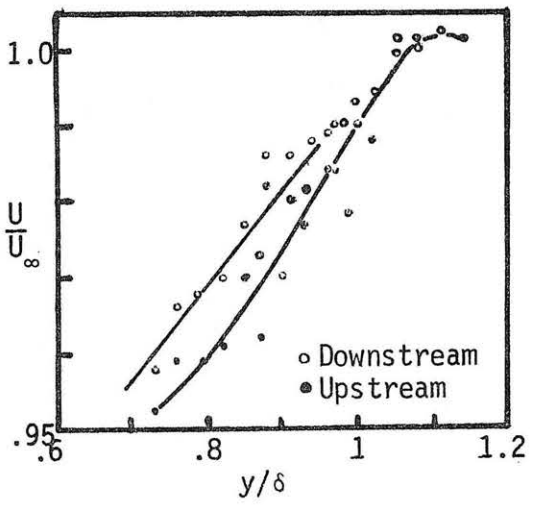

Figure 4. Velocity distribution at the turbulent bulge interfaces obtained by Kaplan and Laufer (1969).

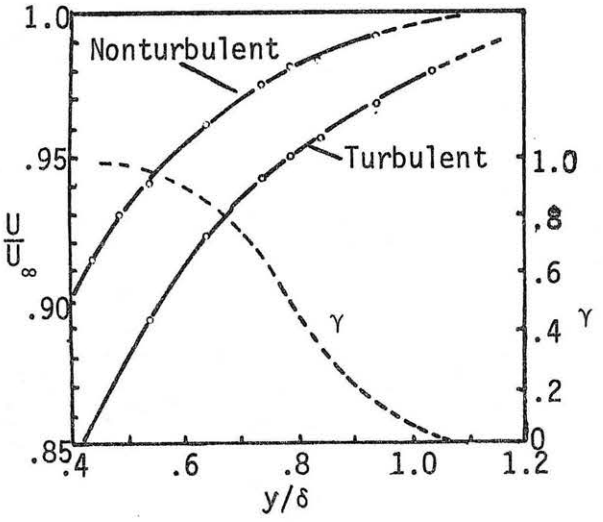

Figure 5. Zone averages of the streamwise velocity component reported by Kovasznay et al. (1970).

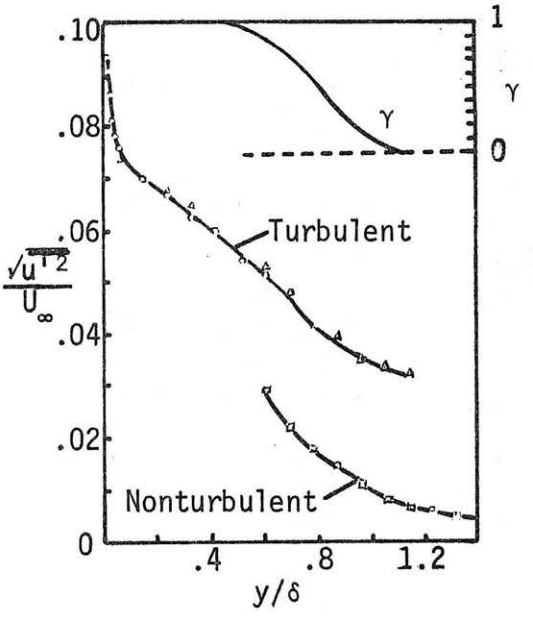

Figure 6. Zone averages of the intensity of the streamwise velocity fluctuations reported by Kovasznay et al. (1970).

From the illustrations of Figures 3, 4 and 5, it appears that in the valleys of the consecutive large eddy structures there is a

localized pressure gradient, which tends to push the fluid inward toward the wall, and also accelerates the fluid on the upstream side of the turbulent bulge. The local streamline curvature near the wall, which would imply a local pressure variation is indicated in Figure 2. The non-turbulent fluid is seen to be thrust almost to the surface.

Although the photographs made by Falco (1977) and Nagib et al. (1979) show the large scale coherent structure in the outer region of the turbulent boundary layer, the structure buried in the confined wall region is not discernible. Special equipment and techniques are being used to explore the turbulent structure in the wall region. Kline et al. (1967) conducted visual studies by using a hydrogen bubble technique. Corino and Brodkey (1969) observed motions of suspended colloidal particles in the wall region of a circular pipe flow by using a high-speed camera moving with the flow. Combined visualization and hot-wire anemometer techniques were also employed by researchers such as Kim et al. (1971), Falco (1977, 1980) and others.

Visual studies of Kline et al. (1967), Corino and Brodkey (1969) and Kim et al. (1971) revealed the existence of a somewhat well-organized but spatially and temporally dependent motions within the wall region. A large scale, streaky structure and an intermittently occurring, violent bursting process were observed in the wall region. A cycle of the bursting phenomenon was described with the help of sketches, Figure 7, by Corino and Brodkey (1969). Each sketch of Figure 7 shows an important step in the motion involved in a bursting cycle.

First, near the wall low-speed streaks form and gradually grow to a vertical dimension of $y^* \simeq 10$, as shown in Figure 7a). When the

streak reaches $y^* \simeq 10$ it starts to oscillate and continues to grow. The oscillation amplifies, as it continue to rise, until it becomes unstable and suddenly breaks into turbulent motion at a height of $10 < y^* < 30$. Simultaneously, a portion of the low speed fluid of the streak is ejected into the core region, which is termed the "ejection" motion, and shown in Figure 7b). Following the ejection, a mass of fluid, with dimensions larger than the ejection scale and with velocity greater than the local mean velocity, flows parallel to or at a slight angle toward the wall. The inward flow of the high-speed fluid is called the "sweep" and is shown in Figure 7c). Kim et al. (1971)

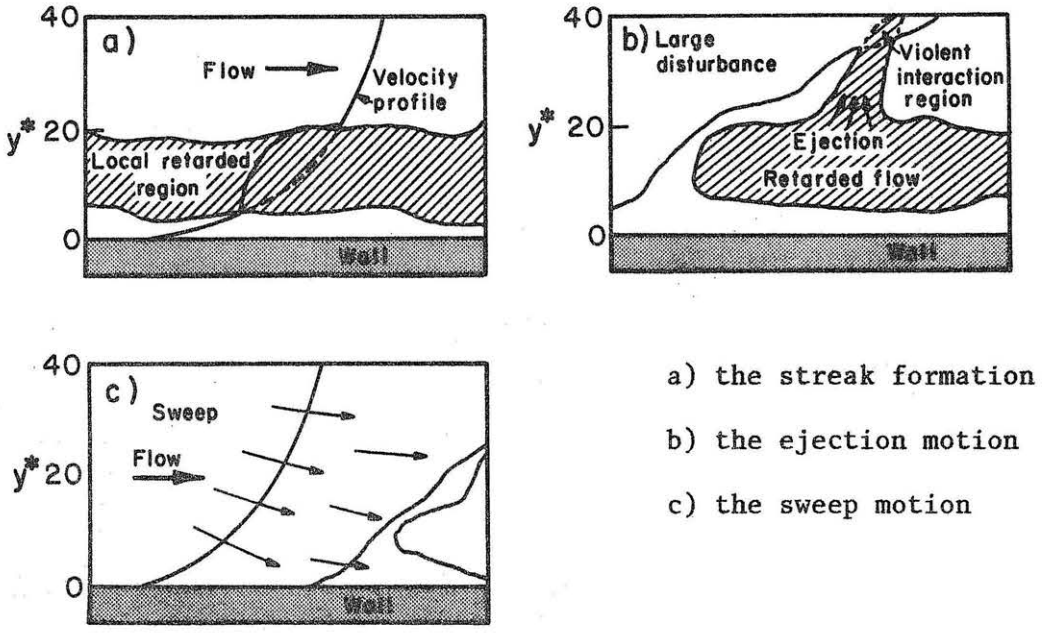

a) the streak formation

b) the ejection motion

c) the sweep motion

Figure 7. Steps in the flow cycle near the wall. Reported by Corino and Brodkey (1969).

provided photographs of streak-lines using hydrogen bubbles for each stage of the bursting phenomenon. Readers are referred to Kim's report for more details.

Associated with the sequence of motions in bursting, occasionally part of the low speed ejected fluid is deflected back toward the wall and at the same time incoming, accelerated fluid is reflected outward away from the wall. These motions are called "inward interaction" and "outward interaction" respectively. Combinations of streamwise and vertical velocity fluctuations, u' and v', as shown in Table 1 are used to designate these motions.

Table 1. Signs of u', v' and u'v' related to motions in a bursting cycle.

Type of Motion	Sign of u'	Sign of v'	Sign of u'v'
Ejection	-	+	-
Sweep	+	-	-
Inward Interaction	-	-	+
Outward Interaction	+	+	+

Flow properties of each motion, especially the Reynolds shear stress $-\rho\, u'v'$, measured in the near wall region by Willmarth and Lu (1971), and Brodkey et al. (1974), indicate the importance of bursting in the generation of turbulent energy. Results of Willmarth and Lu (1971) showed that fractional contribution to $-\rho\, \overline{u'v'}$ at $y^* = 30$ are 80% and 43% due to the ejection and sweep respectively.

Although the bursting phenomenon is spatially and temporally unsteady, agreement on instantaneous traverse streak spacing and mean

bursting period from different measurements was obtained. Results obtained in water channels ($1800 < R_\theta < 2500$) by Kline et al. (1967), Bakewell and Lumley (1967), Kim et al. (1971) and Gupta et al. (1971) showed a nondimensional streak spacing of $z^* \simeq 100$. Rao et al. (1971) summarized the results of Kim et al. (1971), Runstadter et al. (1963), Laufer and Badri Narayanan (1971), and shown that the mean burst time period, $\bar{T}$, scales with the free stream velocity, U_∞, and boundary layer thickness, δ; and $\bar{T}U_\infty/\delta \simeq 5$ in the range $500 < R_\theta < 9000$. Results reported by Falco (1980) shown that $\bar{T}U_\infty/\delta$ could range from 4 to 10 for approximately the same R_θ range.

As demonstrated above, the details of the bursting process in the wall region is well documented. The consequent coherent structure in this region, on the other hand, has not received equivalent attention. Bakewell and Lumley (1967) and Lee, Eckelman and Hanratty (1974) were among those who proposed streamwise, concentrated vortices in the wall region. Recent measurements of the cross-correlation between the surface shear stress and the velocity field in the inner region, made by Kreplin and Eckelman (1979), have confirmed the existence of streamwise vorticity in the sublayer. The measurements suggested that the vorticity exists as a counterrotating vortex pair. In this regard, Falco (1980) presented results which he obtained by using visualization techniques and a hot-wire anemometer simultaneously, which confirm the presence of the vortex motion.

Falco applied oil-fog contaminant through a slit in the wall under a turbulent boundary layer and took pictures of the patterns of the oil-fog, which is carried by the coherent motion. Figure 8 is a photograph reported by Falco (1980). The pocket structure where the smoke

was washed-out, illustrates the existence of streamwise vortices in the near wall region. Falco divided the evolution of a pocket into five stages. The flow properties such as u, du/dy and uv for each stage were evaluated. Connection of each stage to the bursting process was discussed in great detail. Falco concluded that there exists a turbulence generation mechanism near the wall. This mechanism includes; stretching of the vorticity in the sweep motion, the generation of vorticity near the wall by the stagnation point flow that the sweep creates and mutual interaction of the vortices formed as a result of these processes leading to motion away from the wall.

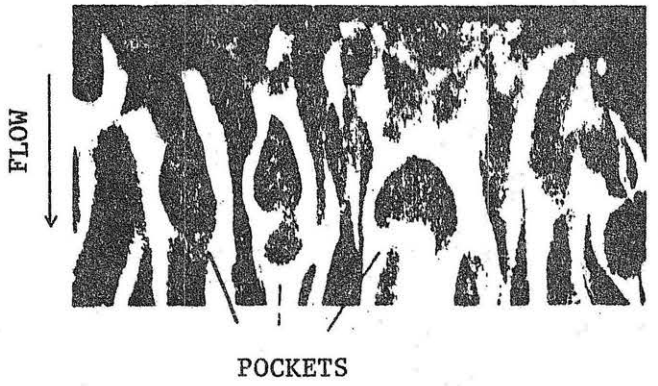

Figure 8. Sketch of the pocket structure near the wall photographed by Falco (1980) at R_θ = 738.

Several other flow characteristics, which are directly related to turbulent boundary layer structure, have also been investigated. The surface pressure variations under turbulent boundary layers have been studied in detail. Researchers, such as Corcos (1964), Blake (1970), Willmarth and Roos (1965) and others measured space-time correlations between fluctuations of surface pressure and turbulent velocities. The convective nature of the wall pressure was studied rather extensively.

Favre et al. (1957), Wills (1964, 1967) and others measured space-time correlations of turbulent velocities at two locations with the streamwise separation across the boundary layer. Their results showed the frequency dependent nature of the convective velocity. Also, in the outer region the convective velocity was smaller than the mean flow velocity and larger in the wall region. Cliff and Sandborn (1973) proposed a physical model for the convective velocity in a turbulent boundary layer, which also predicted this trend. The model of Cliff and Sandborn (1973) postulated that packets of turbulent fluid are generated in a production zone near the viscous sublayer. These packets were found to be discernible from the mean motion and may move either outward from or inward to the wall. The magnitude of the convective velocity in the production zone was found to be equal to the local mean velocity.

Large magnitude fluctuations in surface shear stress were first measured by Mitchell and Hanratty (1966) using an electrochemical technique. Blinco and Simons (1974), and Sandborn (1979) also reported large fluctuations of surface shear stress both in water channels and in wind tunnels. These results demonstrated that the surface shear stress fluctuations in turbulent boundary layer flows are highly time dependent and of large magnitude. The large fluctuation characteristics of the surface shear stress have been used as a means of studying the turbulent layer structure. Brown and Thomas (1977) reported a limited number of correlation measurements between the surface shear stress and the turbulent flow field. The surface shear fluctuations were employed by Kreplin and Eckelmann (1979) for studies regarding the transverse spacing of the low-speed streaks and streamwise vortices.

Based on the above observations, the time dependent nature of the turbulent boundary layer becomes evident. Since the introduction of the idea of eddy viscosity, boundary layer models have tended to substitute long-time averaged statistical quantities for time dependent properties. By doing so, the real mechanisms inherent to a turbulent boundary flow often have been overlooked and the progress toward their understanding limited. The response of a boundary layer type shear flow to a change in velocity or pressure is nonlinear. The statistical averaged approach to the problem masks the nonlinear effects, such as the observed large variations in surface shear stress. With the observation of coherent, repeatable, structures within the boundary layer, time dependent models for the flow should be possible. Solution of the time dependent problem first, followed by the use of a statistical averaging technique should help retain the nonlinear aspects of the flow.

CHAPTER III

SURFACE SHEAR STRESS FLUCTUATIONS

To predict the flow variables in the inner region of a turbulent boundary layer, where large magniture fluctuations have been observed, the non-linear interaction between the flow parameters need be considered. Based on the reported experimental results, a physical model for the flow near the surface is hypothesized. A time dependent solution for a simplified version of this model was pursued. Utilizing this solution and assuming a velocity distribution for the sweep motion a stochastic averaging technique was developed to predict the probability density distribution of surface shear stress. The purpose of this study is to illustrate the importance of the philosophy required to deal with large magnitude fluctuations in a turbulent shear flow. The philosophy requires that the time dependent equations of motion be solved first and then a statistical average be employed to account for the random aspects of the turbulent flow.

3.1 Physical Model

As discussed in the last chapter, visual studies, made by Kline et al. (1967), Corino and Brodkey (1969), Kim et al. (1971) and others, revealed that in the sweep motion associated with the bursting phenomenon, a stream of high speed fluid from the outer region was pushed into the wall region. This high-speed flow will create an impulsive effect on the flow in the proximity of the wall. It appears reasonable that the sweep motion is responsible for the appearance of large magnitude surface shear stress fluctuations, as observed by Mitchell and Hanratty (1966), Blinco and Simons (1974), and Sandborn (1979).

As first argued by Corrsin (1957), this large magnitude fluctuation of surface shear stress would not be seen if the time averaged boundary layer equations were solved. Due to the nonlinear relation between the external driving force and the flow response in a turbulent boundary layer, time averaging of the driving force removes the extremes of the flow response. Thus, it is evident that a time dependent approach is needed to account for this non-linear response characteristic of viscous flows.

Relating the surface shear stress to the sweep motion, together with the observations of Rao et al. (1971) and Falco (1980) that the mean bursting period scales with the outer region parameters, a physical model for the surface shear stress in a turbulent boundary layer can be hypothesized.

Near the surface in the valleys between the large eddies associated with the outer region, there exists strong, localized, vertical pressure gradients. At the beginning of a sweep sequence, there is a high shear between the retarded low-speed streak and the outer region turbulent flow. When the suddenly accelerated fluid associated with the sweep motion intrudes onto the valley, the shear increases and a large scale vortex motion appears. The flow then breaks into turbulent motion and packets of traverse vorticity are formed. The vorticity is carried into the large eddy motion by the surrounding velocity field. With the help of the pressure gradients in the valleys between the large eddies, a stream of outer flow migrates inward momentarily to meet the requirement of continuity. The downward high-speed flow forms streamwise vortices with the surrounding low velocity field and moves downstream. When these streamwise vortices

impulsively arrive in the proximity of the wall, very high magnitudes of surface shear stress are created. The viscous effect retards the high-speed fluid near the wall in a Rayleigh like suddenly accelerated plate fashion. The retardation of flow results in the formation of the low-speed streaks.

The visualization results of Nagib et al. (1979), as shown in Figure 2, together with the flow pattern observed by Blackwelder and Kovasznay (1972), Figure 3, provided evidence for the existence of a localized pressure gradient. As for the sequence of the ejection and the sweep motions, visual studies of Kline et al. (1967), and Corino and Brodkey (1969) indicated that the sweep motion occurs after the ejection motion but an ejection does not necessarily cause a sweep motion. Falco (1977) also observed this phenomenon. Falco reported hot-wire measurements of u', v' and u'v' at $y^* = 67$ and two types of large scale motion measured at this location, as shown in Figures 9a) and 9b). He explained that sometimes the motion shown in Figure 9b) follows that in Figure 9a), but a regular pattern is not apparent. This also explained the intermittent nature of the bursting process. Falco also implied that the sweep motion follows the ejection motion but not vise versa.

The penetration of the high-speed outer flow into the sublayer can be demonstrated by the following measurements. Chen and Blackwelder (1978) used temperature as a passive contaminant in the inner flow. By heating the entire wall of a wind tunnel test section to approximately 12°C above the free-stream temperature, a sharp internal temperature front, characterized by a rapid decrease in temperature, was found to extend throughout the boundary layer. Their results are illustrated in

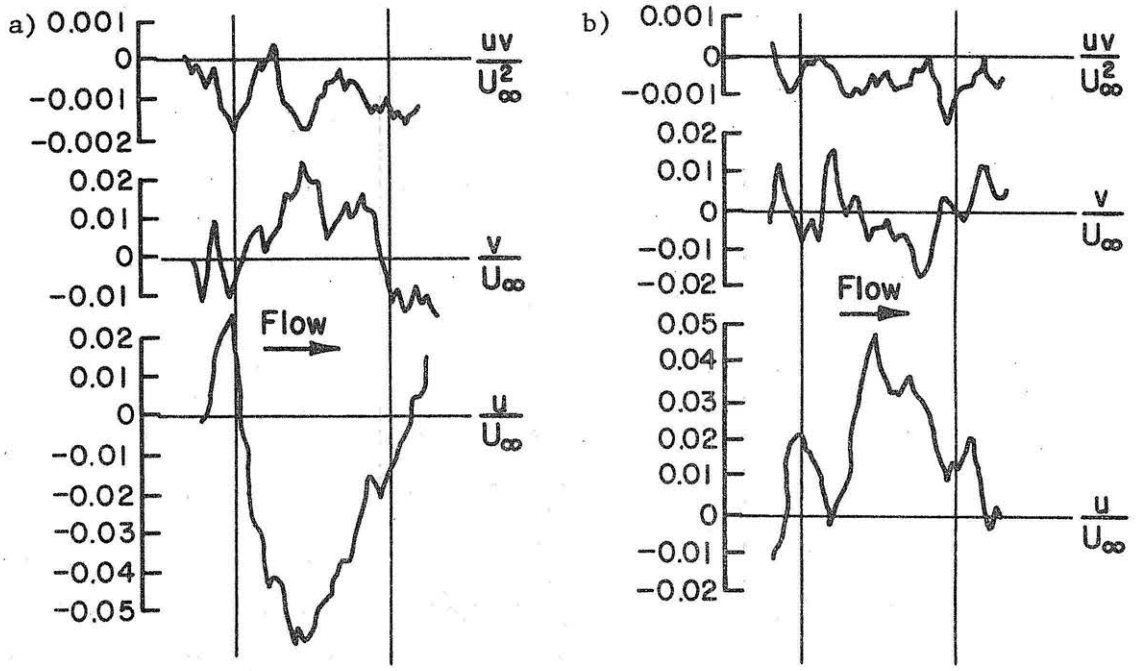

Figure 9. Ensemble averaged u', v' and u'v' signals for large scale motion measured at y* = 67 by Falco (1977).
a) Large scale motion type 1 has a negative zone averaged streamwise velocity perturbation.
b) Large scale motion type 2 has a positive zone averaged streamwise velocity perturbation.

Figure 10, where the arrows indicate a temperature front. Since the internal temperature front is an indication of the upstream side of the large eddy structure (back of large eddy as used in Figures 3 and 4), the data indicated that the sharp acceleration associated with the bursting phenomenon does indeed penetrate down to the sublayer. Ecklemann (1974) placed hot-film probes right above a surface film and recorded signals representing the streamwise velocity and the surface shear stress simultaneously. Figure 11 shows a set of these results for y* = 1.0, 1.9, 2.9, 4.8 and 8.6. An almost one-to-one correspondence between the streamwise velocity in the proximity of the boundary and the surface shear stress is noted. This evidence is used to justify the belief that the surface shear stress is directly related to the sweep motion.

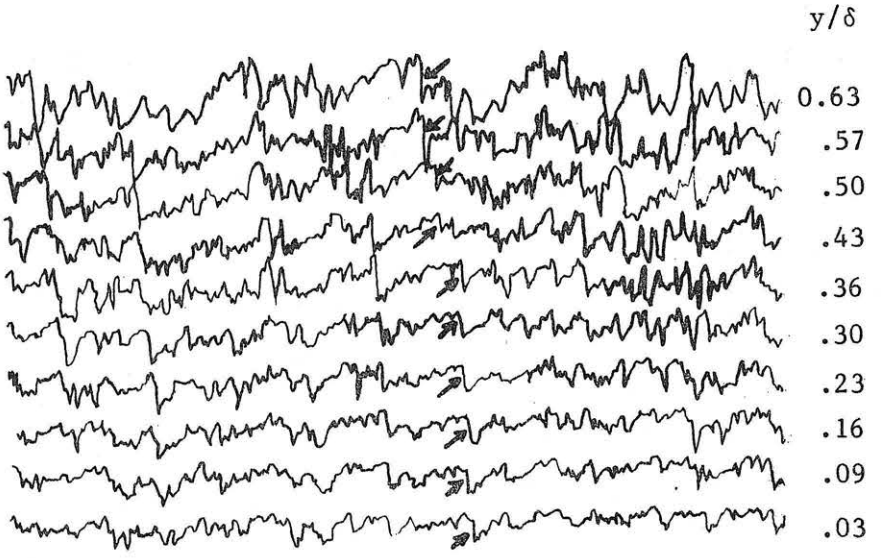

Figure 10. Simultaneous temperature signals from the ten-wire rake in the turbulent region reported by Chen and Blackwelder (1978). One particular temperature front is denoted by the arrows.

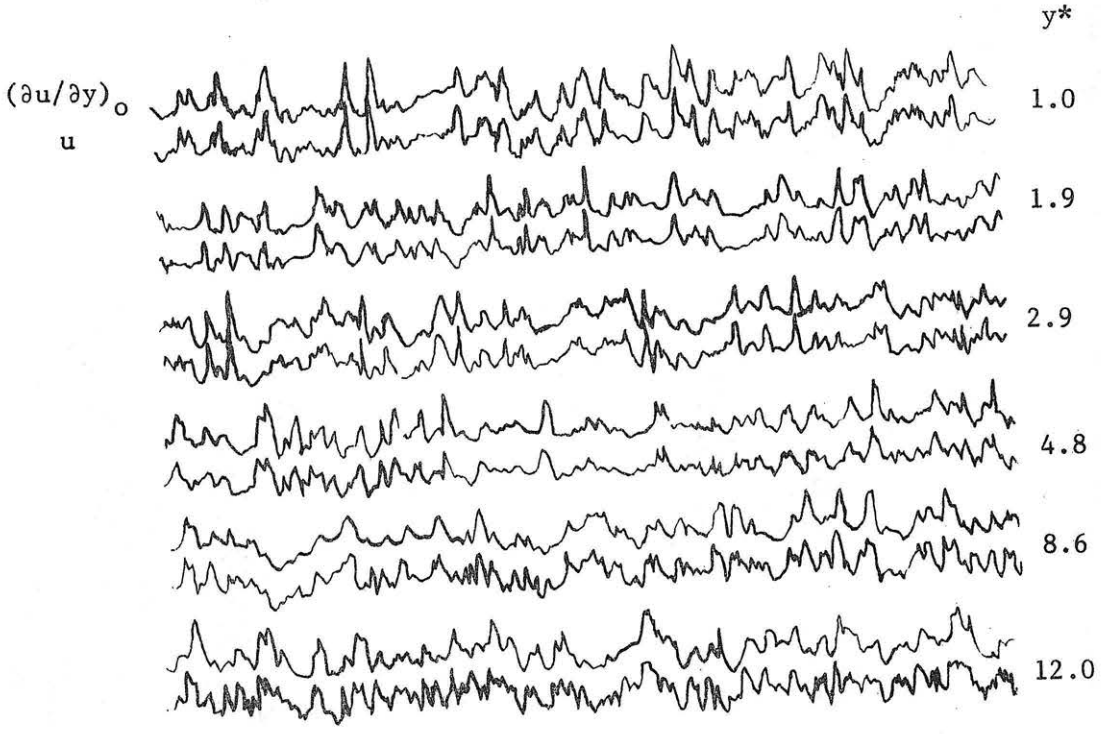

Figure 11. Simultaneous time records of instantaneous $(\partial u/\partial y)_o$ and u fluctuations at various y* position reported by Eckelmann (1974).

3.2 Simplified Time Dependent Model

Direct conversion of the model of a sweep-burst motion into an analytical solution for the turbulent boundary layer could be extremely complex. In order to develop an analytical approach it was necessary to evolve a simplified model. The basic assumptions for the simplified model are as follows:

(a) The time dependent boundary layer approximation for the Navier-Stokes equations for a two-dimensional flow over a flat plate is assumed to apply in the sublayer region.

(b) The time dependent solution starts with the beginning of the sweep motion portion of the overall sweep-burst cycle.

(c) The localized vertical pressure gradient across the sublayer, which must in part initiate the sweep motion, is of a very short time duration. The vertical pressure gradient is assumed to disappear instantaneously after the sweep motion starts.

(d) The initial, equivalent, free-stream velocity is that of the non-turbulent fluid which penetrates into the sublayer region at the beginning of the sweep motion. Its magnitude is expected to correspond to the values obtained by extrapolation of the measurements (non-turbulent velocity) to $y^* \simeq 30$ of Kovasznay et al. (1970), as shown in Figure 5. The equivalent free-stream velocity should also be related to the convective velocity in the sublayer region.

For the case of zero pressure gradient in the longitudinal direction, the two dimensional, time dependent equation of motion in the x-direction is:

$$\frac{\partial u}{\partial t} + u \frac{\partial u}{\partial x} + v \frac{\partial u}{\partial y} = \nu \frac{\partial^2 u}{\partial y^2} + \nu \frac{\partial^2 u}{\partial x^2} \qquad (1)$$

Using the results of convective velocity and cross-correlation measurements, which are discussed in Chapter V, the above equation can be simplified by estimating the order of magnitude for each term. For the case of U_∞ = 10.20 m/sec, the sweep motions originate approximately at 0.7 cm above the boundary and 7.0 cm upstream of the surface shear sensor. The averaged period of occurrence of sweep motion was estimated as 28 milliseconds, which was the time delay for maximum correlation between a hot-wire signal placed at the above coordinate, (7.0, 0.7), and the surface shear sensor. The characteristic velocity associated with the sweep motion was estimated as the convective velocity measured at the height where it has the same magnitude as the local mean velocity. $u \cong 5.0$ m/sec was selected based on the measurements. By assuming the longitudinal velocity is an order of magnitude larger than the vertical velocity within the flow domain considered, the order of magnitude for each term can be estimated. The presence of a vertical pressure gradient and the ejection motion may produce locally large values of vertical velocity, but they are assumed to be of short duration. The estimated order of magnitude for the term of Equation (1) are

$$\frac{\partial u}{\partial t} + u\frac{\partial u}{\partial x} + v\frac{\partial u}{\partial y} = v\frac{\partial^2 u}{\partial y^2} + v\frac{\partial^2 u}{\partial x^2}$$

magnitude (m/sec^2)	178	357	357	1.42	0.0010
order	$0(10^2)$	$0(10^2)$	$0(10^2)$	$0(10^0)$	$0(10^{-3})$

It is found that the term $v\,\partial^2 u/\partial x^2$ is much smaller than the other terms, thus it can be neglected similar to the results for the time averaged equations. The resulting Navier-Stokes equation for the time dependent flow in the x-direction is

$$\frac{\partial u}{\partial t} + u \frac{\partial u}{\partial x} + v \frac{\partial u}{\partial y} = \nu \frac{\partial^2 u}{\partial y^2} \qquad (2)$$

The truncation of the time dependent solution of Equation (2) can be estimated as equivalent to $\bar{T}$, which is the most probable period between two consecutive bursting cycles.

In the present study, the model was developed to predict the time history of the surface shear stress during the bursting cycle. The flow domain considered is the inner region of the boundary layer. A variation of the effective freestream velocity might be expected over a bursting cycle duration, which also perturbs the flow; however, this effect should be small. The response of the surface shear stress to a variation of freestream velocity has been investigated by Watson (1958) for the case of a laminar boundary layer with surface suction. The surface shear stress response was demonstrated to be much smaller than that caused by an impulsively started motion. Thus, it was assumed that small variations in the effective freestream velocity would be of secondary importance.

There are certain limitations imposed on the model. Since the ejection and the sweep motions are large scale vertical motions, refinement of the model could require inclusion of the equation of motion in the y-direction also. Assumption (c) can be taken to imply that a zero thickness boundary layer exists instantaneously as the sweep motion starts. Thus, an infinitely large surface shear stress would be required by the model. Obviously, it will be necessary to limit the surface shear to finite values.

As the bursting process is very spatially and to a lesser extent temporally dependent, the strength of each sweep motion past a given

point will vary. A complete solution of the mean flow properties will require a stochastic averaging of the individual sweep-burst cycles.

Consider the surface shear stress induced by the "sweep" motion in the near wall region of a turbulent boundary layer. Assume that as soon as the "jet-like" stream carried by the sweep reaches the wall, a flow field is established instantaneously. Then, for the case of zero pressure gradient, the governing equation, Equation (2) and the continuity equation ($\partial u/\partial x + \partial v/\partial y = 0$) are solved. The boundary conditions are:

$$\text{for } t \geq 0,\ y \to \infty,\ u = U_c \equiv \text{constant} \tag{3}$$

$$\text{for } t \geq 0,\ y = 0,\ u = 0,\ v = 0 \tag{4}$$

which is the unsteady Blasius problem.

By introducing the following nondimensional terms,

$$u^o = u/U_c; \quad x^o = x/L; \quad t^o = \frac{U_c t}{L}$$

$$v^o = \frac{v}{U_c}\left(\frac{U_c L}{\nu}\right)^{\frac{1}{2}} \equiv \frac{v}{U_c}\sqrt{Re}; \quad y^o = \frac{y}{L}\left(\frac{U_c L}{\nu}\right)^{\frac{1}{2}} \equiv \frac{y}{L}\sqrt{Re},$$

Equations (1) together with the continuity equation and the boundary conditions become:

$$\frac{\partial u^o}{\partial x^o} + \frac{\partial v^o}{\partial y^o} = 0 \tag{6}$$

$$\frac{\partial u^o}{\partial t^o} + u^o \frac{\partial u^o}{\partial x^o} + v^o \frac{\partial u^o}{\partial y^o} = \frac{\partial^2 u^o}{\partial y^{o2}} \tag{7}$$

$$t^o \geq 0, \quad y^o \to \infty, \quad u = 1 \tag{8}$$

$$t^o > 0, \quad y^o = 0, \quad u^o = v^o = 0 \tag{9}$$

The above equations are further transformed by using

$$\phi = \frac{x^o}{t^o} \quad \text{and} \quad \eta = y^o/\sqrt{2x^o} \tag{10}$$

as the independent variables and

$$f = u^o \quad \text{and} \quad g = v^o y^o/\eta - f\eta \tag{11}$$

The transformed equations become:

$$2\phi \frac{\partial f}{\partial \phi} + \frac{\partial g}{\partial \eta} + f = 0 \tag{12}$$

and

$$2\phi\ (f - \phi) \frac{\partial f}{\partial \phi} + g \frac{\partial f}{\partial \eta} = \frac{\partial^2 f}{\partial \eta^2} \tag{13}$$

If $t^* = 1/\phi = t^o/x^o$ is introduced, Equations (12) and (13) become:

$$-2t^* \frac{\partial f}{\partial t^*} + \frac{\partial g}{\partial \eta} + f = 0 \tag{14}$$

$$(2 - 2t^* f) \frac{\partial f}{\partial t^*} + g \frac{\partial f}{\partial \eta} - \frac{\partial^2 f}{\partial \eta^2} = 0 \tag{15}$$

The Transformed boundary conditions are:

$$f = g = 0 \quad \text{at} \quad \eta = 0$$

and

$$f = 1 \text{ at } \eta \to \infty$$

A numerical solution for Equations (14) and (15) with the same boundary conditions was reported by Watkins (1975) for unsteady heat transfer in impulsive Falkner-Skan flows. An approximate solution for the same problem was later given by Gottifredi and Quiroga (1978). In both studies, calculations of the non-dimensional surface shear stress for several flow conditions were also presented. A comparison of the results obtained from the two solutions were shown to be in good

agreement. Gottifredi and Quiroga obtained an approximate form of the non-dimensional surface shear stress for the general Falkner-Skan flows. Unfortunately, an error was found in this approximate form. Their techniques were applied to the present problem and the correct form was employed.

By defining a new variable ξ as

$$\xi = \eta/\sqrt{2t^*} \tag{16}$$

and assuming a series solution for f and g of the following forms:

$$f = F_0(\xi) + F_1(\xi)t^* + \ldots. \tag{17}$$

$$g = G_1(\xi)t^{*1/2} + G_2(\xi)t^{*3/2} + \ldots \tag{18}$$

Equations (14) and (15) become two approximate formulas which contain terms involving $F_0(\xi)$, $F_1(\xi)$, $G_1(\xi)$ and $G_2(\xi)$. By collecting terms of like power of τ^* the following ordinary differential equations were obtained.

$$2\xi F_0' + F_0'' = 0 \tag{19}$$

$$2\xi F_1' + F_1'' - 4F_1 = 2F_0F_0' + \sqrt{2}\, G_1F_0' \tag{20}$$

$$G_1' + \sqrt{2}\xi F_0' + \sqrt{2}F_0 = 0 \tag{21}$$

Detailed derivations which lead to the above equations are given in Appendix A. Boundary conditions for Equations (17) and (18) become:

$$F_0 = F_1 = G_1 = 0 \text{ at } \xi = 0$$

$$F_0 = 1 \text{ and } F_1 = 0 \text{ at } \xi \to \infty$$

To solve Equations (19), (20) and (21), an approximate technique was used, which was attributed to Rosenzweig (1959) (and was applied by

Cess (1961) to the problem of heat transfer due to a nonsteady surface temperature). This technique requires an estimate of $df/d\xi$ at both very small ξ and very large ξ.

From Equation (19), the solution for $F_0(\xi)$ is

$$F_0(\xi) = \text{erf}(\xi) \tag{23}$$

For small value of ξ, $F_0(\xi)$ can be approximated as

$$F(\xi) = \text{erf}(\xi) = \frac{2}{\sqrt{\pi}} \sum_{n=0}^{\infty} \frac{(-1)^n \xi^{2n+1}}{(2n+1)n!} \simeq \frac{2}{\sqrt{\pi}} \xi \tag{24}$$

Using Equation (24), $G_1(\xi)$ was determined from Equation (21).

$$G'(\xi) = -\sqrt{2}F - \sqrt{2}\xi F' \simeq -\frac{2\sqrt{2}}{\sqrt{\pi}} \xi - \frac{2\sqrt{2}}{\sqrt{\pi}} \xi \simeq -\frac{4\sqrt{2}}{\sqrt{\pi}} \xi \tag{25}$$

Thus,

$$G_1(\xi) \simeq -2 \left(\frac{\sqrt{2}}{\sqrt{\pi}}\right) \xi^2 \tag{26}$$

By substitution of Equations (24) and (26) into Equation (20), we have

$$2\xi F_1' + F_1'' - 4F_1 \simeq \frac{8}{\pi} \xi - \frac{8}{\sqrt{\pi}} \xi^2 \tag{27}$$

By setting $\xi = 0$ in Equation (27), and using the boundary condition $F_1(\xi=0) = 0$, we obtain

$$F_1''(\xi=0) \simeq 0$$

Thus, we have

$$F_1'(\xi=0) \simeq \frac{4}{\pi} \tag{28}$$

and

$$\left.\frac{\partial f}{\partial \eta}\right|_{\eta=0} \simeq \frac{dF_0(\xi)}{d\xi} \cdot \left.\frac{\partial \xi}{\partial \eta}\right|_{\eta=0} + t^* \frac{dF_1(\xi)}{d\xi} \cdot \left.\frac{\partial \xi}{\partial \eta}\right|_{\eta=0}$$

$$\simeq F_0'(\xi=0) \cdot \frac{1}{\sqrt{2t^*}} + \frac{\sqrt{t^*}}{\sqrt{2}} F_1'(\xi=0) + 0\ (t^{*3/2})$$

$$\simeq \frac{\sqrt{2}}{\sqrt{\pi t^*}} + \frac{2\sqrt{2}}{\pi}\sqrt{t^*} + 0\ (t^{*3/2}) \qquad (29)$$

Equation (20) is true only for very small t^* due to the approximation used in Equation (24). For very small t^* $\sqrt{2}/\sqrt{\pi t^*} >> 2\sqrt{2}/\pi\ \sqrt{t^*}$, thus Equation (29) could be approximated by neglecting the terms of $0(\sqrt{t^*})$ and $0(t^{*3/2})$. Finally, for very small t^*,

$$\left.\frac{\partial f}{\partial \eta}\right|_{\eta=0} \simeq \frac{\sqrt{2}}{\sqrt{\pi t^*}} \qquad (30)$$

For very large t^*, the $\frac{\partial u}{\partial t}$ term in Equation (2) becomes negligible, and Equations (1) and (2) become the Blasius problem. Its solution was shown by Schlichting (1968) and Watkins (1975) as

$$\left.\frac{\partial f}{\partial \eta}\right|_{\eta=0} \simeq f'(\infty) = 0.4695 \quad \text{as } t^* >> 1 \qquad (31)$$

Equation (31) is assumed to be the expression for very large t^*.

Using Equations (30) and (31), the method of Rosezweig was applied and an approximate form for $\left.\frac{\partial f}{\partial \eta}\right|_{\eta=0}$, as expressed by Equation (32), was obtained. The derivation of Equation (32) is shown in Appendix B.

$$f_0' \equiv \left.\frac{\partial f}{\partial \eta}\right|_{\eta=0} \simeq \frac{\sqrt{2}}{\sqrt{\pi t^*}} \exp\{-2f'^2(\infty)t^*\} + f'(\infty)\ \mathrm{erf}\{\sqrt{2t^*}f'(\infty)\} \qquad (32)$$

where $f'(\infty) = 0.4695$. Calculated results of f_0' at several points along the t^*-axis are tabulated in Table 2. Using these f_0' values,

Equation (32) is plotted in Figure 12. As implied by assumption (c) of the time dependent flow model, infinitely large surface shear stress at $t^* = 0$ are unavoidable. As time, t^*, increases, f_0' approaches $f'(\infty) = 0.4695$ asymptotically.

3.3 Stochastic Averaging Techniques

The simplified time dependent flow model discussed in the last section cannot be directly used due to the random nature of the sweep motion. In order to account for the spatial and temporal dependence of the bursting process, a stochastic averaging technique, which incorporates the simplified model, was developed to predict the probability density distribution of the surface shear stress under a turbulent boundary layer.

This stochastic averaging technique starts with the construction of a histogram of f_0'. A general criterion for the truncation of Equation (32) is not available, so truncational values of t^* were estimated empirically by utilizing the experimental results to be discussed in Chapter V. By expressing t^* as $t^* \equiv t\, U_c/x$, truncational values of t^* could be estimated by considering a sweep motion which originated at the location of the instability. According to the proposed flow model, this specific sweep motion would affect the flow variables near the surface until the next sweep motion starts. Thus for a simplified case for which the frequency of occurrence and strength of the sweep motion are constant, the period between two sweep motions and the strength, U_c, together with x should be used to obtain the truncational t^*. For an actual flow problem, mean bursting period $\bar{T}$ and most probable U_c, $(U_c)_{mp}$, together with averaged x-coordinate of the location of instability origin, $\bar{x}$, should be used.

As concluded from the study of Cliff and Sandborn (1973), the convective velocity measured at the height where it has the same magnitude as the local mean velocity was considered as the most probable velocity of the sweep motion. Results summarized by Rao et al. (1971) and Falco (1980) for $\bar{T}U_\infty/\delta$ observed by many researchers were used to estimate $\bar{T}$. The space-time cross-correlation measurements of velocity and surface shear, which are discussed in Section 5.4 of Chapter V, provided the estimation of the averaged x-coordinate. By adopting $U_\infty\bar{T}/\delta = 7.5$ and using the results shown in Table 6 for δ, Figure 26 for $(U_c)_{mp}$ and Figure 28 for $\bar{x}$, the following values were obtained:

a) For $U_\infty = 8.55$ m/sec,

$$\delta = 6.528 \text{ cm} \qquad \bar{x} \cong 6.0 \text{ cm}, \qquad (U_c)_{mp} \cong 4.3 \text{ m/sec},$$

the truncation value of t^* is

$$t^* = \frac{\bar{T}(U_c)_{mp}}{\bar{x}} \cong \frac{7.5\ \delta\ (U_c)_{mp}}{U_\infty\ \bar{x}} \cong 4.10$$

b) For $U_\infty = 10.2$ m/sec

$$\delta = 6.350 \text{ cm}, \qquad \bar{x} \cong 7.0 \text{ cm}, \qquad (U_c)_{mp} \cong 5.1 \text{ m/sec},$$

the truncation value of t^* is

$$t^* = \frac{7.5\ \delta\ (U_c)_{mp}}{U_\infty\ \bar{x}} \cong 3.41$$

Based on the above estimations, $t^* = 4.0$ was chosen as a representative truncation time for applying Equation (32) to the following demonstration.

Equation (32) between $t^* = 0.0$ and $t^* = 4.0$ was plotted with 200 equal intervals of $\Delta t^* = 0.02$ on the t^*-axis.[1] For each f_0' a

[1] Principles of digital method for estimate of probability, Bendat and Piersol (1971), was applied in the present study.

window of width $\Delta f_0' = 0.1$ was used, the number of Δt^* intervals, including fraction of an interval, which has a value of f_0' within a specific window was estimated graphically. This number divided by the total number of Δt^* interval and window width, 200 and 0.1 respectively, resulted in the estimated probability density for f_0' covered in a specific f_0' window. The above procedure is expressed mathematically as follows:

$$P_i \equiv P[(f_0')_i] = \frac{N_i}{N_o} \frac{1}{\Delta f_0'} \tag{33}$$

where

$\Delta f_0'$ = width of each f_0' window

$(f_0')_i$ = central point of ith f_0' window

N_o = total number of Δt^* interval

= 200 in the present study

N_i = number of Δt^* interval such that

$$(f_0')_i - \frac{1}{2}\Delta f_0' \leq f_0'(t^*) \leq (f_0')_i + \frac{1}{2}\Delta f_0'$$

P_i = estimated probability density for f_0' covered in the ith f_0' window.

The results obtained using the procedure are tabulated in Table 3, and the estimated probability density function is plotted in Figure 13.

The relation between surface shear stress τ_w and f_0', i.e.,

$$\tau_w = \frac{\mu U_c}{\sqrt{2}\, x} \sqrt{\frac{U_c x}{\nu}}\ f_0' \tag{34}$$

was obtained by introducing x^o, y^o, u^o and η, (which were defined in the last section) into the relation for f_0'

$$f_0' \equiv \left(\frac{\partial f}{\partial \eta}\right)_{\eta=0} = \frac{\partial u^o}{\partial y^o} \cdot \frac{\partial y^o}{\partial \eta}\bigg|_{\eta=0} \tag{35}$$

The interrelation among τ_w, U_c and x was unknown. For the present study, it was assumed that for a specific boundary layer problem the x value could be estimated using the most probable τ_w and U_c, which were determined experimentally, and the most probable f_0' value calculated. Consequently, Equation (34) was simplified as

$$(\tau_w)_{mp} = \omega \, (U_c)_{mp}^{3/2} \, (f_0')_{mp} \tag{36}$$

where

$$\omega = \frac{\mu}{\sqrt{2}} \frac{1}{\sqrt{xv}} = \text{constant} \tag{37}$$

depends on a specific problem, which would be determined from the most probable values of τ_w and U_c for a specific problem.

By assuming that the probability density function of U_c for a specific problem is known and that U_c axis was divided into J windows of equal width of ΔU_c, the probability density $P[(U_c)_j]$ for U_c withing the jth U_c window could be estimated. $(\tau_w)_k$ is used for the grid point on the τ_w axis where its probability density $P[(\tau_w)_k]$ is to be calculated. From Equation (36) and (37), for the jth, U_c window, there is a particular ith window of f_0' which would generate a τ_w interval covering $(\tau_w)_k$. Thus the overall probability density $P[(\tau_w)_k]$ due to the above statistical U_c distribution could be estimated by

$$P[(\tau_w)_k] = \sum_{j=1}^{j=J} \frac{P[(U_c)_j] \cdot \Delta U_c \cdot P[(f_0')_i] \cdot \Delta f_0'}{(\Delta \tau_w)_j} \tag{38}$$

where

$(U_c)_j$ = jth U_c window,

J = total number of U_c windows,

K = total number of $(\tau_w)_k$ points,

$(f_0')_i$ = ith window of f_0' which generates a τ_w interval covering $(\tau_w)_k$ when associated with $(U_c)_j$,

$(\Delta\tau_w)_j = \omega[(U_c)_j]^{3/2}\,\Delta f_0'$,

$(\tau_w)_k$ = grid point on τ_w axis at which the probability $P[(\tau_w)_k]$ is calculated.

A crude estimate of $\overline{\tau_w}$ was obtained by

$$\overline{\tau_w} = \sum_{k=1}^{k} (\tau_w)_k \cdot P[(\upsilon_w)_k] \cdot \Delta(\tau_w)_k \quad . \tag{39}$$

The flow chart for the above procedure of probability density calculation for τ_w is presented in Appendix C.

To demonstrate the above stochastic averaging technique and its application together with the flow model to predict the surface shear stress, several sets of computations were made. Experimental results for the surface shear stress for the cases of U_∞ = 10.2 m/sec and U_∞ = 8.55 m/sec, (which are shown in Figures 23 and 26), were used to obtain the required constant ω. The convective velocity measured at the height where the convective velocity and the mean velocity were equal was used as the most probable velocity of the sweep motion. The following values were estimated from the experimental data:

a) For U_∞ = 8.55 m/sec,

$$(U_c)_{mp} = 4.30 \text{ m/sec}, \quad (\tau_w)_{mp} = 0.1 \text{ N/m}^2$$

b) For U_∞ = 10.20 m/sec,

$$(U_c)_{mp} = 5.10 \text{ m/sec}, \quad (\tau_w)_{mp} = 0.153 \text{ N/m}^2.$$

By assuming $(f_0')_{mp} = 0.5$, ω = 0.02666 and 0.0224 were obtained for the above two cases respectively.

Using these values and assuming several different possible distributions for the sweep velocity, results as shown in Figures

14a)-141) were obtained. The corresponding experimental measurements are also shown in these figures for comparison. A Gaussian probability distribution

$$P(U_c) = (\sigma\sqrt{2\pi})^{-1} \exp \{ - \frac{[U_c - (U_c)_{mp}]^2}{2\sigma^2} \} \tag{40}$$

and a modified Rayleigh distribution,

$$P(U_c) = \frac{U_c - (U_c)_{min}}{c^2} \exp \{ - \frac{[U_c - (U_c)_{min}]^2}{2c^2} \} \tag{41}$$

were employed in the present study. In the above equations, $(U_c)_{mp}$ was used as the mean value for the Gaussian distributions, $(U_c)_{min}$ and c were selected such that the assumed Rayleigh distributions would have the most probable U_c approximately equal to the $(U_c)_{mp}$, which corresponds to $(\tau_w)_{mp}$, as determined from Equation (36).

Computed results show that the skewed shape of the probability density distribution of surface shear stress under a turbulent boundary layer is predicted for each case tested. The predicted magnitude of the most probable shear stress is in reasonable agreement with the measurements. Compared with the measured probability distribution of surface shear, the analysis over predicts the high magnitude fluctuations. This over-prediction is due in part to the singular point encountered at $t^* = 0$ when Equation (32) was applied. The singularity combined with the summation scheme for computing $\bar{\tau}_w$, Equation (39), will contribute to the over prediction of $\bar{\tau}_w$. It is also possible that the frequency response of the measuring instruments may make the results at the large magnitudes questionable.

It was possible to improve the agreement (less than ± 20%) between the measured and predicted values of surface shear by employing

arbitrary values of the standard deviation and the equivalent velocity distribution.

Increase of the standard deviation for the Gaussian distribution and its equivalent quantity, c, for the modified Rayleigh distribution reduces the magnitude of the peak and flats out the shape of the resulting probability curve. The flatting effect is more apparent toward the lower shear stress side than toward the higher side, as can be seen by comparing Figures 14b) and c) with Figure 14a), and Figures 14e) and f) with 14d). These results seems to justify the approach, which leads to Equation (32), as well as the proposed physical model which predicts a Rayleigh type surface shear stress response to the bursting motion. Moreover, the agreement between the measured and predicted values, shown in Figures 14a) and 14d), suggests that the distribution of sweep velocity could be similar to a Gaussian distribution with ratio of mean value to standard deviation of about 0.10.

Parameters used in these computations and the mean surface shear stress obtained are summarized in Table 4.

CHAPTER IV

EXPERIMENTAL SETUP AND PROCEDURE

The experimental study was performed at the Engineering Research Center of Colorado State University. Measurements were made in a small, variable geometry, wind tunnel in a region where the longitudinal pressure gradient was nearly zero.

The major part of the measurements consist of correlations of surface shear stress and fluctuating velocity in the mean flow direction. Convective velocity and probability density of turbulent velocity and surface shear stress were also evaluated. The signals from a dual wire probe and a surface hot wire were recorded using a FM recorder. A correlation and probability analyzer was used to evaluate the cross-correlation between each set of signals and the probability distribution for the individual signals. The cross-correlation and probability of the voltage signals were plotted directly using an X-Y plotter. The instrumentation employed for these measurements included constant-temperature, hot-wire anemometers, an analog spectrum analyzer, filters , an analog percentage time analyzer, and a HP-1000 computer facility. Pressure and velocity measurements were evaluated using a capacitance pressure transducer.

4.1 Wind Tunnel

An open-return, variable geometry, wind tunnel, shown in Figure 15 was used. The test section was made of plexiglass and has a cross section of 45 cm x 45 cm. A 1.37-m fan driven by a variable speed motor was located downstream of the test section. The free stream velocity was controlled manually. Time variations in the free stream pressure were limited to ±3 percent.

The test section consists of a zero pressure gradient region of approximately 190 cm in length over which a turbulent boundary layer of the order of 6 cm in thickness was developed. The equivalent momentum thickness Reynolds number, R_θ, is of the order of 4.0×10^3. This flat plate region was followed by a curved, adverse pressure gradient region. Figure 15 shows the setup of the test section.

The flow measurements were limited to the zero pressure gradient region. At the centerline of the wind tunnel and 198 cm downstream of the entrance of the test section, a surface hot wire was mounted flush to the formica surface. A series of static pressure holes of 0.05 cm diameter were drilled along the center-line in order to evaluate the static pressure distribution. An actuator mounted beneath the plate was used to traverse the probes through the boundary layer.

The coordinate system used is that the x-axis is parallel to the surface and the flow (positive x is measured upstream of the surface hot-wire), the y-axis is perpendicular to the surface and the flow, and the z-axis is parallel to the surface and perpendicular to the flow direction.

4.2 Instrumentation

Hot wire probes. Hot wires were used as the sensing element for all correlation measurements, probability measurements and surface shear stress evaluation. The material for the hot wires was platinum-8% tungsten, 0.01 mm diameter for all sensors. The length of wires used ranged from 0.03 cm to 0.06 cm. The wires were operated by constant temperature, hot wire anemometer circuits.

Hot wire sensors of three different designs were employed. They were single wire probes, a dual wire probe and a surface wire. The

single wire probe was used for the turbulent measurements since it could be traversed very close to the wall. The dual wire probe, which had the approximate dimensions shown in Figure 16a), was used mainly for the measurements of convective velocity, and the cross correlation of surface shear stress and fluctuating velocities through the boundary layer. The rear wire signal of the dual probe was correlated with the lead wire signal in order to measure a convection time for the turbulent structure to travel from the lead to the rear wire. The information between the surface shear stress and related motion in the boundary layer was obtained by measuring the cross-correlation between the probe hot wires and the surface hot wire signals.

The surface hot wire was used to measure the fluctuating surface shear stress. It was constructed by mounting the wire directly on the surface, such that the heat transfer from the wire was limited to the linear velocity region of the boundary layer.

Correlation and probability analyzer. For correlation and probability measurements, a Signal Analysis Industries Corporation Correlation and Probability Analyzer, Model SAI-42 was used. The correlation analyzer was a hybrid computer, which uses both analog and digital techniques. Correlation analysis provides a quantitative measure of the degree of similarity between signals as they appear relative to one another in time. The SAI-42 model provides auto- and cross-correlation functions with incremental lag or time delays values ranging from 1 μsec to 1 sec resulting in total time delays of from 100 μsec to 100 sec. An auto- or cross-correlation function was determined simultaneously at 100 incremental lag points so that a complete correlation function is displayed at one time.

The probability analysis provided information concerning the likelihood that the amplitude of a signal lies within a prescribed interval. The analyzer determined probability at 100 continuous amplitude intervals. Value of each amplitude bound was obtained through a calibration procedure, which employed a sine wave of known amplitude.

Tape transport. A frequency modulation type of tape recorder was used for the study. Seven channels could be used to record signals simultaneously, however, only the odd number were used to avoid the possible time-displacement errors caused by the physical separation of the odd and even numbered heads.

Time percentage analyzer. A analog time percentage analyzer which was designed by Finn and Sandborn (1964) was used to measure the intermittency through the boundary layer. This analyzer measures the percent of time an ac signal is non-zero.

Small size pitot tube. A pitot tube with an elliptical shaped opening and the dimensions shown on Figure 16b) was used to measure the local mean velocity. The output of the pitot tube pressure was applied to the high side of a differential pressure transducer, while the low side was connected to the local surface static pressure tap. The pressure was sampled and digitized at a rate of 600 Hz and averaged for 20 sec by a HP-1000 computer. Each dynamic pressure reading was converted to the equivalent velocity and then averaged. The averaged velocity and root-mean-square value of the fluctuating component were returned to the keyboard terminal instantaneously. Using this small size pitot tube, the mean velocity at a height of $y^* \geq 2.0$ above the wall was determined.

Height indicating system. To explore the flow properties in the sublayer region, the actual height of the measuring probe must be accurately determined. The measuring probe was mounted on a rod, which was connected to a motor-driven actuator. Attached to the actuating mechanism was a dial indicator with an accuracy of 0.025 cm (0.001 in.). This indicator was used to indicate the height of the measuring probe above the surface. A thin graphite film (pencil mark) was applied on the flat plate. An electrical circuit was used to indicate when the probe was in contact with the graphite film, so the exact location of it could be determined. The dial indicator was then set to the effective height of the sensor (hot wire or pitot tube) above the surface. A special jig with a calibrated optical microscope was employed to determine the probe dimensions. Correction for velocity gradient and averaging errors were made.

4.3 Evaluation of the Hot-wire Signals

Time series of signals from the dual hot-wire and the surface hot-wire were recorded simultaneously for 3 minutes. A sine wave, which was used both as identification and for calibration was recorded before each set of measurements. The hot-wire voltages were controlled within specific limits to insure that the recordings contained all the frequency information from DC to the upper limit of the sensors. The sine wave was employed to calibrate the gains of the record and reproduce amplifiers of the tape recorder.

For convective velocity evaluation, the longitudinal separation between the lead and the back wires were divided by the time delay of the maximum correlation. For a detailed discussion of the evaluation of convective velocities, the reader is referred to Cliff and Sandborn (1973).

CHAPTER V

EXPERIMENTAL RESULT AND DISCUSSION

Measurements were made at free stream velocities of approximately 10.20 m/sec, 9.36 m/sec and 8.55 m/sec. The corresponding R_θ values are 4050, 3500 and 3080, respectively. The primary part of the measurements was related to the surface shear stress evaluation at the center line, 196.6 cm downstream of the entrance of the test section. The location (196.6 cm) was chosen as the origin of the coordinate system. Also, the positive streamwise coordinate (x-coordinate) was taken as upstream of the 196.6 cm station in the wind tunnel. At R_θ = 3080, modification of surface shear stress by blocking the passage of the sweep motion was investigated. This investigation was aimed to justify the proposed flow model.

5.1 The Flow Field over the Test Model

The time averaged variables of the turbulent boundary layer developed over the test section were evaluated. The object was to assure a nearly zero pressure gradient condition, a uniform flow and a normally behaved boundary layer over the surface.

The static pressure distribution along the centerline of the test model was obtained by measuring the pressure output from the 0.05 mm diameter holes referenced to the value at a location of 120 cm from the entrance of the test section. The results are tabulated in Table 5 and are plotted in Figure 17. The pressure is nearly constant from 30.0 cm to 200 cm. Although there is a slight variation in pressure along the surface, the deviations are of the same order as the accuracy that individual reading can be made.

At a free-stream velocity of $U_\infty \simeq 12.80$ m/sec, mean velocity profiles were measured for several lateral locations at x = -10.2 cm -15.20 cm and -24.11 cm, as shown in Figure 18. Velocity variations in the lateral direction across the test section were within approximately ± 1%. The profiles measured at x = -24.11 cm indicate an acceleration which corresponds to a favorable pressure gradient as indicated on Figure 17. The flow field up to the measuring point has a near zero pressure gradient and it is uniform across the span.

At the location of x = 0 and z = 0, detailed time averaged properties including mean velocity profiles, longitudinal turbulence intensity profiles and the intermittency were measured. Table 6 lists the related boundary layer quantities calculated from the mean velocity measurements. Also listed are the skin friction coefficient, C_f, the corresponding surface shear stress, $\bar{\tau}_w$, and shear stress velocity, U_τ. The skin friction coefficients were calculated from the one parameter equation of Bell (1979), shown in Figure 19. The inner region similarity plot for mean velocity is shown in Figure 20, and is compared with a typical "Law of the wall." The mean velocity profiles, turbulence intensity profiles and intermittency profiles are summarized in Figure 21. The related data for mean velocity, turbulence intensity and intermittency are tabulated in Tables 7, 8 and 9, respectively. In Figure 21b) turbulence measurements made by Klebanoff and by Eckelmann in the wall region over flat plates are also compared with the present data.

As shown in Figure 20, the comparison of results of the present study with the law of the wall indicates that the flow corresponds closely to a flat plate flow. The turbulence intensity measurements of

the present study is bracketed by the measurements of Klebanoff and Eckelmann, as illustrated on the insert of Figure 21b). The decrease of turbulence intensity toward the wall in sublayer region $0 < yU_\tau/\nu < 5$ indicates that high-speed fluid does reach the wall and travel adjacent to the wall as suggested by the time dependent model for the surface shear stress. Figure 21c) shows a comparison of intermittency measurements of the present study with the relation suggested by Klebanoff. Figure 22 shows spectrum measurements at several heights across the boundary layer. These plots show that the contribution of eddies in the higher frequency range increases as the wall is approached.

5.2 The Probability Distributions of Hot-wire and Surface-wire Signals

The probability density distribution of the surface shear stress, $P(\tau_w)$, and the streamwise turbulent velocity components, $P(u')$, at several heights from $y^* \simeq 2.0$ up to $y^* \simeq 800$ were evaluated. The probability density distribution of a specific quantity provides information on the magnitude of the fluctuating values. It would be expected that the velocity probability, $P(u')$, measured in the sublayer region should have a similar pattern as the surface shear stress, $P(\tau_w)$. Large magnitude excursions of the shear stress and the streamwise velocity flucutations have been reported near the wall.

Due to the non-linear relationship between the magnitude of surface shear stress and transducer output (voltage), a correction is required. The technique for evaluating the surface shear stress with surface hot wires is discussed by Sandborn (1979). Figure 23 shows the corrected curves of $P(\tau_w)$ for $U_\infty = 8.55$ m/sec and $U_\infty = 10.2$ m/sec. The surface shear stress is skewed with large positive magnitude fluctuations as great as 2.75 $(\bar{\tau}_w)$.

The probability density distribution of the streamwise velocity fluctuations at various heights are shown in Figure 24. The abscissa of these plots was normalized with the local mean velocity U. The variations of the velocity probability distribution with height are in agreement with similar results of Brodkay, Wallace and Eckelmann (1973). In the sublayer region, ($y^* \leq 10$), P(u') is skewed with large positive values. The maximum fluctuation observed at $y^* \simeq 2.0$ is of the same order of magnitude as the local mean velocity U. The probability distributions approach a Gaussian shape and gradually skew to the opposite direction with vertical height, $y^* \geq 150$, and the distribution has a very small standard deviation.

The negative side and positive side of P(u') could be viewed as representing flow of speed lower or higher than the mean velocity respectively. For $y^* \leq 10$, flow of speed higher than the mean velocity occurs over a small percentage of the total time. The high-speed flow is then gradually retarded. The retarding process lasts longer than the acceleration. Brodkey, Wallace and Eckelmann (1974) were able to determine the individual contribution of each motion in a bursting cycle to the retarding and accelerating process. Their results for $y^* = 3.4$ is illustrated in Figure 25. It shows that both the sweep motion and the outward interaction are accounted for in the flow acceleration; but the sweep is more effective than the outward interaction and is responsible for the much higher magnitude velocity. It also indicates that the ejection motion contributes more to the deceleration of the flow than the inward interaction does.

Comparison of the shape of $P(\tau_w)$ and P(u') in the sublayer region reveals a similar pattern. This similarity demonstrates the interrelation between the sublayer motion and surface shear stress. Although

the maximum fluctuation of u is only of the order of 2U, maximum fluctuations of the surface shear stress approache 3 $\bar{\tau}_w$. This increase in magnitude demonstrates the importance of the non-linear response involved in a turbulent boundary layer.

5.3 Convective Velocity Measurements

The dual-wire probe was used for the measurements of convective velocity over the test model. The two wires were separated by a distance, ΔW which ranged from 0.550 cm to 0.625 cm. Convective velocity profiles measured at x = 0.0 cm, z = 0.0 cm for U_∞ = 10.20 m/sec and 8.55 m/sec are shown in Figure 26 together with the corresponding mean velocity profiles.

The convective velocity was smaller than the mean-flow velocity in the outer region. But, the convective velocity was much higher than the mean velocity in the sublayer region. Since convective velocity is a measure of the rate at which the turbulent structures are convected, results shown in Figure 26 imply that turbulent structures in the sublayer are transported at a rate faster than the local mean velocity. This is possible only when a high-speed motion exists in the sublayer region. Measurements of convective velocity thus provides direct evidence for the existence of high-speed velocity associated with the sweep motion in the sublayer region, as proposed in the physical model.

5.4 Cross-correlation between Surface Shear Stress and Streamwise Turbulent Velocity

Space and time correlations of the time series of boundary layer-hot-wire and surface-hot-wire signals were evaluated. At selected heights, the surface-hot-wire and boundary-layer-hot-wire signals from the dual wires were recorded simultaneously for at least 3 minutes.

The cross-correlation between the surface shear stress, τ_w, and the streamwise turbulence velocity, u, defined as

$$R_{\tau_w u}(\Delta x, \Delta y, \Delta z; n\Delta t) = \lim_{T_s \to \infty} \frac{1}{T_s} \int_0^{T_s} \tau_w(t)\, u(t + n\Delta t)dt \qquad (42)$$

was evaluated using the hybrid analog digital correlator. In the above equation, Δx, Δy and Δz represent separation of the hot wire and surface wire in the x, y and z directions, respectively. $n\Delta t$ is the time increment and T_s is the total summation time used in the computation of the correlation. $R_{\tau_w u}$ for n = 1 to n = 100 were calculated. In this study, Δt ranging from 20×10^{-6} sec to 500×10^{-6} sec and T_s ranging from 30 sec to 66 sec were used.

The major portion of the correlation measurements were made by aligning the hot wire with the surface wire in the streamwise direction and keeping z = 0. The location of the hot wire varies from x = 9.0 cm to x = -7.0 cm. At each location, measurements were made at several heights from $y \simeq 0.008$ cm up to y = 1.27 cm. The equivalent non-dimensional heights ranged from $y^* = 3$ to $y^* \simeq 250$. For the z = 0 case, a single maximum of the curve, $(R_{\tau_w u})_{max}$ is nearly a constant value for a range of $n\Delta t$, thus, it was difficult to determine a unique value of Δt_{max}. This uncertainty in Δt_{max} increases as the magnitude of $(R_{\tau_w u})_{max}$ becomes smaller. In the present study, the midpoint of the uncertain range of $n\Delta t$ was chosen as $(\Delta t)_{max}$. The data of $(R_{\tau_w u})_{max}$ and $(\Delta t)_{max}$ are presented in Appendix D.

$(R_{\tau_w u})_{max}$ and $(\Delta t)_{max}$ obtained at each measuring point in the domain about the surface shear stress sensor were employed to construct

the peak isocorrelation curves and the peak time delay curves shown on Figures 28 and 29, respectively.

Three possible errors were investigated in the process of the correlation measurements. One is due to the unsteadiness of the flow, another is related to the repeatability of the results and the third is the phase miss-match between the measuring instruments. Evaluation of $(R_{\tau_w u})_{max}$ for different segments of the time series of the hot wire and the surface wire signals for a specific value of Δx and Δy separations showed that the maximum deviation of individual measurements from the mean value of $(R_{\tau_w u})_{max}$ is ±6% of the mean. To check the repeatability of the results, comparison of results obtained at the same locations on different days were made. On one day, the measurements were made using the lead wire of the dual wire probe; and on the second day, the back wire of the dual wire probe was used. The comparison is illustrated in Figure 30. From this figure, a maximum deviation of day-to-day measurements of less than ±10% was estimated. Based on these observations, the possible maximum uncertainty related to an individual evaluation is less than ±16% if the two uncertainties add linearly.

As illustrated in Figure 28, the peak isocorrelation curves for the three R_θ values show common characteristics. The isocorrelation lines for $(R_{\tau_w u})_{max} = 0.40$, 0.50, 0.60, 0.70 and 0.80 form closed loops around the surface sensor. A region of relatively low $(R_{\tau_w u})_{max}$, $0.2 < (R_{\tau_w u})_{max} < 0.3$, which is designated by the symbol B exists downstream of the contour of $(R_{\tau_w u})_{max} = 0.40$.

Before discussing the physical meaning of the present peak isocorrelation curves, the correlations between surface shear stress

and turbulent velocity in a duct evaluation of Rajagopalan and Antonia (1980) are of specific interest. A set of results obtained by Rajagopalan and Antonia are shown in Figure 31, in which the subscripts 1 and h represent the low-pass filtered frequencies and the high-pass filtered frequencies of a signal. These plots illustrate that for the turbulent velocity u measured outside the inner region only u_1 correlated with τ_{wh}. For u measured in the inner region, the correlation of τ_{wh} and u_h was much higher than the other frequency correlations.

Based on the above finding of Rajagopalan and Antonia, we can interpret the isocorrelation curves shown in Figure 28 as follows: in the outer region the correlations represent the large scale motion related to the surface shear stress; while in the inner region, the correlation between the entire u and τ_w signals are present, but the correlation between the high frequency part of u and τ_w is predominant. The high frequency part of the turbulent velocity in the inner region was confirmed to be associated with the bursting phenomenon by Kim et al. (1971) and others. Brown and Thomas (1977) observed that the large magnitude surface shear stress is also at the high frequencies. The close relation between the sweep motion and surface shear stress is evident.

The peak isocorrelation curves of Figure 28 for the inner region, $y^* \leq 30$, appear to be nearly parallel to each other between $x \simeq -1.5$ and $x \simeq 3.0$. On the downstream side of the surface wire, the isocorrelation lines for $.5 < (R_{\tau_w u})_{max} < .6$ are distorted to an elongated loop with its center inclined to the wall at a small angle. Since the high frequency part of u, which is directly related to the bursting

phenomenon, is the major contribution to the correlate with the surface shear stress, the isocorrelation lines in the inner region must indicate the approximate passage and evolution of the sweep motion.

The peak time delay curves, shown in Figure 29, provide information about the evolution of the large scale motion in the outer region. These curves start with a nearly vertical but irregular shape in the upstream region and gradually incline toward the wall for the downstream direction. The peak time delay curve, $(\Delta t)_{max} = 0.0$ sec, represents the mean locus of the upstream and downstream sides of the large scale motion, as discussed by Falco (1978). The angle between the mean of $(\Delta t)_{max} = 0$ curve and the surface is 13.0°, 11.13° and 12.53° for $R_\theta = 4050$, 3500 and 3080 respectively. These values are lower than the value of approximately 18° reported by Brown and Thomas (1977) for a turbulent boundary layer at a higher Reynolds number, $R_\theta = 1.06 \times 10^5$.

A limited number of measurements of $R_{\tau_w u}(\Delta x, \Delta y, \Delta z; n\Delta t)$ with $\Delta z \neq 0$ were also evaluated for $R_\theta = 4050$. The major part of these measurements were made in a domain of x from 0.0 cm to 5.0 cm and z from 0.0 cm to 1.5 cm on one side of the center line only. The hot-wire probe was placed at $y = 0.127$ cm, 0.254 cm and 0.381 cm above the surface. As the probe was moved away from the center-line, the magnitude of correlation decreased rapidly, however, a multimaximum correlation curve was obtained. The magnitude of correlation became negligible for z-distances greater than 1.5 cm.

Figure 32 shows typical cross correlation curves obtained for $\Delta x = 5.0$ cm, $\Delta y = 0.127$ cm and several z locations. The value of the maxima measured at each location is plotted on Figure 33 for $y = 0.127$

cm, 0.254 cm and 0.381 cm. For Figure 33 the data with solid circles indicates the existence of a multi-maximum correlation curve, while those with open circles represents the existence of a single maximum correlation curve. An approximate boundary between these two groups of data points is constructed for each plot of Figure 33. This boundary is related to the passage of the large scale motion. The lateral expanse of this boundary remains nearly constant of the order of $z^* = 100$ from $y^* = 22.82$ to $y^* = 84.7$. The boundary indicates the approximate scale of the large scale motion.

5.5 Surface Shear Stress Modification

Based on the physical model discussed in Chapter III, the large magnitude fluctuations of surface shear stress are directly related to the sweep motion of the bursting phenomenon. Correlation measurements, as discussed previously in section 5.4 of the present chapter, demonstrated the passage of the sweep motion. It was postulated that if the sweep motion could be modified or prevented from penetrating directly into the sublayer, the large magnitude fluctuations of surface shear stress would be damped or eliminated.

As shown in Figure 28c), at $R_\theta = 3080$ the sweep effect is first evident in a region at a nondimensional x-distrance of $x^* \simeq 750$ to 1000, and at nondimensional y-distance of $y^* \simeq 75$ to 100. The random, three-dimensional production of the fluctuations over the surface may limit somewhat the selection of a specific location of the start of the sweep motion. If the instability of this region can be blocked from reaching the surface, large amplitude surface shear fluctuations should be reduced dramatically. Thin aluminum plates of 0.013 cm thick but with different widths were placed at different heights above the

surface and at different locations with respect to the surface-hot-wire to examine their effects. Figure 34 show a sketch of a typical plate. The plates have a marked effect on the magnitude of the surface shear, indicating that the sweep motion is modified.

A summary plot of the change in the mean surface shear produced by three different widths of plates at three different heights is shown in Figure 34. Although the effect of both plate width and height can be determined from the measurements, a large amount of scatter was encountered. This scatter was traced to a critical alignment sensitivity of the plates parallel to the surface. Figure 35 shows tests made with the same plate set at +2.9, 0 and -2.9 degrees with respect to the surface. As demonstrated by Figure 35, the results are extremely sensitive to the angle of the plate. Repeat tests for the plate at 0.0 cm are also shown in Figure 35. Variation of mean surface shear stress as great as 20% was observed due to slight misalignment of the plate angle which could not have been greater than ±0.5 degrees.

The possibility of surface shear stress reduction caused by the wake behind the plate was also investigated. The plate of 3 cm wide, 0.4 cm high was placed with its trailing edge 4 cm upstream of the surface sensor. The mean velocity profile measured above the surface sensor at U_∞ = 8.55 m/sec is compared with result without the plate in Figure 36. A velocity defect was observed near the height of the plate. The plate wake showed little effect on the flow near the surface. Hence, it can be concluded that the wake effect on the reduction of surface shear stress should be of secondary importance.

The variations in the surface shear stress probability distribution obtained when the plate of 3 mm wide and 2 mm high was

placed at different locations are compared with the basic flow result in Figure 37. A major reduction of the large magnitude fluctuations was observed when the plate was placed at 2 cm upstream of the surface-hot-wire. However, almost no effect on the surface shear stress distribution was seen when the same plate was placed 7 cm upstream of the surface-hot-wire. Figure 38 shows the surface shear stress probability distributions for the plate of 3 mm wide and 8 mm high placed at various locations upstream of the surface-wire. The 8 mm high plate had very little effect on the surface shear fluctuations.

Based on the space-time correlation measurements for U_∞ = 8.55 m/sec as shown in Figure 28c), the origin of the instability is located about 0.6 cm above the surface and 6 cm upstream of the surface wire. The proposed flow model, as was described in Chapter III, predicted that the plate placed on the passage of the sweep motion would have considerable effect on the surface shear stress. This prediction seems to be justified by the results shown in Figure 37. On the other hand, the results shown in Figure 38 of the little effect induced by an 8 mm high plate implies that the surface shear stress is not affected by blockage in the outer flow. It was also noted that the present technique of blocking the sweep is effective for only one event. Once the plates are moved further upstream their effect vanishes. Thus, stopping a single sweep from reaching the surface does not appear to have a major effect on the overall boundary layer. The three dimensional characteristics of the events, apparently fill in for the one blocked event. Although the plates are of major interest in demonstrating the general concept of the present model, they do not produce an insight into the actual production of the sweep-burst phenomenon.

CHAPTER VI

CONCLUSIONS

In a turbulent shear flow, a sudden change of the external driving force causes a dramatic response of flow variables across the boundary layer. The response of the flow is non-linear due to the viscous effects. The mixing length and eddy viscosity models substitute long-time averaged statistical quantities for the highly time dependent variables involved in a turbulent flow, and thus mask a great deal of non-linear effects. Prandtl's turbulent boundary layer approach of employing the averaged Reynolds equation and a turbulence closure model has proved to be insufficient to predict flow variables with fluctuation of magnitude as great as the mean value, such as the cases for surface shear stress and also quantities in the separation region. The philosophy of solving first the time dependent equation of motion and then employing a stochastic averaging to include the random aspect of the flow is proposed and demonstrated. This approach is able to produce good predictions for the mean and time dependent surface shear stress under a turbulent boundary layer over a smooth plate.

Based on observations of the turbulent boundary layer structure, a physical model dealing with flow near the surface is hypothesized.

In the inner region of a turbulent boundary layer, an intermittent bursting phenomenon has been observed. Also, large magnitude fluctuations of the surface shear stress under a turbulent boundary have been reported. The present model proposes that the surface shear stress fluctuations are due to the non-linear response of the flow produced by the bursting process near the wall.

It is postulated that localized pressure gradients created in the valleys of the large scale structures are the origin of the bursting phenomenon. This localized pressure gradient produces the sweep motion, which in turn brings the high-speed fluid from the outer region inward toward the inner region. The high-speed fluid is then retarded near the wall and finally ejected outward. The ejection of the low-speed motion in turn, triggers the sweep motion and the bursting cycles repeat.

A simplified model was employed to illustrate the non-linear response of surface shear stress to a single sweep motion. The model treated the sweep motion as an impulsively started boundary layer flow above a surface. An approximate time depenent solution for the shear stress at the wall in response to a discrete sweep velocity was obtained. Assuming a Gaussian or a modified Rayleigh probability distribution for the sweep velocity, a stochastic averaging technique was developed for prediction of the resulting surface shear stress response. This approach was shown to predict the large magnitude fluctuations and the highly skewed probability distribution of the surface shear stress.

In order to justify the time dependent model, measurements of the probability distribution and cross correlations of the turbulent velocity and surface shear stress were evaluated for a zero pressure gradient, turbulent boundary layer. Experimental results indicated that the probability distributions of the longitudinal turbulent velocity in the sublayer region, $(0 < yU_\tau/\nu < 10)$, show characteristics similar to the probability distribution of the surface shear stress. Large magnitude fluctuations greater than two times the mean surface shear were

observed. Cross correlation measurements showed that a high degree of correlation exists between the surface shear stress and the turbulent velocity in the inner region. From the peak isocorrelation curves near the surface, the origin of the flow instability can be identified at a non-dimensional distance of approximately ($y^* =$) 150 above the surface and a non-dimensional distance ($x^* \simeq$) 1500 upstream of the surface sensor. Also, these curves indicate the approximate passage of the high-speed flow associated with the sweep motion. It was also concluded that the convective velocity measured at the height near the origin of instability is related to the sweep motion.

As implied by the time dependent model for the surface shear stress, if the sweep motion could be modified, the magnitude of the large shear stress fluctuations at the wall would be substantially changed. A series of thin (0.13 mm) plates of different widths and heights were inserted in the sublayer to block the instability or sweep motion from reaching the surface. Reduction of both the mean and fluctuating surface shear was obtained. The variation in surface shear was found to be extremely sensitive to slight angle of attacks of the plates.

REFERENCES

Bakewell, H. P. and Lumley, J. L. (1967). "Viscous Sublayer and Adjacent Wall Region in Turbulent Pipe Flow," The Physics of Fluids, Vol. 10, p. 1880.

Bendat, J. S. and Piersol, A. G. (1971). "Random Data: Analysis and Measurement Procedures," Wiley-Interscience, New York, NY, pp. 309-312.

Bell, G. J. (1979). "Turbulent Boundary Layer Skin Friction Predictions," M.S. Thesis, Colorado State University.

Blackwelder, R. F. and Kovasznay, L. S. G. (1972). "Time Scales and Correlations in a Turbulent Boundary Layer," Physics of Fluids, Vol. 15, p. 1545.

Blake, W. K. (1970). "Turbulent Boundary Layer Wall Pressure Fluctuations on Smooth and Rough Walls," Journal of Fluid Mechanics, Vol. 44, p. 637.

Blinco, P. and Simons, D. B. (1974). "Characteristics of Turbulent Boundary Shear Stress," Journal of the Engineering Mechanics Division, Proceedings, ASCE, Vol. 100, No. EM2, p. 203.

Brodkey, R. S., Wallace, J. M. and Eckelmann, H. (1974). "Some Properties of Truncated Turbulence Signals in Bounded Shear Flows," Journal of Fluid Mechanics, Vol. 63, Part 3, pp. 209-224.

Brown, G. L. and Thomas, A. S. W. (1977). "Large Structure in a Turbulent Layer," The Physics of Fluids, Vol. 20, No. 10, Part II, pp. 5243-5251.

Cess, R. D. (1961). "Heat Transfer to Laminar Flow Across a Flat Plate with Nonsteady Surface Temperature," Journal of Heat Transfer, Vol. 83C, pp. 274-280.

Chen, C. P. and Blackwelder, R. F. (1978). "Large-scale Motion in a Turbulent Boundary Layer: A Study Using Temperature Contamination," Journal of Fluid Mechanics, Vol. 80, Part I, pp. 1-31.

Clauser, F. H. (1956). "The Turbulent Boundary Layer," Advances of Applied Mechanics, Vol. 4, pp. 1-51, New York, NY.

Cliff, W. C. and Sandborn, V. A. (1973). "Measurements and a Model for Convective Velocities in the Turbulent Boundary Layer," NASA TN D-7416.

Corcos, G. M. (1964). "The Structure of the Turbulent Pressure Field in Boundary Layer Flows," Journal of Fluid Mechanics, Vol. 18, pp. 353-379.

Corino, E. R. and Brodkey, R. S. (1969). "A Visual Investigation of the Wall Region in Turbulent Flow," Journal of Fluid Mechanics, Vol. 37, p. 1.

Corrsin, S. (1957). "Some Current Problems in Turbulent Shear Flow," Naval Hydrodynamics, No. 515, National Academy of Science-National Research Council, Chapter XV.

Eckelmann, H. (1974). "The Structure of the Viscous Sublayer and the Adjacent Wall Region in a Turbulent Channel Flow," Journal of Fluid Mechanics, Vol. 65, Part 3, pp. 439-459.

Falco, R. E. (1977). "Coherent Motions in the Outer Region of Turbulent Boundary Layers," The Physics of Fluids, Vol. 20, No. 10, Part II, pp. s124-s132.

Falco, R. E. (1980). "The Production of Turbulence Near a Wall," AIAA-80-1356, AIAA 13th Fluid and Plasma Dynamics Conference, Snowmass, Colorado, July 14, 1980.

Favre, A. J., Gaviglio, J. J. and Dumas, R. J. (1957a). "Space-time Correlation and Spectra in a Turbulent Boundary Layer," Journal of Fluid Mechanics, Vol. 2, Part 3, pp. 313-342.

Favre, A. J., Gaviglio, J. J. and Dumas, R. J. (1957b). "Further Space-time Correlations of Velocity in a Turbulent Boundary Layer," Journal of Fluid Mechanics, Vol. 3, Part 3, pp. 344-356.

Finn, C. L. and Sandborn, V. A. (1964). "Instrument for Measuring the Intermittency of Quasi-steady Signals," Fluid Mechanics Papers, No. 3, Colorado State University, Fort Collins, CO.

Gottifredi, J. C. and Quiroga, O. D. (1978). "A Simple Analysis of Unsteady Heat Transfer in Impulsive Falkner-Skan Flows," Internal Journal of Heat and Mass Transfer, Vol. 21, pp. 662-664.

Gupta, A. K., Laufer, J. and Kaplan, R. E. (1971). "Spatial Structure in the Viscous Sublayer," Journal of Fluid Mechanics, Vol. 50, p. 493.

Head, M. R. (1958). "Entrainment in the Turbulent Boundary Layer," Aeronautic Research Council, Reports and Memoranda No. 3152.

Kaplan, R. E. and Laufer, J. (1969). "The Intermittenly Turbulent Region of the Boundary Layer," Proceedings of International Congress of Mechanics, 12th, p. 236.

Kim, H. T., Klin, S. J. and Reynolds, W. C. (1971). "The Production of Turbulence Near a Smooth Wall in a Turbulent Boundary Layer," Journal of Fluid Mechanics, Vol. 50, Part 1, pp. 133-160.

Klebanoff, P. S. and Diehle, Z. W. (1952). "Some Features of Artificially Thickened Fully Developed Turbulent Boundary Layers with Zero Pressure Gradient," NACA Report 1110.

Klebanoff, P. S. (1954). "Characteristics of Turbulence in a Boundary Layer with Zero Pressure Gradient," NACA TN3178.

Kline, S. J., Reynolds, W. C., Schraub, F. A. and Runstadler, P. W. (1967). "The Structure of Turbulent Boundary Layers," Journal of Fluid Mechanics, Vol. 30, pp. 741-773.

Kovasznay, L. S. G., Kibens, V. and Blackwelder, R. F. (1970). "Large-scale Motion in the Intermittent Region of a Turbulent Boundary Layer," Journal of Fluid Mechanics, Vol. 41, p. 283.

Kreplin, H. and Eckelmann, H. (1979). "Propagation of Perturbations in the Viscous Sublayer and Adjacent Wall Region," Journal of Fluid Mechanics, Vol. 95, Part 2, pp. 315-322.

Laufer, J. and Narayanan, M. A. B. (1971). "Mean Period of the Turbulent Production Mechanism in a Boundary Layer," Physics of Fluids, Vol. 14, No. 1, January 1971, pp. 182-183.

Mitchell, J. E. and Hanratty, R. J. (1966). "A Study of Turbulence at a Wall Using an Electro-chemical Wall Shear-stress Meter," Journal of Fluid Mechanics, Vol. 26, pp. 199-216.

Nagib, H. M., Corke, T. C. and Guezennec, Y. (1979). "Visualization in Turbulent Flows," Proceedings, Third Engineering Mechanics, Division Specialty Conference, ASCE, September 17-19, Austin, TX.

Rajagopalan, S. and Antonia, R. A. (1980). "Interaction between Large and Small Scale Motions in a Two-dimensional Turbulent Duct Flow," Physics of Fluids, Vol. 23, Part 6, p. 1101.

Rao, K. N., Narasimha, R. and Badri Narayanan, M. A. (1971). "The Bursting Phenomenon in a Turbulent Boundary Layer," Journal of Fluid Mechanics, Vol. 48, p. 339.

Runstadler, P. W., Kline, S. J. and Reynolds, W. C. (1963). "An Investigation of the Flow Structure of the Turbulent Boundary Layer," Mechanical Engineering Department Report MD-8, Stanford University.

Sandborn, V. A. (1979). "Evaluation of the Time Dependent Surface Shear Stress in Turbulent Flows," ASME Paper No. 79-WA/FE-17, August.

Schlichting, H. (1968). "Boundary Layer Theory," McGraw-Hill Book Company, New York, NY, 6e, p. 129.

Townsend, A. A. (1956). "The Structure of Turbulent Shear Flow," Cambridge University Press.

Van Driest, E. R. (1956). "On Turbulent Flow Near a Wall," Journal of the Aeronautical Science, Vol. 23, p. 1007.

Willmarth, W. W. and Lu, S. S. (1971). "Structure of Reynolds Stress Near the Wall," Journal of Fluid Mechanics, Vol. 55, p. 581.

Willmarth, W. W. and Roos, F. W. (1965). "Resolution and Structure of the Wall Pressure Field Beneath a Turbulent Boundary Layer," Journal of Fluid Mechanics, Vol. 22, Part 1, pp. 81-94.

Wills, J. A. B. (1964). "On Convective Velocities in Turbulent Shear Flow," Journal of Fluid Mechanics, Vol. 20, Part 3, pp. 417-432.

Wills, J. A. B. (1967). "A Solution of the Navier-stokes Equations Illustrating the Response of a Laminar Boundary Layer to a Given Change in the External Stream Velocity," Quarterly Journal of Mechanics and Applied Mathematics, Vol. XI, Part 3, p. 303.

Watkins, C. B. (1975). "Unsteady Heat Transfer in Impulsive Falkner-Shan Flows," International Journal Heat Mass Transfer, Vol. 19, pp. 395-407.

APPENDIX A

DERIVATION OF EQUATIONS (19), (20) AND (21)

From Equation (16), we have

$$\frac{\partial \xi}{\partial t^*} = -\frac{\xi}{t^*} \quad \text{and} \quad \frac{\partial \xi}{\partial \eta} = \frac{1}{\sqrt{2t^*}} \tag{A-1}$$

Applying (A-1) and replacing f and g with Equations (17) and (18), the following approximation forms were obtained from Equation (14):

$$-2t^* \left(\frac{dF_o}{d\xi} \cdot \frac{\partial \xi}{\partial t^*} + F_1 + t^* \frac{dF_1}{d\xi} \cdot \frac{\partial \xi}{\partial t^*} + \ldots \right) +$$

$$\left(t^{*1/2} \cdot \frac{dG_1}{d\xi} \cdot \frac{\partial \xi}{\partial \eta} + t^{*3/2} \cdot \frac{dG_2}{d\xi} \cdot \frac{\partial \xi}{\partial \eta} + \ldots \right) +$$

$$F_o + F_1 t^* + \ldots = 0$$

$$\xi \frac{dF_o}{d\xi} - t^* F_1 + t^* \xi \frac{dF_1}{d\xi} + \frac{1}{\sqrt{2}} \frac{dG_2}{d\xi} + F_o + \ldots = 0 \tag{A-2}$$

From Equation (15):

$$(2 - 2t^* F_o - 2t^{*2} F_1 - \ldots)\left(\frac{dF_o}{d\xi} \cdot \frac{\partial \xi}{\partial t^*} + F_1 + t^* \frac{dF_1}{d\xi} \cdot \frac{\partial \xi}{\partial t^*} + \ldots \right) +$$

$$(t^{*1/2} G_1 + t^{*3/2} G_2 + \ldots)\left(\frac{dF_o}{d\xi} \cdot \frac{\partial \xi}{\partial \eta} + t^* \frac{dF_1}{d\xi} \cdot \frac{\partial \xi}{\partial t^*} + \ldots \right) -$$

$$\frac{\partial \xi}{\partial \eta} \cdot \frac{d}{d\xi} \left(\frac{dF_o}{d\xi} \cdot \frac{\partial \xi}{\partial \eta} + t^* \frac{dF_1}{d\xi} \frac{\partial \xi}{\partial \eta} + \ldots \right) = 0 \tag{A-3}$$

$$\left(2 - 2t^* F_o - 2t^{*2} F_1 - \ldots \right)\left(-\frac{\xi}{2t^*} F_o' + F_1 - \frac{\xi}{2} F_1' + \ldots \right)$$

$$+ \left(t^{*1/2} G_1 + t^{*3/2} G_2 + \ldots \right)\left(\frac{1}{\sqrt{2t^*}} F' + \frac{\sqrt{t^*}}{\sqrt{2}} F_1' + \ldots \right) -$$

$$\frac{1}{\sqrt{2t^*}} \cdot \frac{1}{\sqrt{2t^*}} F_o'' - \frac{1}{\sqrt{2t^*}} \cdot \frac{t^*}{\sqrt{2t^*}} F_1'' + \ldots = 0 \tag{A-4}$$

$$- \frac{\xi}{t^*} F_o' + 2F_1 - \xi F_1' + \xi F_o F_o' - 2t^* F_o F_1 + t^* \xi F_o F_1' +$$

$$t^* \xi F_o' F_1 - 2t^{*2} F_1^2 + t^{*2} \xi F_1 F_1' + \frac{1}{\sqrt{2}} F_o' G_1 + \frac{1}{\sqrt{2}} F_1' G_1 +$$

$$\frac{t^*}{\sqrt{2}} F_o' G_2 + \frac{t^{*2}}{\sqrt{2}} F_1' G_2 - \frac{1}{2t^*} F_o'' - \frac{1}{2} F_1'' + \ldots = 0 \qquad \text{(A-5)}$$

Collecting terms of like power of t^* in Equations (A-2), (A-3), (A-4) and (A-5), Equations (19), (20), and (21) were obtained as summarized below:

Order of t^*	From Equation	Resulting Differential Equation
$\frac{1}{t^*}$	(A-2)	$2\xi F_o' + F_o'' = 0$
1	(A-2)	$2\xi F_1' + F_1'' - 4F_1 + 2F_o F_o' + \sqrt{2G_1 F_o}'$
1	(A-1)	$G_1' + \sqrt{2\xi F_o}' + \sqrt{2F_o} = 0$

APPENDIX B

DERIVATION OF EQUATION (32)

To apply the method of Rosezweig, a Laplace transform of f was defined as

$$\phi(s,\eta) = s \int_0^\infty f(t,t^*)\, e^{-st^*} dt^* \tag{B-1}$$

Transformation of Equation (30) yields

$$-\left(\frac{\partial\phi}{\partial\eta}\right)_{\eta=0} \cong s\left(\frac{\sqrt{2}}{\sqrt{s}}\right) \cong -\sqrt{2s} \tag{B-2}$$

where s is very large. For small s, transformation of Equation (31) becomes

$$-\left(\frac{\partial\phi}{\partial\eta}\right)_{\eta=0} \cong -f'(\infty) \tag{B-3}$$

Following Rosenzweig, an approximate expression will be assumed of the form

$$-\left(\frac{\partial\phi}{\partial\eta}\right)_{\eta=0} = a_1 \frac{(s+a_2)}{(s+a_3)^{1/2}} + \ldots \tag{B-4}$$

For small s this reduces to

$$-\left(\frac{\partial\phi}{\partial\eta}\right)_{\eta=0} = \frac{a_1 a_2}{\sqrt{a_3}} + \ldots \tag{B-5}$$

while for large s

$$-\left(\frac{\partial\phi}{\partial\eta}\right)_{\eta=0} = a_1 s^{1/2} + a_1\left(a_2 - \frac{a_3}{2}\right) s^{-1/2} + \ldots \tag{B-6}$$

where a_1, a_2 and a_3 were determined such that Equation (B-5) agree with Equation (B-3), and Equation (B-6) agree with Equation (B-2). We have

$$a_1 = -\sqrt{2}$$

$$a_3 = 2f'^2(\infty)$$

$$a_2 = f'^2(\infty)$$

Thus for any t^*, the approximate form for $\left.\frac{\partial f}{\partial \eta}\right|_{\eta=0}$ was obtained by

$$\left.\frac{\partial f}{\partial \eta}\right|_{\eta=0} = -L^{-1}\left(\left.\frac{\partial \phi}{\partial \eta}\right|_{\eta=0} \cdot \frac{1}{s}\right)$$

$$= -L^{-1}\left\{\frac{a_1(s+a_2)}{s\sqrt{s+a_3}}\right\}$$

$$= -L^{-1}\left\{\frac{a_1}{\sqrt{s+a_3}} + \frac{a_1 a_2}{s\sqrt{s+a_3}}\right\}$$

$$= -L^{-1}\left\{\frac{a_1}{\sqrt{s+a_3}}\right\} - L^{-1}\left\{\frac{a_1 a_2}{s\sqrt{s+a_3}}\right\}$$

$$= \frac{\sqrt{2}}{\sqrt{\pi t^*}} \exp\{-2f'^2(\infty)t^*\} + f'(\infty)\,\mathrm{erf}\{\sqrt{2}t^* f'(\infty)\} \qquad (32)$$

APPENDIX C

FLOW CHART FOR THE COMPUTATION OF $P(\tau_w)$ DUE TO AN ASSUMED VELOCITY DISTRIBUTION $P(U_c)$

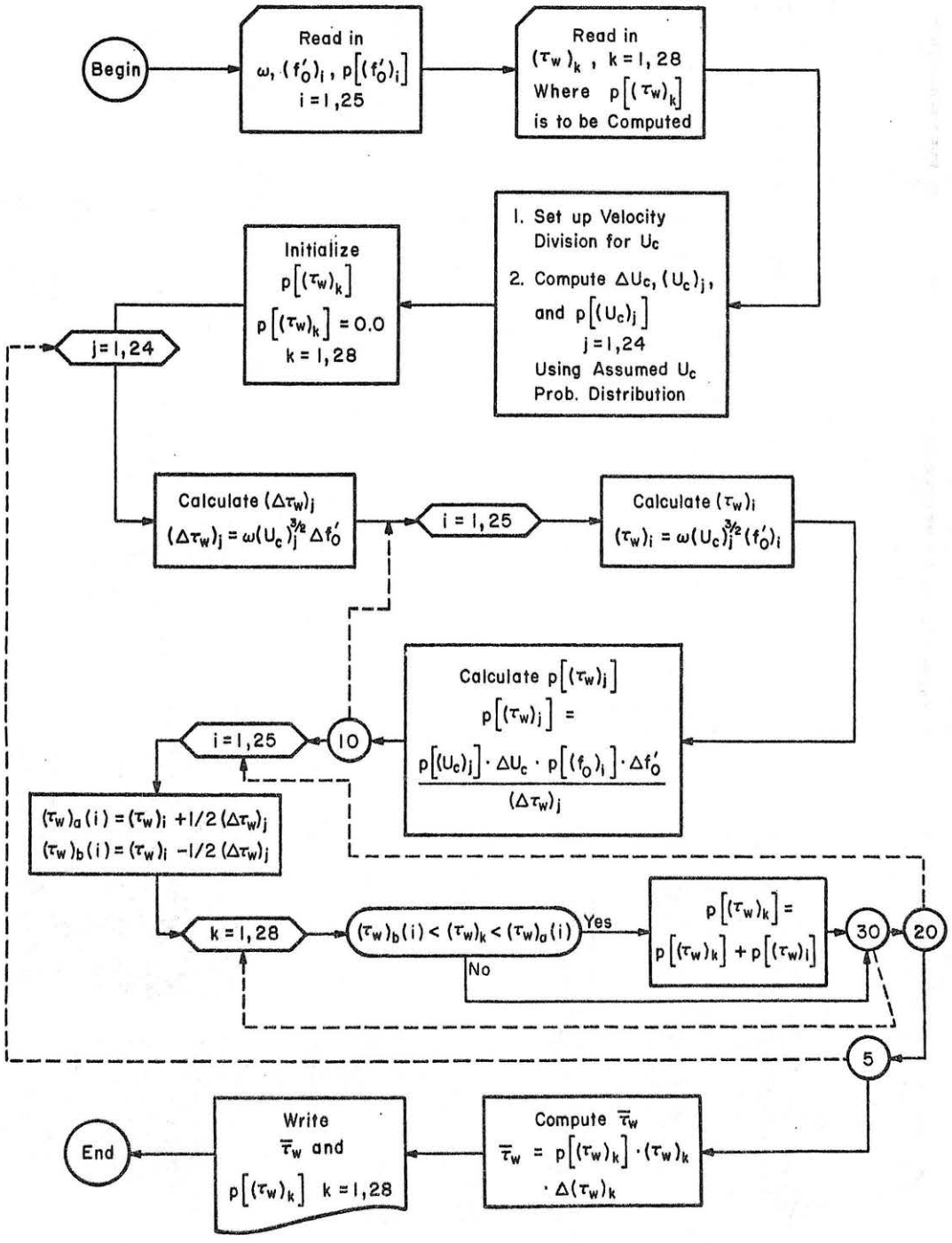

APPENDIX D

EVALUATION OF THE MAXIMUM SPACE-TIME CORRELATIONS

Data for cross-correlation measurements between a boundary-layer-hot-wire placed at coordinate (x,y) and a surface-wire located at coordinate (0.0,0.0) are presented. Positive x is designated as upstream of the surface-wire. $(R_{\tau w}u)_{max}$ is the maximum cross-correlation value obtained at a maximum time delay, Δt_{max}, between the boundary-layer- and surface-hot-wire signals. The boundary-layer-hot-wire signal was delayed with respect to the surface wire.

a) $U_\infty = 10.20$ m/sec, $R_\theta = 4050$

b) $U_\infty = 9.36$ m/sec, $R_\theta = 3500$

c) $U_\infty = 8.55$ m/sec, $R_\theta = 3080$

a) U_∞ = 10.20 m/sec, R_θ = 4050

x (cm)	y (cm)	$(R_{\tau w}u)_{max}$	Δt_{max} 10^{-3} sec	x (cm)	y (cm)	$(R_{\tau w}u)_{max}$	Δt_{max} 10^{-3} sec
2.80	0.03	.260	9.400	0.15	1.27	0.386	2.400
2.80	0.10	.320	7.00	0.15	0.51	0.325	3.30
2.80	0.23	.350	8.00	0.15	0.64	0.327	4.150
2.80	0.36	.390	8.00	0.15	0.76	0.314	5.0
2.80	0.48	.400	8.00	0.15	1.02	0.254	5.800
2.80	0.74	.360	8.900				
2.80	1.24	.233	11.150	0.75	.04	0.695	1.18
				0.75	0.06	0.724	1.94
3.40	0.05	.217	5.790	0.75	0.13	0.599	2.19
3.40	0.13	.299	8.430	0.75	0.18	0.499	2.36
3.40	0.25	.250	8.760	0.75	0.254	0.457	2.82
3.40	0.38	.382	9.130	0.75	0.386	0.390	3.62
3.40	0.51	.371	9.370	0.75	0.510	0.395	3.98
3.40	0.76	.285	9.370	0.75	0.76	0.298	5.35
3.40	1.26	.246	10.160	0.75	1.02	0.273	6.44
4.05	0.06	.260	7.600	0.90	0.64	0.304	-
4.05	0.15	.319	9.800	0.90	0.89	0.273	-
4.05	0.24	.312	9.350	0.90	1.14	0.251	-
4.05	0.37	.320	9.250				
4.05	0.50	.335	10.580	1.30	0.08	0.508	3.100
4.05	0.62	.321	10.420	1.30	0.13	0.496	3.580
4.05	0.75	.282	11.850	1.30	0.254	0.468	4.020
4.05	0.88	.238	11.250	1.30	0.38	0.394	4.370
4.05	1.00	.217	12.850	1.30	0.51	0.395	4.400
4.05	1.26	.173	14.750	1.30	0.76	0.261	6.140
4.65	0.08	.276	8.850	1.70	.254	-	-
4.65	0.17	.186	11.300	1.70	.51	.239	-
4.65	0.25	.197	11.050	1.70	.76	.260	-
4.65	0.38	.233	11.500	1.70	.89	.255	-
4.65	0.51	.317	10.650	1.70	1.02	.233	-
4.65	0.64	.297	10.850	1.70	1.27	.224	-
4.65	0.76	.269	11.150				
4.65	0.89	.254	11.000	1.80	0.03	.692	4.300
4.65	1.02	.237	14.350	1.80	0.10	.672	5.000
4.65	1.27	.222	14.100	1.80	0.23	.372	6.200
				1.80	0.36	.490	5.800
5.10	0.08	.218	10.350	1.80	0.49	-	6.400
5.10	0.25	.293	11.850	1.80	0.74	-	6.600
5.10	0.38	.325	10.650				
5.10	0.45	.329	11.150	2.40	0.08	.419	5.120
5.10	0.56	.326	13.200	2.40	0.13	.313	5.510
				2.40	0.25	.486	-
5.20	.64	.310	13.400	2.40	0.38	.456	8.780
5.20	.89	.251	12.850	2.40	0.51	.430	7.950
5.20	1.02	.212	14.000	2.40	0.76	.344	8.660
				2.40	1.27	.235	9.130

a) U_∞ = 10.20 m/sec, R_θ = 4050 (continued)

x (cm)	y (cm)	$(R_{\tau w}u)_{max}$	Δt_{max} 10^{-3} sec	x (cm)	y (cm)	$(R_{\tau w}u)_{max}$	Δt_{max} 10^{-3} sec
5.80	0.06	.230	11.500	8.30	0.05	.165	13.000
5.80	0.18	.222	14.400	8.30	0.10	.181	14.750
5.80	0.24	.281	12.300	8.30	0.23	.327	15.500
5.80	0.37	.296	12.500	8.30	0.36	.259	16.000
5.80	0.50	.300	12.300	8.30	0.42	.274	16.500
5.80	0.62	.350	14.100	8.30	0.48	.298	17.000
5.80	0.75	.293	12.900	8.30	0.56	.278	17.000
5.80	0.88	.280	14.350	8.30	0.66	.279	17.000
5.80	1.00	.236	14.450	8.30	0.74	.213	16.750
5.80	1.26	.320	14.500	8.30	0.86	.251	18.250
				8.30	0.99	.236	18.250
6.40	0.08	.220	16.100	8.30	1.25	.188	20.000
6.40	0.18	.286	12.300				
6.40	0.25	.268	13.250	8.80	0.08	.167	14.750
6.40	0.38	.231	16.400	8.80	0.13	.165	15.750
6.40	0.51	.302	16.100	8.80	0.25	.252	17.250
6.40	0.64	.257	16.400	8.80	0.38	.248	17.000
6.40	0.76	.309	17.600	8.80	0.45	.279	16.500
6.40	0.89	.296	17.300	8.80	0.51	-	17.500
6.40	1.02	-	14.250	8.80	0.58	.249	18.500
6.40	1.27	.234	15.150	8.80	0.69	.342	17.500
				8.80	0.76	.231	18.250
7.00	0.06	.198	12.130	8.80	0.89	.257	18.000
7.00	0.17	.270	14.800	8.80	1.02	.257	18.500
7.00	0.24	.284	16.180	8.80	1.27	.163	18.500
7.00	0.37	.329	16.100				
7.00	0.50	.321	16.250	10.30	0.23	.196	19.500
7.00	0.62	.284	17.100	10.30	0.36	.118	21.500
7.00	0.75	.278	17.100	10.30	0.42	.203	21.500
7.00	0.88	.244	17.900	10.30	0.48	.201	19.500
7.00	1.00	.241	18.000	10.30	0.56	.184	20.500
7.00	1.26	.236	19.000	10.30	0.66	.248	20.250
				10.30	0.74	.264	20.500
7.60	0.08	.154	12.800	10.30	0.86	.279	21.000
7.60	0.18	.214	16.150	10.30	0.99	.236	21.500
7.60	0.25	.245	16.100				
7.60	0.38	.213	19.000	10.80	0.25	.205	18.500
7.60	0.51	.272	16.350	10.80	0.38	.230	21.500
7.60	0.64	.290	16.200	10.80	0.45	.258	22.000
7.60	0.76	.267	16.800	10.80	0.51	.241	21.500
7.60	0.89	.300	18.550	10.80	0.58	.255	21.500
7.60	1.02	.292	22.400	10.80	0.69	.269	21.250
7.60	1.27	.269	-	10.80	0.76	.263	21.000
				10.80	0.86	.236	21.500
				10.80	1.02	.281	22.750

a) U_∞ = 10.20 m/sec, R_θ = 4050 (continued)

x (cm)	y (cm)	$(R_{\tau w}u)_{max}$	Δt_{max}	x (cm)	y (cm)	$(R_{\tau w}u)_{max}$	Δt_{max} 10^{-3} sec
-0.15	0.05	.770	.700	-2.10	0.03	497	-3.25
-0.15	0.10	-	-	-2.10	0.08	570	-2.55
-0.15	0.15	.728	1.250	-2.10	0.13	519	-1.40
-0.15	0.20	.516	1.500	-2.10	0.18	500	-0.90
-0.15	0.25	.514	2.000	-2.10	0.23	470	-0.46
-0.15	0.31	.470	2.750	-2.10	0.36	393	-0.25
-0.15	0.38	.463	2.900	-2.10	0.48	386	0.90
-0.15	0.51	.400	3.250				
-0.15	0.76	.295	5.400	-2.25	0.64	.355	1.000
-0.15	1.27	.268	7.400	-2.25	0.76	.329	2.250
				-2.25	0.89	.315	4.650
-0.30	0.45	-	4.000	-2.25	1.02	.275	2.500
-0.30	0.64	.399	4.750	-2.25	1.14	.256	2.500
-0.30	0.89	.292	6.000	-2.25	1.27	.240	6.000
-0.30	1.02	.262	-				
0.30	1.14	-	6.500	-2.60	0.05	.422	-3.900
				-2.60	0.10	.403	-3.800
-0.75	0.03	.804	-0.500	-2.60	0.15	.470	-2.700
-0.75	0.08	-	-	-2.60	0.20	.462	-2.700
-0.75	0.13	.762	0.0	-2.60	0.25	.414	-2.200
-0.75	0.18	.516	1.500	-2.60	0.38	.425	-1.400
-0.75	0.23	.436	1.600	-2.60	0.51	.358	-0.50
-0.75	0.28	.469	1.80				
-0.75	0.36	.436	2.150	-2.75	0.58	.356	0.750
-0.75	0.48	.364	-	-2.75	0.71	.349	1.600
-0.75	0.51	.306	2.000	-2.75	0.84	.283	2.900
-0.75	0.64	.418	3.500	-2.75	0.97	.259	2.500
-0.75	0.74	.326	4.300	-2.75	1.09	.239	3.100
-0.75	0.77	(.314)	5.500	-2.75	1.22	.241	2.500
-0.75	0.89	.297	6.250				
-0.75	1.02	.271	6.000	-3.20	0.03	.385	-5.200
-0.75	1.25	.250	7.150	-3.20	0.08	.375	-4.150
-0.75	1.27	.238	7.250	-3.20	0.13	.529	-3.900
				-3.20	0.18	.537	-3.500
-1.25	0.46	(.198)	-	-3.20	0.23	.483	-3.000
-1.25	0.58	.362	3.250	-3.20	0.36	.517	-1.100
-1.25	0.72	.350	-	-3.20	0.48	.546	-2.500
-1.25	0.84	.317	6.000				
-1.25	0.97	-	6.000	-3.85	0.10	.244	-6.500
-1.25	1.22	.275	7.000	-3.85	0.18	.271	-4.750
				-3.85	0.25	.337	-3.500
-1.50	0.05	.562	-2.500	-3.85	0.37	.263	-1.750
-1.50	0.10	.591	-2.950	-3.85	0.51	.343	-3.000
-1.50	0.15	.622	-1.400	-3.85	0.64	.315	-0.5
-1.50	0.20	.516	-0.900	-3.85	0.76	.354	-0.25
-1.50	0.25	.456	-0.300	-3.85	0.89	.293	-
-1.50	0.38	.374	0.500	-3.85	1.02	.289	-
-1.50	0.51	.343	1.300	-3.85	1.14	.260	1.750
				-3.85	1.27	.220	1.500

a) U_∞ = 10.20 m/sec, R_θ = 4050 (continued)

x (cm)	y (cm)	$(R_{\tau w}u)_{max}$	Δt_{max} 10^{-3} sec
-4.35	0.05	.273	-6.250
-4.35	0.14	.301	-4.750
-4.35	0.20	.356	-4.750
-4.35	0.33	.363	-3.500
-4.35	0.46	.372	-4.000
-4.35	0.58	.333	-2.500
-4.35	0.71	.272	-1.50
-4.35	0.84	.282	-1.000
-4.35	0.97	.268	-0.250
-4.35	1.09	.249	0.500
-4.35	1.22	.220	0.500
-5.25	0.10	.295	-7.000
-5.25	0.25	.308	-5.000
-5.25	0.38	.300	-4.500
-5.25	0.51	.443	-4.000
-5.25	0.64	.303	-3.000
-5.25	0.76	.336	-2.500
-5.75	0.05	.258	-8.250
-5.75	0.20	.360	-6.500
-5.75	0.33	.363	-5.500
-5.75	0.46	.319	-4.750
-5.75	0.58	.325	-4.000
-5.75	0.71	.315	-3.250

b) U_∞ = 9.36 m/sec, R_θ = 3500 (continued)

x (cm)	y (cm)	$(R_{\tau w}u)_{max}$	Δt_{max} 10^{-3} sec	x (cm)	y (cm)	$(R_{\tau w}u)_{max}$	Δt_{max} 10^{-3} sec
10.8	0.127	0.174	22.00	8.3	0.051	0.172	13.25
10.8	0.254	0.168	22.00	8.3	0.102	0.176	16.00
10.8	0.381	0.180	22.50	8.3	0.229	0.203	17.00
10.8	0.445	0.238	22.50	8.3	0.356	0.392	17.00
10.8	0.508	0.232	23.50	8.3	0.419	0.313	18.75
10.8	0.584	0.235	22.50	8.3	0.483	0.301	18.00
10.8	0.686	0.267	23.00	8.3	0.559	0.261	17.75
10.8	0.762	0.284	23.00	8.3	0.660	0.236	20.00
10.8	0.889	0.276	22.75	8.3	0.737	0.199	18.75
10.8	1.016	0.252	23.50	8.3	0.864	0.236	18.50
				8.3	0.991	0.241	19.25
10.30	0.102	0.156	20.00	8.3	1.245	0.187	22.00
10.30	0.229	0.182	21.00				
10.30	0.356	0.191	22.25	7.6	0.076	0.176	14.10
10.30	0.419	0.216	22.25	7.6	0.178	0.165	15.75
10.30	0.483	0.198	22.00	7.6	0.254	0.222	17.75
10.30	0.559	0.233	22.50	7.6	0.381	0.261	16.35
10.30	0.660	0.275	23.25	7.6	0.508	0.244	18.30
10.30	0.737	0.257	22.50	7.6	0.635	0.284	17.00
10.30	0.864	0.235	23.00	7.6	0.762	0.299	16.75
10.30	0.991	0.200	23.00	7.6	0.889	0.247	20.80
				7.6	1.016	0.273	16.50
8.8	0.076	0.080	15.50	7.6	1.270	0.207	17.50
8.8	0.127	0.194	16.00				
8.8	0.254	0.223	17.50	7.0	0.051	0.190	13.80
8.8	0.381	0.227	18.25	7.0	0.152	0.223	14.40
8.8	0.445	0.256	18.00	7.0	0.229	0.246	16.25
8.8	0.508	-	20.00	7.0	0.356	0.299	16.10
8.8	0.584	0.262	21.50	7.0	0.483	0.295	18.50
8.8	0.686	0.255	21.00	7.0	0.610	0.254	18.50
8.8	0.762	0.237	18.75	7.0	0.762	0.296	20.00
8.8	0.889	0.243	19.50	7.0	0.864	0.250	20.00
8.8	1.016	0.227	20.50	7.0	0.991	0.216	20.25
8.8	1.270	0.145	23.75	7.0	1.245	0.190	22.00

b) U_∞ = 9.36 m/sec, R_θ = 3500 (continued)

x (cm)	y (cm)	$(R_{\tau w}u)_{max}$	Δt_{max} 10^{-3} sec	x (cm)	y (cm)	$(R_{\tau w}u)_{max}$	Δt_{max} 10^{-3} sec
6.4	0.076	0.203	11.00	4.65	0.076	0.197	9.55
6.4	0.178	0.214	12.35	4.65	0.178	0.285	11.10
6.4	0.254	0.210	16.10	4.65	0.254	0.292	11.30
6.4	0.381	0.288	14.40	4.65	0.381	0.378	11.10
6.4	0.508	0.316	14.10	4.65	0.508	0.340	-
6.4	0.635	0.261	13.55	4.65	0.635	0.302	12.00
6.4	0.762	0.280	14.35	4.65	0.762	0.290	12.50
6.4	0.889	0.203	14.60	4.65	0.889	0.246	12.65
6.4	1.016	0.246	16.30	4.65	1.016	0.243	13.50
6.4	1.270	-	17.00	4.65	1.270	-	14.00
5.90	0.064	0.213	15.75	4.20	0.064	0.242	9.00
5.90	0.152	0.204	9.75	4.20	0.152	0.298	10.65
5.90	0.229	0.214	14.00	4.20	0.241	0.313	10.50
5.90	0.356	0.284	14.43	4.20	0.368	0.338	11.05
5.90	0.483	0.321	14.25	4.20	0.495	0.345	11.15
5.90	0.610	0.267	14.25	4.20	0.622	0.322	11.10
5.90	0.737	0.282	14.40	4.20	0.749	0.282	11.50
5.90	0.864	0.254	14.75	4.20	0.876	0.265	12.60
5.90	0.991	0.297	16.65	4.20	1.003	0.232	14.15
5.90	1.245	0.275	16.10	4.20	1.257	-	16.30
5.2	0.076	0.173	11.50	3.40	0.051	0.259	7.64
5.2	0.254	0.274	14.00	3.40	0.127	0.306	8.50
5.2	0.381	0.291	14.00	3.40	0.254	0.390	-
5.2	0.445	0.298	13.50	3.40	0.381	0.365	9.29
5.2	0.508	0.285	14.00	3.40	0.508	0.229	9.06
5.2	0.635	0.282	14.25	3.40	0.762	0.260	-
5.2	0.762	0.279	14.00	3.40	1.270	0.240	11.73
5.2	0.889	0.259	13.00				
5.2	1.016	0.250	14.75				

b) U_∞ = 9.36 m/sec, R_θ = 3500 (continued)

x (cm)	y (cm)	$(R_{\tau w}u)_{max}$	Δt_{max} 10^{-3} sec	x (cm)	y (cm)	$(R_{\tau w}u)_{max}$	Δt_{max} 10^{-3} sec
2.40	0.051	0.425	5.35	0.9	0.635	0.308	6.50
2.40	0.127	0.318	7.64	0.9	0.889	0.283	7.50
2.40	0.254	0.401	9.05	0.9	1.143	0.229	9.50
2.40	0.381	0.368	8.43				
2.40	0.508	0.359	8.42	0.15	0.025	0.728	1.10
2.40	0.762	0.395	10.24	0.15	0.076	-	1.25
2.40	1.270	0.148	8.19	0.15	0.127	0.663	1.75
				0.15	0.178	0.538	3.00
1.70	0.127	0.434	5.25	0.15	0.229	0.489	3.30
1.70	0.254	0.358	-	0.15	0.279	0.419	3.60
1.70	0.381	0.343	7.00	0.15	0.381	0.351	3.25
1.70	0.508	0.320	6.50	0.15	0.508	0.328	4.50
1.70	0.635	0.314	7.50	0.15	0.635	0.328	5.50
1.70	0.762	0.296	8.75	0.15	0.762	0.292	6.50
1.70	0.889	0.262	9.50	0.15	0.889	0.278	6.75
1.70	1.016	0.242	9.50	0.15	1.016	0.241	7.00
1.30	0.076	0.492	3.48	-0.15	0.051	0.800	0.60
1.30	0.127	0.473	3.98	-0.15	0.102	0.770	1.10
1.30	0.254	0.381	4.45	-0.15	0.152	0.611	1.25
1.30	0.381	0.395	4.69	-0.15	0.203	0.522	1.50
1.30	0.508	0.366	5.08	-0.15	0.254	0.474	1.75
1.30	0.762	0.306	7.80	-0.15	0.305	0.456	2.75
1.30	1.270	-	9.15	-0.15	0.381	0.453	3.50
				-0.15	0.508	0.360	3.75
0.7	0.051	0.585	1.25	-0.15	0.762	0.326	5.25
0.7	0.102	0.769	1.40	-0.15	0.889	0.279	5.50
0.7	0.152	0.600	2.00	-0.15	1.016	0.262	7.00
0.7	0.203	0.526	2.55	-0.15	1.270	0.269	7.90
0.7	0.254	0.471	3.00				
0.7	0.305	0.438	4.20				
0.7	0.381	0.432	3.75				
0.7	0.508	0.402	4.10				
0.7	0.762	0.329	5.50				

b) U_∞ = 9.36 m/sec, R_θ = 3500 (continued)

x (cm)	y (cm)	$(R_{\tau w}u)_{max}$	Δt_{max} 10^{-3} sec	x (cm)	y (cm)	$(R_{\tau w}u)_{max}$	Δt_{max} 10^{-3} sec
-0.75	0.025	0.796	-0.50	-2.10	0.025	0.472	-3.25
-0.75	0.076	0.798	0.25	-2.10	0.076	0.464	-2.65
-0.75	0.127	0.661	1.25	-2.10	0.127	0.418	-2.15
-0.75	0.178	0.577	1.75	-2.10	0.178	0.442	-1.50
-0.75	0.229	0.458	2.50	-2.10	0.229	0.480	-0.25
-0.75	0.279	0.422	1.25	-2.10	0.356	0.425	-0.25
-0.75	0.356	0.432	2.25	-2.10	0.483	0.385	1.25
-0.75	0.483	0.366	3.15				
-0.75	0.508	0.321	3.00	-2.25	0.635	0.305	0.75
-0.75	0.635	0.345	4.20	-2.25	0.762	0.306	2.75
-0.75	0.737	0.314	5.50	-2.25	0.889	0.314	3.50
-0.75	0.762	0.300	5.00	-2.25	1.016	0.205	4.10
-0.75	0.889	0.287	-	-2.25	1.143	0.245	6.50
-0.75	1.016	0.270	7.00	-2.25	1.270	0.232	5.00
-0.75	1.245	0.285	7.05				
-0.75	1.270	0.256	10.00	-2.60	0.051	0.411	-3.00
				-2.60	0.102	0.432	-3.90
-1.50	0.051	0.488	-2.45	-2.60	0.152	0.470	-3.25
-1.50	0.102	0.552	-1.40	-2.60	0.203	0.458	-3.05
-1.50	0.152	0.800	-0.80	-2.60	0.254	0.421	-2.70
-1.50	0.203	0.510	-0.40	-2.60	0.381	0.440	-1.15
-1.50	0.254	0.493	-0.40	-2.60	0.508	0.400	-0.60
-1.50	0.381	0.379	5.20				
-1.50	0.508	0.361		-2.75	0.584	0.307	0.62
				-2.75	0.711	0.395	1.50
-1.25	0.584	0.335	3.50	-2.75	0.838	0.297	1.30
-1.25	0.711	0.282	4.50	-2.75	0.965	0.302	3.30
-1.25	0.838	0.330	6.25	-2.75	1.092	0.254	2.00
-1.25	0.965	0.305	6.25	-2.75	1.219	0.291	-
-1.25	1.219	0.263	10.00				

b) U_∞ = 9.36 m/sec, R_θ = 3500 (continued)

x (cm)	y (cm)	$(R_{\tau w}u)_{max}$	Δt_{max} 10^{-3} sec	x (cm)	y (cm)	$(R_{\tau w}u)_{max}$	Δt_{max} 10^{-3} sec
-3.20	0.025	0.379	-5.92	-5.25	0.102	0.283	-9.50
-3.20	0.076	0.471	-4.85	-5.25	0.254	0.290	-6.25
-3.20	0.127	0.510	-3.85	-5.25	0.381	0.327	-3.75
-3.20	0.178	0.530	-3.40	-5.25	0.508	0.257	-4.00
-3.20	0.229	0.453	-3.00	-5.25	0.635	0.307	-4.00
-3.20	0.356	0.439	-2.25	-5.25	0.762	0.314	-2.50
-3.20	0.483	0.415	-1.00	-5.25	0.889	0.295	-
				-5.25	1.016	0.316	-0.50
-3.85	0.102	0.239	-4.50	-5.25	1.143	0.261	1.00
-3.85	0.178	0.327	-4.50	-5.25	1.270	0.200	2.25
-3.85	0.254	0.282	-4.00				
-3.85	0.368	0.319	-4.00	-5.75	0.051	0.254	-8.50
-3.85	0.508	0.371	-3.00	-5.75	0.203	0.316	-6.50
-3.85	0.762	0.324	-	-5.75	0.330	0.317	-4.75
-3.85	0.889	0.309	-0.50	-5.75	0.457	0.323	-3.00
-3.85	1.016	0.273	1.00	-5.75	0.584	0.349	-4.50
-3.85	1.143	0.266	1.25	-5.75	0.711	0.295	-2.00
-3.85	1.270	0.228	1.50	-5.75	0.838	0.296	-1.50
				-5.75	0.965	0.274	-0.50
-4.35	0.051	0.181	-7.75	-5.75	1.092	0.258	-
-4.35	0.127	0.309	-4.50	-5.75	1.219	0.252	1.10
-4.35	0.203	0.326	-4.50				
-4.35	0.330	0.356	-3.75	-6.45	0.127	0.314	-9.00
-4.35	0.457	0.366	-3.50	-6.45	0.254	0.304	-8.50
-4.35	0.584	0.326	-2.25	-6.45	0.381	0.335	-7.50
-4.35	0.711	0.414	-0.60	-6.45	0.508	0.349	-7.00
-4.35	0.838	0.296	1.00	-6.45	0.635	0.317	-6.03
-4.35	0.965	0.263	1.00	-6.45	0.762	0.448	-4.00
-4.35	1.092	0.270	1.50	-6.45	0.889	0.263	-4.00
-4.35	1.219	0.209	2.40	-6.45	1.016	0.274	-3.00
				-6.45	1.143	0.245	-
				-6.45	1.270	0.230	-0.50
				-6.95	0.076	0.314	-10.50
				-6.95	0.203	0.327	-8.50
				-6.95	0.330	0.409	-7.75
				-6.95	0.457	0.305	-7.00
				-6.95	0.584	0.265	-4.00
				-6.95	0.711	0.349	-4.00
				-6.95	0.838	0.279	-4.00
				-6.95	0.965	0.272	-4.00
				-6.95	1.092	0.280	-2.00
				-6.95	1.219	0.273	-0.75

c) U_∞ = 8.55 m/sec, R_θ = 3080

x (cm)	y (cm)	$(R_{\tau w}u)_{max}$	Δt_{max} 10^{-3} sec	x (cm)	y (cm)	$(R_{\tau w}u)_{max}$	Δt_{max} 10^{-3} sec
10.8	0.127	0.168	24.50	8.3	0.051	0.175	16.00
10.8	0.254	0.222	21.75	8.3	0.102	0.163	16.50
10.8	0.381	0.227	25.00	8.3	0.229	0.218	21.25
10.8	0.445	0.200	24.75	8.3	0.356	0.290	21.50
10.8	0.508	0.261	24.00	8.3	0.419	0.305	21.50
10.8	0.584	0.239	24.50	8.3	0.483	0.268	21.50
10.8	0.686	0.296	28.00	8.3	0.559	0.260	21.50
10.8	0.762	0.284	26.00	8.3	0.660	0.245	21.50
10.8	0.889	0.270	25.25	8.3	0.737	0.283	21.50
10.8	1.016	0.292	25.00	8.3	0.864	0.270	20.50
				8.3	0.991	0.257	21.75
10.3	0.102	0.170	21.50	8.3	1.245	0.206	22.50
10.3	0.229	0.196	22.00				
10.3	0.356	0.188	24.00	7.6	0.076	0.161	15.65
10.3	0.419	0.188	22.25	7.6	0.178	0.172	17.65
10.3	0.483	0.200	23.25	7.6	0.254	0.239	17.00
10.3	0.559	0.208	23.25	7.6	0.381	0.244	18.20
10.3	0.660	0.310	25.00	7.6	0.508	0.278	19.00
10.3	0.737	0.240	23.50	7.6	0.635	0.269	20.25
10.3	0.864	0.220	23.50	7.6	0.762	0.318	21.00
10.3	0.991	0.198	26.75	7.6	0.889	0.287	17.00
				7.6	1.016	0.242	18.50
8.8	0.076	0.179	18.50				
8.8	0.127	0.153	22.00	7.0	0.051	0.208	14.20
8.8	0.254	0.218	22.00	7.0	0.152	0.211	17.15
8.8	0.381	0.286	22.00	7.0	0.229	0.236	16.60
8.8	0.445	0.287	21.50	7.0	0.356	0.267	18.00
8.8	0.508	0.288	21.50	7.0	0.483	0.286	14.50
8.8	0.584	0.454	22.00	7.0	0.610	0.290	15.50
8.8	0.686	0.264	21.50	7.0	0.762	0.250	15.00
8.8	0.762	0.238	22.00	7.0	0.864	0.191	16.75
8.8	0.889	0.254	22.50	7.0	0.991	0.241	16.00
8.8	1.016	0.271	21.75	7.0	1.245	0.176	16.25
8.8	1.270	0.200	22.00				

c) U_∞ = 8.55 m/sec, R_θ = 3080 (continued)

x (cm)	y (cm)	$(R_{\tau w}u)_{max}$	Δt_{max} 10^{-3} sec	x (cm)	y (cm)	$(R_{\tau w}u)_{max}$	Δt_{max} 10^{-3} sec
6.4	0.076	0.231	12.60	4.7	0.076	0.233	10.15
6.4	0.178	0.205	14.80	4.7	0.178	0.290	12.50
6.4	0.254	0.218	15.40	4.7	0.254	0.322	11.50
6.4	0.381	0.305	14.00	4.7	0.381	0.320	12.00
6.4	0.508	0.320	15.62	4.7	0.508	0.320	11.20
6.4	0.635	0.290	15.70	4.7	0.635	0.290	12.10
6.4	0.762	0.260	16.00	4.7	0.762	0.260	13.25
6.4	0.889	0.283	16.00	4.7	0.889	0.287	13.00
6.4	1.016	0.218	18.40	4.7	1.016	0.240	14.45
6.4	1.270	0.196	19.20	4.7	1.270	0.190	15.00
5.8	0.051	0.239	12.45	4.1	0.064	0.250	10.00
5.8	0.165	0.239	12.50	4.1	0.165	0.275	10.65
5.8	0.241	0.240	13.75	4.1	0.241	0.297	11.80
5.8	0.368	0.297	15.40	4.1	0.368	0.314	11.10
5.8	0.495	0.281	16.00	4.1	0.495	0.326	12.45
5.8	0.622	0.272	15.20	4.1	0.622	0.293	11.90
5.8	0.749	0.225	15.30	4.1	0.749	0.269	12.08
5.8	0.876	0.226	16.85	4.1	0.876	0.270	11.20
5.8	1.003	0.246	17.65	4.1	1.003	0.205	13.55
5.8	1.257	0.177	18.00	4.1	1.257	0.100	13.60
5.2	0.076	0.200	12.50	3.4	0.051	0.309	9.30
5.2	0.254	0.251	13.75	3.4	0.127	0.325	9.17
5.2	0.381	0.293	16.00	3.4	0.254	0.376	10.16
5.2	0.508	0.292	15.00	3.4	0.381	0.494	9.53
5.2	0.635	0.258	14.25	3.4	0.508	0.266	9.84
5.2	0.762	0.286	16.00	3.4	0.762	0.299	10.50
5.2	0.889	0.248	17.00	3.4	1.270	0.189	11.73
5.2	1.016	0.249	16.00				

c) U_∞ = 8.55 m/sec, R_θ = 3080 (continued)

x (cm)	y (cm)	$(R_{\tau w}u)_{max}$	Δt_{max} 10^{-3} sec	x (cm)	y (cm)	$(R_{\tau w}u)_{max}$	Δt_{max} 10^{-3} sec
2.4	0.051	0.345	6.46	0.15	0.025	0.685	0.75
2.4	0.127	0.424	7.64	0.15	0.076	-	1.025
2.4	0.254	0.370	8.40	0.15	0.127	-	2.45
2.4	0.381	0.411	8.62	0.15	0.178	0.550	3.00
2.4	0.508	0.350	8.40	0.15	0.279	0.449	3.40
2.4	0.762	0.330	9.60	0.15	0.356	0.378	4.00
2.4	1.270	0.209	11.80	0.15	0.508	0.322	5.00
				0.15	0.635	0.333	5.50
1.7	0.127	0.496	5.50	0.15	0.762	0.292	5.75
1.7	0.254	0.400	6.50	0.15	0.889	0.272	6.50
1.7	0.381	0.340	7.00	0.15	1.016	0.246	7.50
1.7	0.508	0.342	7.50				
1.7	0.635	0.301	8.75	-0.15	0.051	0.795	0.65
1.7	0.762	0.292	9.00	-0.15	0.102	0.693	1.00
1.7	0.889	0.290	9.50	-0.15	0.152	0.639	1.30
1.7	1.016	0.253	9.50	-0.15	0.203	0.517	2.25
				-0.15	0.254	0.452	2.50
1.3	0.051	0.462	3.74	-0.15	0.305	0.446	3.25
1.3	0.254	0.441	4.92	-0.15	0.381	0.390	3.60
1.3	0.381	0.393	4.72	-0.15	0.508	0.382	5.20
1.3	0.508	0.332	5.87	-0.15	0.762	0.278	6.15
1.3	0.762	0.325	8.19	-0.15	1.270	0.294	10.50
0.7	0.51	0.590	1.65	-0.75	0.025	0.774	-0.55
0.7	0.102	0.740	1.85	-0.75	0.076	0.716	0.40
0.7	0.203	0.457	3.10	-0.75	0.127	0.617	1.30
0.7	0.305	0.409	4.15	-0.75	0.178	0.505	
0.7	0.381	0.432	3.90	-0.75	0.229	0.465	1.50
0.7	0.508	0.436	5.70	-0.75	0.279	0.448	2.50
				-0.75	0.356	0.388	2.99
0.9	0.635	0.309	6.00	-0.75	0.483	0.352	3.75
0.9	0.762	0.335	7.00	-0.75	0.635	0.338	6.50
0.9	0.889	0.249	9.00	-0.75	0.762	0.310	6.00
0.9	0.143	0.240	10.00	-0.75	0.889	0.313	6.25
				-0.75	1.016	0.288	7.00

c) U_∞ = 8.55 m/sec, R_θ = 3080 (continued)

x (cm)	y (cm)	$(R_{\tau w}u)_{max}$	Δt_{max} 10^{-3} sec	x (cm)	y (cm)	$(R_{\tau w}u)_{max}$	Δt_{max} 10^{-3} sec
-2.1	0.025	0.548	-3.90	-3.85	0.102	0.250	-8.50
-2.1	0.076	0.444	-3.05	-3.85	0.178	0.263	-6.25
-2.1	0.127	0.533	-1.90	-3.85	0.254	0.316	-4.00
-2.1	0.178	0.432	-1.80	-3.85	0.381	0.269	-3.25
-2.1	0.229	0.488	-0.25	-3.85	0.508	0.315	-2.50
-2.1	0.356	0.384	-0.25	-3.85	0.635	0.356	-4.00
-2.1	0.483	0.370	0.0	-3.85	0.762	0.300	-1.25
				-3.85	0.889	0.291	-0.25
-2.25	0.635	0.295	2.25	-3.85	1.016	0.302	1.00
-2.25	0.762	0.279	2.50	-3.85	1.270	0.224	1.50
-2.25	0.889	0.286	3.00				
-2.25	1.016	0.261	3.25	-4.35	0.051	0.252	-8.25
-2.25	1.270	0.221	7.00	-4.35	0.127	0.326	-6.00
				-4.35	0.203	0.300	-7.50
-2.6	0.051	0.519	-5.00	-4.35	0.330	0.331	-4.00
-2.6	0.102	0.434	-4.00	-4.35	0.457	0.344	-3.50
-2.6	0.152	0.474	-3.20	-4.35	0.584	0.332	-1.50
-2.6	0.203	0.477	-3.50	-4.35	0.711	0.386	-0.50
-2.6	0.254	0.421	-2.70	-4.35	0.838	0.241	0.50
-2.6	0.381	0.406	-1.50	-4.35	0.965	0.313	-0.25
-2.6	0.508	0.366	-0.90	-4.35	1.219	0.237	1.00
-2.75	0.711	0.285	1.50	-5.25	0.102	0.291	-8.50
-2.75	0.838	0.340	1.20	-5.25	0.254	0.288	-6.00
-2.75	0.965	0.242	3.00	-5.25	0.381	0.288	-4.50
-2.75	1.219	0.250	6.25	-5.25	0.508	0.300	-4.00
				-5.25	0.635	0.332	-4.50
-3.2	0.025	0.328	-6.65	-5.25	0.762	0.329	-2.00
-3.2	0.076	0.521	-5.85	-5.25	0.889	0.280	-3.25
-3.2	0.127	0.516	-4.10	-5.25	1.016	0.274	-4.50
-3.2	0.178	0.523	-3.80	-5.25	1.270	0.209	1.50
-3.2	0.229	0.486	-3.00				
-3.2	0.356	0.411	-1.40				
-3.2	0.483	0.420	-0.50				

c) U_∞ = 8.55 m/sec, R_θ = 3080 (continued)

x (cm)	y (cm)	$(R_{\tau w}u)_{max}$	Δt_{max} 10^{-3} sec
-5.75	0.051	0.279	1.05
-5.75	0.203	0.297	-7.25
-5.75	0.330	0.357	-6.25
-5.75	0.457	0.305	-4.50
-5.75	0.584	0.320	4.50
-5.75	0.711	0.303	0.90
-5.75	0.838	0.235	-2.75
-5.75	0.965	0.235	-1.10
-5.75	1.219	0.277	1.00
-6.45	0.127	0.269	-10.00
-6.45	0.254	0.339	-8.50
-6.45	0.381	0.353	-7.75
-6.45	0.508	0.346	-
-6.45	0.635	0.276	-6.50
-6.45	0.762	0.405	-4.50
-6.45	0.889	0.273	-3.00
-6.45	1.016	0.281	-3.75
-6.45	1.143	0.260	-0.70
-6.45	1.270	0.239	-0.50
-6.95	0.076	0.274	-12.75
-6.95	0.203	0.322	-10.50
-6.95	0.330	0.324	-8.00
-6.95	0.457	0.343	-7.75
-6.95	0.584	0.445	-6.50
-6.95	0.711	0.274	-5.50
-6.95	0.838	0.262	-5.25
-6.95	0.965	0.261	-4.00
-6.95	1.092	0.259	-3.50
-6.95	1.219	0.247	-1.50

Table 2. Evaluation of $\left.\frac{\partial f}{\partial \eta}\right|_{\eta=0}$ Equation (32).

Nondimensional Time t^*	Nondimensional Shear Stress $\left.\frac{\partial f}{\partial \eta}\right\|_{\eta=0}$
0.0036	3.244
0.0082	8.829
0.0145	6.622
0.0227	5.298
0.0327	4.415
0.0510	3.532
0.0655	3.117
0.0907	2.649
0.1098	2.409
0.1533	2.039
0.2041	1.768
0.2622	1.562
0.3450	1.363
0.4391	1.211
0.5671	1.069
0.7896	0.914
0.9291	0.8475
1.0800	0.7919
1.2421	0.7449
1.6005	0.6707
2.0042	0.6162
2.5008	0.5724
3.2121	0.5342
3.8334	0.5137
4.7035	0.4962
5.7344	0.4847
6.9477	0.4774
8.1026	0.4740
9.0732	0.4722

Table 3. Histogram and estimated probability density for f'_o. Values of f'_o between $t^* = 0$ and $t^* = 4.0$ were used.

$$P_i = P\,[(f'_o)_i] = \frac{N_i}{N_o}\,\frac{1}{\Delta f'_o}$$

$$N_o = 200\ ,\ \Delta f'_o = 0.1$$

$(f'_o)_i$ window	N_i	P_i	$(f'_o)_i$ window	N_i	P_i
0.5 - 0.6	95.0	4.75	3.0 - 3.1	0.25	0.0125
0.6 - 0.7	32.0	1.60	3.1 - 3.2	0.23	0.0115
0.7 - 0.8	20.0	1.00	3.2 - 3.3	0.20	0.0100
0.8 - 0.9	12.5	0.625	3.3 - 3.4	0.20	0.0100
0.9 - 1.0	7.8	0.390	3.4 - 3.5	0.18	0.0090
1.0 - 1.1	5.9	0.295	3.5 - 3.6	0.15	0.0075
1.1 - 1.2	4.8	0.240	3.6 - 3.7	0.13	0.0065
1.2 - 1.3	3.4	0.170	3.7 - 3.8	0.11	0.0055
1.3 - 1.4	2.7	0.135	3.8 - 3.9	0.10	0.0050
1.4 - 1.5	2.0	0.100	3.9 - 4.0	0.09	0.0045
1.5 - 1.6	1.9	0.095	4.0 - 4.1	0.06	0.0030
1.6 - 1.7	1.4	0.070	4.1 - 4.2	0.04	0.0020
1.7 - 1.8	1.0	0.050	4.2 - 4.3	*	*
1.8 - 1.9	0.95	0.0475		*	*
1.9 - 2.0	0.85	0.0425		*	*
2.0 - 2.1	0.74	0.0370		*	*
2.1 - 2.2	0.66	0.0330		*	*
2.2 - 2.3	0.64	0.0320		*	*
2.3 - 2.4	0.56	0.0280		*	*
2.4 - 2.5	0.47	0.0235		*	*
2.5 - 2.6	0.38	0.0190		*	*
2.6 - 2.7	0.34	0.0170		*	*
2.7 - 2.8	0.30	0.0150	∞	*	*
2.8 - 2.9	0.28	0.0140			
2.9 - 3.0	0.26	0.0130	Note: * Too little to be counted		

Table 4. Parameters used in the stochastic averaging computation and the mean surface shear stress obtained.

Gaussian Distribution $P(U_c) = (\sigma\sqrt{2\pi})^{-1} \exp\left\{ \frac{-[U_c-(U_c)_{mp}]^2}{2\sigma^2} \right\}$

Modified Rayleigh Distribution $P(U_c) = \frac{U_c-(U_c)_{min}}{c^2} \exp\left\{ - \frac{[U_c-(U_c)_{min}]^2}{c^2} \right\}$

Case No.	Assumed U_c Distribution			$(\tau_w)_{mp}$ N/m^2	$(\bar{\tau}_w)_{measured}$ N/m^2	$(\bar{\tau}_w)_{calculated}$ N/m^2	Reference Figure
1	Gaussian $(U_c)_{mp}$	= 4.3 m/sec	σ = 0.5 m/sec	0.1	0.1243	0.1419	14a
2	Gaussian	= 4.3 m/sec	= 1.0 m/sec	0.1	0.1243	0.1541	14b
3	Guassian	= 4.3 m/sec	= 1.5 m/sec	0.1	0.1243	0.1530	14c
4	Guassian	= 5.1 m/sec	= 0.5 m/sec	0.153	0.1713	0.2266	14d
5	Guassian	= 5.1 m/sec	= 1.0 m/sec	0.153	0.1713	0.2149	14e
6	Guassian	= 5.1 m/sec	= 1.5 m/sec	0.153	0.1713	0.2209	14f
7	Rayleigh $(U_c)_{min}$	= 3.2 m/sec	e = 1.0 m/sec	0.1	0.1243	0.1576	14g
8	Rayleigh	= 3.0 m/sec	= 1.30 m/sec	0.1	0.1243	0.1711	14h
9	Rayleigh	= 2.5 m/sec	= 1.800 m/sec	0.1	0.1243	0.1740	14i
10	Rayleigh	= 4.3 m/sec	= 0.95 m/sec	0.153	0.1713	0.2425	14j
11	Rayleigh	= 4.0 m/sec	= 1.25 m/sec	0.153	0.1713	0.2459	14k
12	Rayleigh	= 3.0 m/sec	= 1.90 m/sec	0.153	0.1713	0.2236	14l

Table 5. Static pressure distribution along the centerline of the test model. x was measured from the entrance of the test section.

Freestream Velocity	U_∞ = 10.7 m/sec	U_∞ = 9.76 m/sec	U_∞ = 8.55 m/sec
x-distance (cm)	Δp (mmHg)	Δp (mmHg)	Δp (mmHg)
120.40	+0.011	+0.008	+0.006
130.65	-0.001	-0.0016	-0.002
135.72	+0.002	+0.001	+0.000
140.77	+0.000	-0.000	-0.001
145.85	+0.000	-0.000	-0.001
151.01	+0.002	+0.0006	-0.000
156.01	+0.003	+0.001	+0.000
161.09	+0.001	+0.000	-0.000
166.12	+0.002	+0.001	+0.000
171.20	+0.001	-0.001	-0.000
176.28	+0.002	+0.001	+0.000
181.36	+0.003	+0.002	+0.0009
186.44	+0.002	+0.001	+0.000
191.52	+0.002	+0.001	+0.000
196.60	-0.001	-0.002	-0.002
201.68	-0.003	-0.0026	-0.0024
206.76	-0.007	-0.006	-0.006
209.30	+0.003	+0.0015	+0.0005
211.82	-0.016	-0.014	-0.012
214.36	-0.025	-0.021	-0.018
216.90	-0.031	-0.026	-0.021
218.21	-0.041	-0.036	-0.028
219.44	-0.055	-0.046	-0.038
220.07	-0.064	-0.055	-0.044
220.71	-0.072	-0.060	-0.050
220.99	-0.077	-0.065	-0.052
221.34	-0.084	-0.070	-0.058
222.80	-0.082	-0.071	-0.056
223.415	-0.069	-0.059	-0.050
224.705	-0.065	-0.054	-0.045
227.245	-0.050	-0.043	-0.035
229.785	-0.037	-0.031	-0.026
232.325	-0.028	-0.024	-0.020
234.883	-0.020	-0.016	-0.014
237.405	-0.013	-0.011	-0.010
239.945	-0.003	-0.004	-0.003
242.485	+0.007	+0.006	+0.004
245.025	+0.024	+0.020	+0.015
247.565	+0.042	+0.035	+0.028
250.105	+0.058	+0.048	+0.039
252.66	+0.067	+0.055	+0.041
255.20	+0.076	+0.064	+0.050

Table 5. (continued)

Freestream Velocity	U_∞ = 10.7 m/sec	U_∞ = 9.76 m/sec	U_∞ = 8.55 m/sec
x-distance (cm)	Δp (mmHg)	Δp (mmHg)	Δp (mmHg)
257.74	+0.083	+0.069	+0.054
260.30	+0.093	+0.077	+0.061
265.43	+0.097	+0.081	+0.064
267.95	+0.100	+0.085	+0.066
270.46	+0.104	+0.087	+0.068
272.98	+0.107	+0.089	+0.071
275.52	+0.111	+0.091	+0.072
278.11	+0.112	+0.094	+0.074
280.67	+0.114	+0.096	+0.074
283.19	+0.116	+0.099	+0.077

Table 6. Boundary layer quantities.

U_∞ (m/sec)	δ (cm)	δ^* (cm)	θ (cm)	H	R_θ	c_f 10^{-3}	$\bar{\tau}_w$ (N/m^2)	U_τ (m/sec)
10.20	6.350	0.991	0.718	1.380	4050	3.225	0.1713	0.4147
9.36	6.477	0.932	0.690	1.350	3500	3.350	0.1439	0.3800
8.55	6.528	0.879	0.664	1.324	3080	3.450	0.1243	0.3532

Table 7. Measured mean velocity distribution over the flat plate.

a) U_∞ = 10.20 m/sec

y	y/δ	yU_τ/ν	U	U/U_∞	U/U_τ
cm			m/sec		
0.018	0.0030	4.00	1.73	0.170	4.17
0.023	0.0036	5.19	2.27	0.225	5.47
0.028	0.0044	6.31	2.48	0.243	5.98
0.031	0.0049	6.99	3.08	0.302	7.42
0.045	0.0071	10.14	3.59	0.352	8.65
0.058	0.0090	13.08	4.23	0.415	10.20
0.083	0.0131	18.71	4.65	0.451	11.21
0.100	0.0157	22.54	5.04	0.494	12.15
0.134	0.0211	30.21	5.25	0.515	12.66
0.160	0.0252	36.08	5.42	0.531	13.07
0.210	0.0331	47.35	5.76	0.565	13.89
0.262	0.0413	59.08	5.79	0.568	13.96
0.388	0.0611	87.49	6.28	0.616	15.14
0.516	0.0811	116.35	6.55	0.642	15.79
0.642	0.1011	144.77	6.79	0.666	16.37
0.770	0.1213	173.63	6.92	0.678	16.68
1.024	0.1613	230.90	7.10	0.696	17.12
1.278	0.2013	288.18	7.34	0.720	17.70
2.040	0.3213	460.00	8.10	0.794	19.53
2.548	0.4013	574.57	8.36	0.820	20.17
3.310	0.5213	746.40	8.65	0.848	20.86
3.818	0.6013	861.00	9.15	0.897	22.06
4.580	0.7213	1032.80	9.44	0.926	22.78
5.088	0.8013	1147.33	9.69	0.950	23.37
5.586	0.8800	1259.00	9.82	0.963	23.69
5.842	0.9200	1317.00	10.00	0.980	24.11
6.092	0.9594	1373.36	10.09	0.989	24.33
6.350	1.0000	1431.00	10.20	1.000	24.60

Table 7. (continued)

b) U_∞ = 9.36 m/sec

y	y/δ	yU_τ/ν	U	U/U_∞	U/U_τ
cm			m/sec		
0.022	0.0034	4.54	1.75	0.188	4.60
0.027	0.0042	5.57	2.00	0.215	5.28
0.033	0.0051	6.82	2.28	0.245	6.02
0.037	0.0057	7.64	2.91	0.312	7.66
0.047	0.0073	9.71	3.32	0.357	8.74
0.063	0.0097	13.02	3.66	0.393	9.63
0.073	0.0113	15.08	3.91	0.420	10.29
0.087	0.0134	17.97	4.10	0.440	10.80
0.111	0.0171	22.94	4.52	0.485	11.89
0.163	0.0252	36.68	4.95	0.531	13.03
0.213	0.0329	44.01	5.24	0.562	13.78
0.263	0.0406	54.34	5.43	0.580	14.28
0.391	0.0604	80.79	5.65	0.606	14.87
0.516	0.0797	106.62	5.79	0.622	15.25
0.642	0.0991	132.66	5.96	0.639	16.68
0.769	0.1187	158.90	6.20	0.665	16.31
1.023	0.1579	211.38	6.36	0.680	16.74
1.530	0.2362	316.15	6.89	0.740	18.14
2.041	0.3154	422.15	7.25	0.778	19.09
2.546	0.3931	526.08	7.51	0.803	19.77
3.053	0.4714	630.84	7.89	0.843	20.76
3.814	0.5889	788.10	8.38	0.896	22.06
4.575	0.7063	945.33	8.72	0.936	22.95
5.084	0.7849	1050.51	8.80	0.940	23.14
5.690	0.8785	1175.73	9.03	0.965	23.76
6.092	0.9450	1258.80	9.20	0.983	24.20
6.477	1.0000	1337.52	9.36	1.000	24.62

Table 7. (continued)

c) U_∞ = 8.55 m/sec

y	y/δ	yU_τ/ν	U	U/U_∞	U/U_τ
cm			m/sec		
0.020	0.0031	3.84	1.37	0.161	3.88
0.026	0.0040	4.99	1.88	0.220	5.32
0.032	0.0049	6.14	2.28	0.268	6.46
0.036	0.0055	6.91	2.50	0.294	7.09
0.046	0.0070	8.83	2.95	0.345	8.35
0.062	0.0095	11.91	3.58	0.420	10.15
0.081	0.0124	15.55	3.74	0.439	10.60
0.111	0.0170	21.32	4.30	0.504	12.17
0.163	0.0250	31.30	4.70	0.550	13.28
0.213	0.0326	40.91	4.89	0.573	13.84
0.263	0.0403	49.30	4.96	0.580	14.01
0.388	0.0594	74.52	5.17	0.605	14.62
0.516	0.0790	99.10	5.30	0.620	15.00
0.642	0.0983	123.30	5.51	0.645	15.60
0.769	0.1178	147.70	5.60	0.655	15.82
1.023	0.1567	196.47	5.75	0.674	16.30
1.278	0.1958	245.45	6.00	0.703	16.98
1.530	0.2344	293.90	6.33	0.740	17.88
2.043	0.3130	392.37	6.58	0.771	18.63
2.546	0.3900	489.00	6.84	0.800	19.33
3.310	0.5070	635.71	7.20	0.844	20.39
4.072	0.6238	782.06	7.61	0.890	21.50
4.575	0.7008	878.70	7.87	0.920	22.22
5.088	0.7794	977.20	8.04	0.940	22.71
5.334	0.8171	1024.44	8.08	0.945	22.83
6.096	0.9338	1170.79	8.38	0.980	23.68
6.528	1.0000	1253.00	8.55	1.000	24.16

Table 8. Turbulence intensity measurements.

a) U_∞ = 10.20 m/sec

y (cm)	y/δ	Turbulent Intensity (%)
0.008	0.001	29.0
0.020	0.003	28.2
0.038	0.006	25.3
0.051	0.008	23.2
0.076	0.012	20.5
0.127	0.020	16.7
0.190	0.030	14.3
0.254	0.040	13.4
0.381	0.060	11.2
0.508	0.080	10.3
1.016	0.160	9.0
1.524	0.240	8.0
2.032	0.320	7.6
2.540	0.400	6.2
3.302	0.520	5.1
4.318	0.680	3.7
5.080	0.800	3.0
5.842	0.920	2.0

a) U_∞ = 10.20 m/sec

y (cm)	y/δ	Turbulent Intensity (%)
0.008	0.001	27.7
0.020	0.003	29.0
0.038	0.006	24.6
0.051	0.009	20.8
0.076	0.011	20.1
0.127	0.019	17.3
0.190	0.029	14.8
0.254	0.039	13.3
0.381	0.058	11.8
0.508	0.078	10.7
1.016	0.157	9.0
1.524	0.235	7.9
2.032	0.313	7.3
2.540	0.392	6.2
3.302	0.509	5.0
4.318	0.666	3.9
5.080	0.784	3.0
5.715	0.882	1.7

Table 8. (continued)

c) U_∞ = 8.55 m/sec

y (cm)	y/δ	Turbulent Intensity (%)
0.008	0.001	27.3
0.020	0.003	32.0
0.038	0.005	24.6
0.051	0.007	20.4
0.076	0.011	20.3
0.127	0.019	17.1
0.190	0.029	15.2
0.254	0.039	13.7
0.381	0.058	11.6
0.508	0.077	11.1
1.016	0.155	9.1
1.524	0.233	8.2
2.032	0.311	7.3
2.540	0.389	6.5
3.302	0.505	5.1
4.318	0.661	4.3
5.082	0.778	2.4
5.715	0.875	1.6

Table 9. Intermittency measurements.

U_∞ = 10.20 m/sec		U_∞ = 9.36 m/sec		U_∞ = 8.55 m/sec	
y/δ	γ	y/δ	γ	y/δ	γ
0.400	0.97	0.387	0.98	0.395	0.98
0.500	0.96	0.492	-	0.494	0.92
0.600	0.95	0.589	0.93	0.585	0.87
0.700	0.93	0.686	0.92	0.684	0.83
0.800	0.77	0.782	0.51	0.782	0.77
0.900	0.18	0.879	0.23	0.881	-
1.003	0.03	0.976	0.14	0.980	0.08

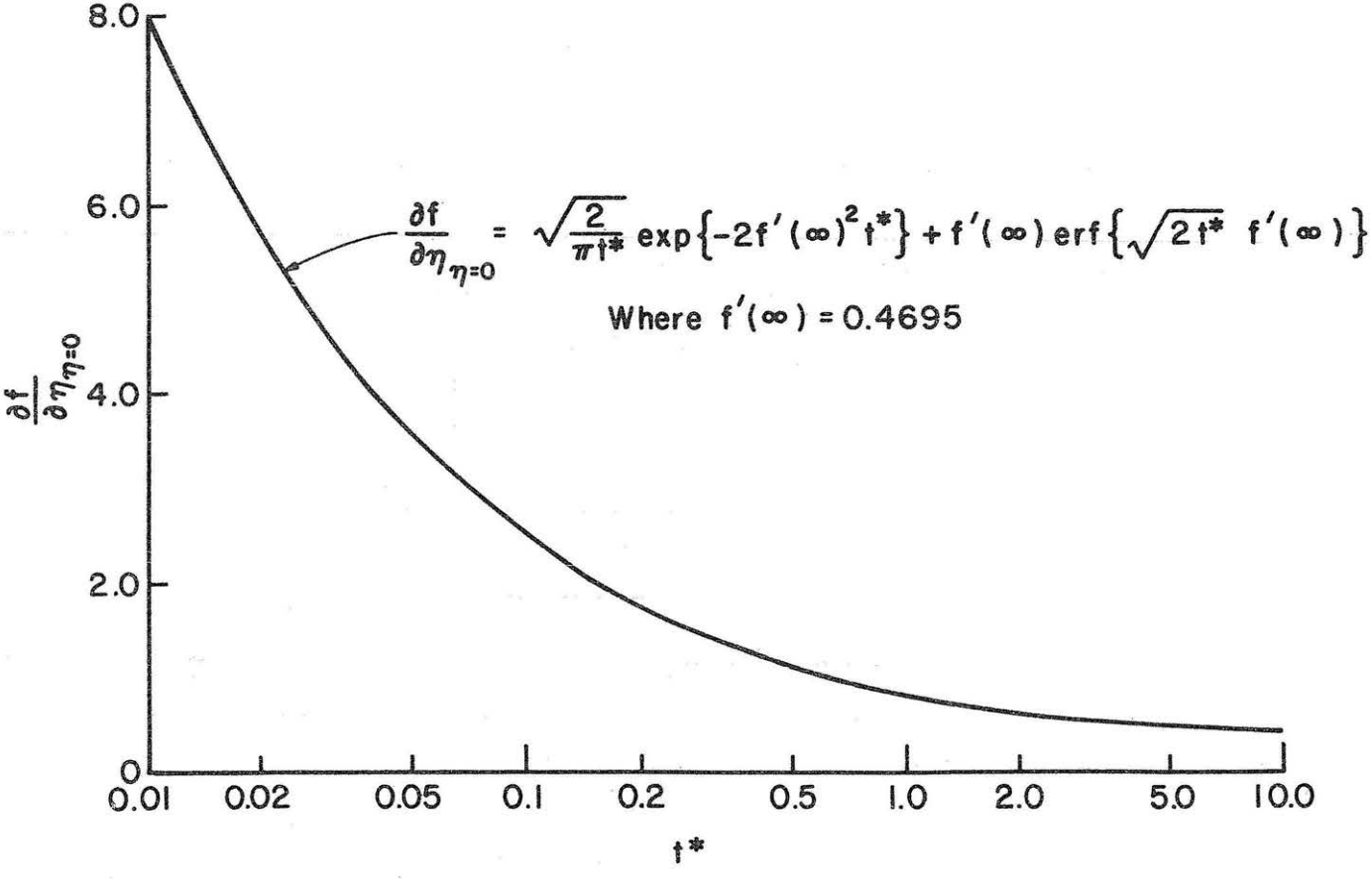

Figure 12. The surface shear stress variation due to a single sweep motion, Equation (32).

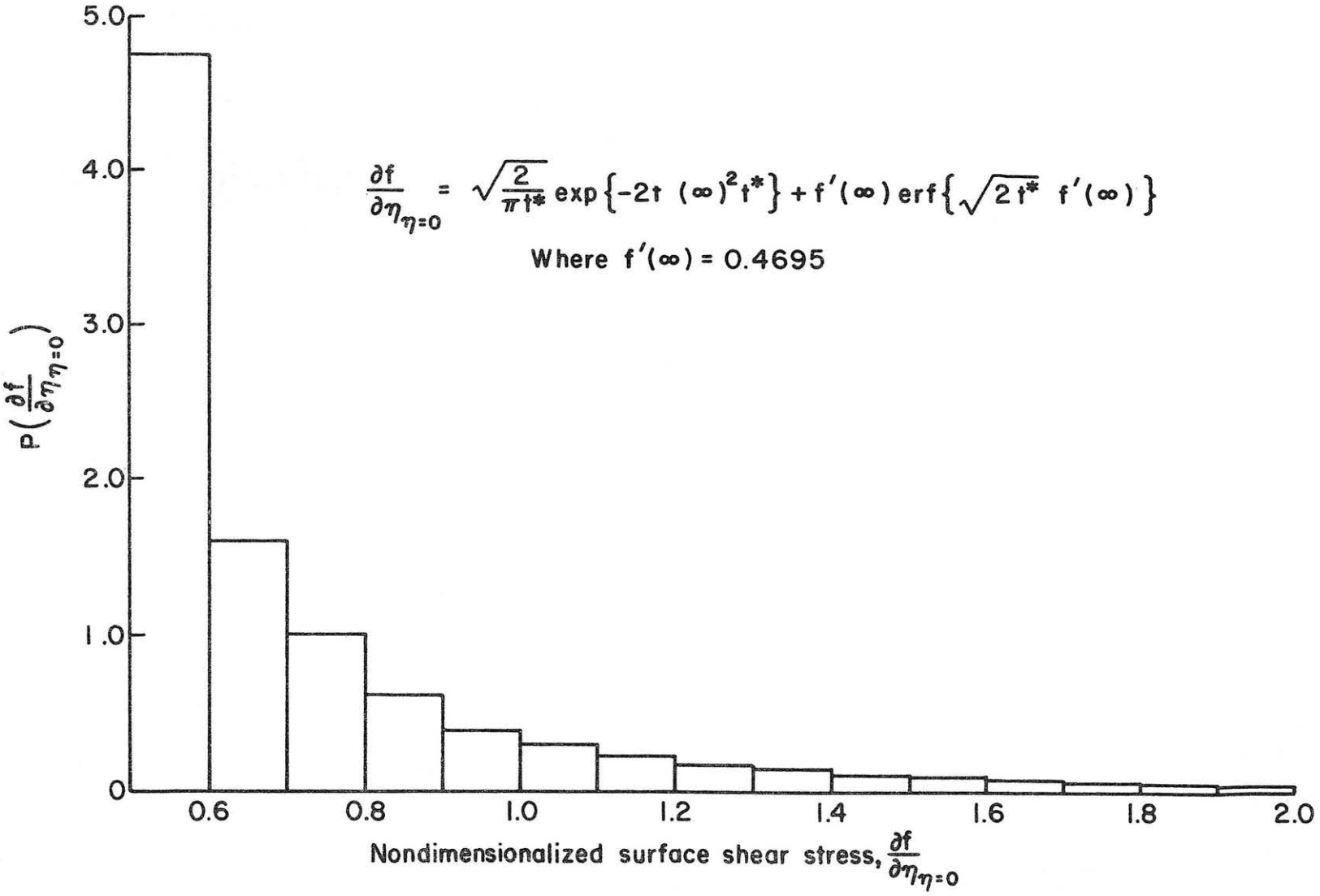

Figure 13. Estimated probability density function of $\partial f/\partial \eta\ \eta=0$. Values of $\partial f/\partial \eta\ \eta=0$ between $t^* = 0$ and $t^* = 4.0$ were used.

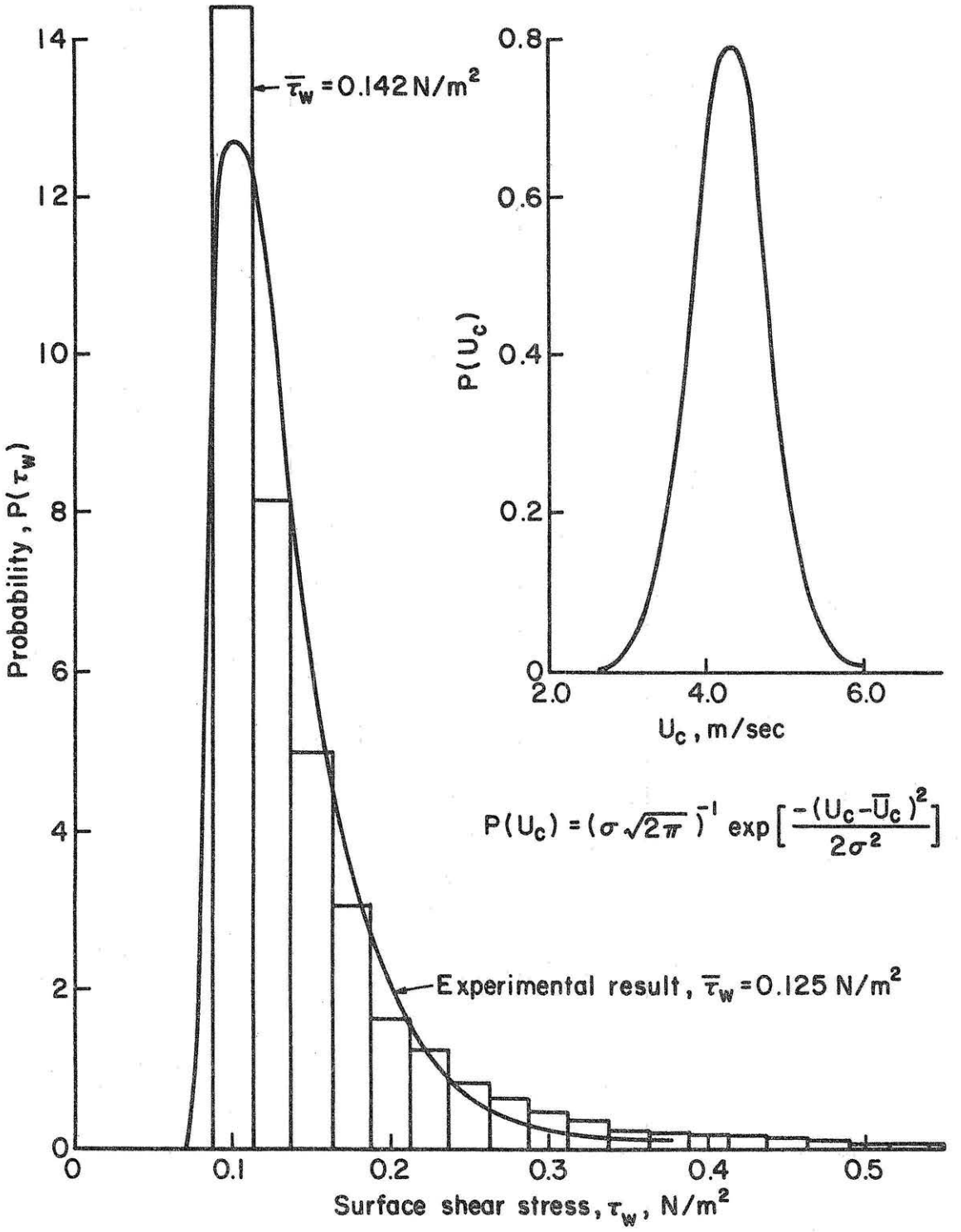

Figure 14a. Predicted probability distribution; Gaussian distribution $\bar{U}c$=4.3 m/sec, σ=0.5 m/sec.

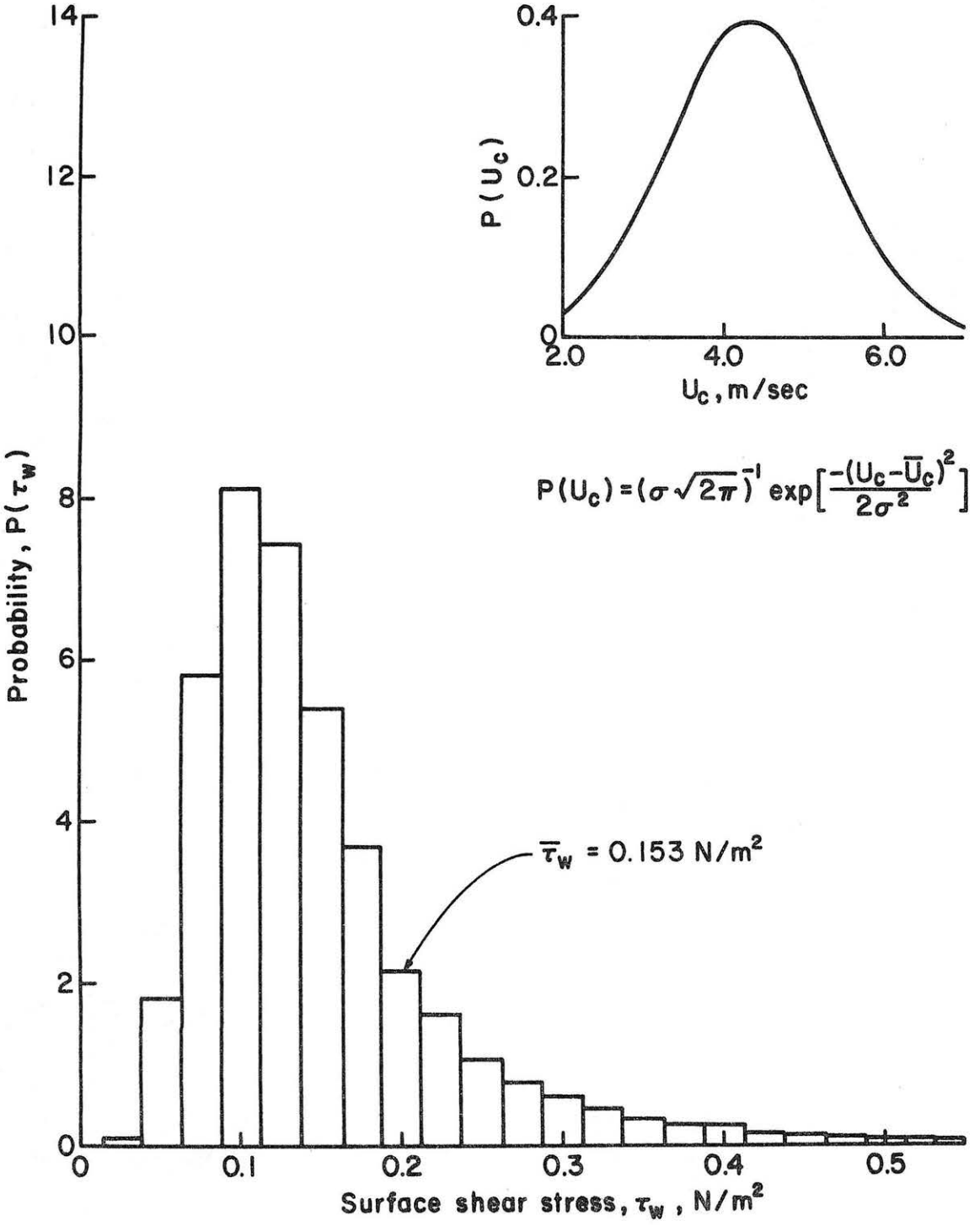

Figure 14b. Predicted probability distribution; Gaussian distribution $\bar{U}c$=4.3 m/sec, σ=1.0 m/sec.

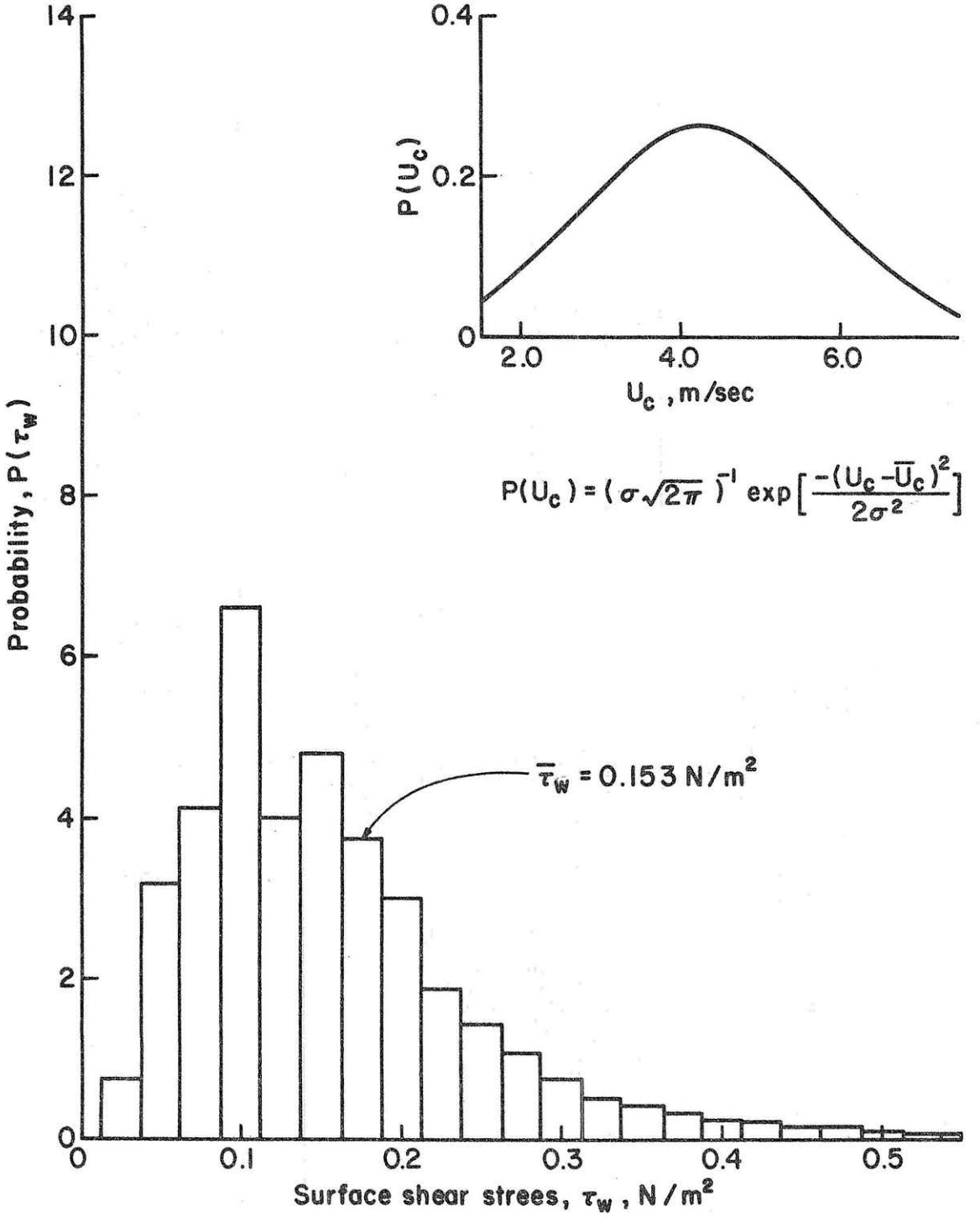

Figure 14c. Predicted probability distribution; Gaussian distribution $\bar{U}c$=4.3 m/sec, σ=1.5 m/sec.

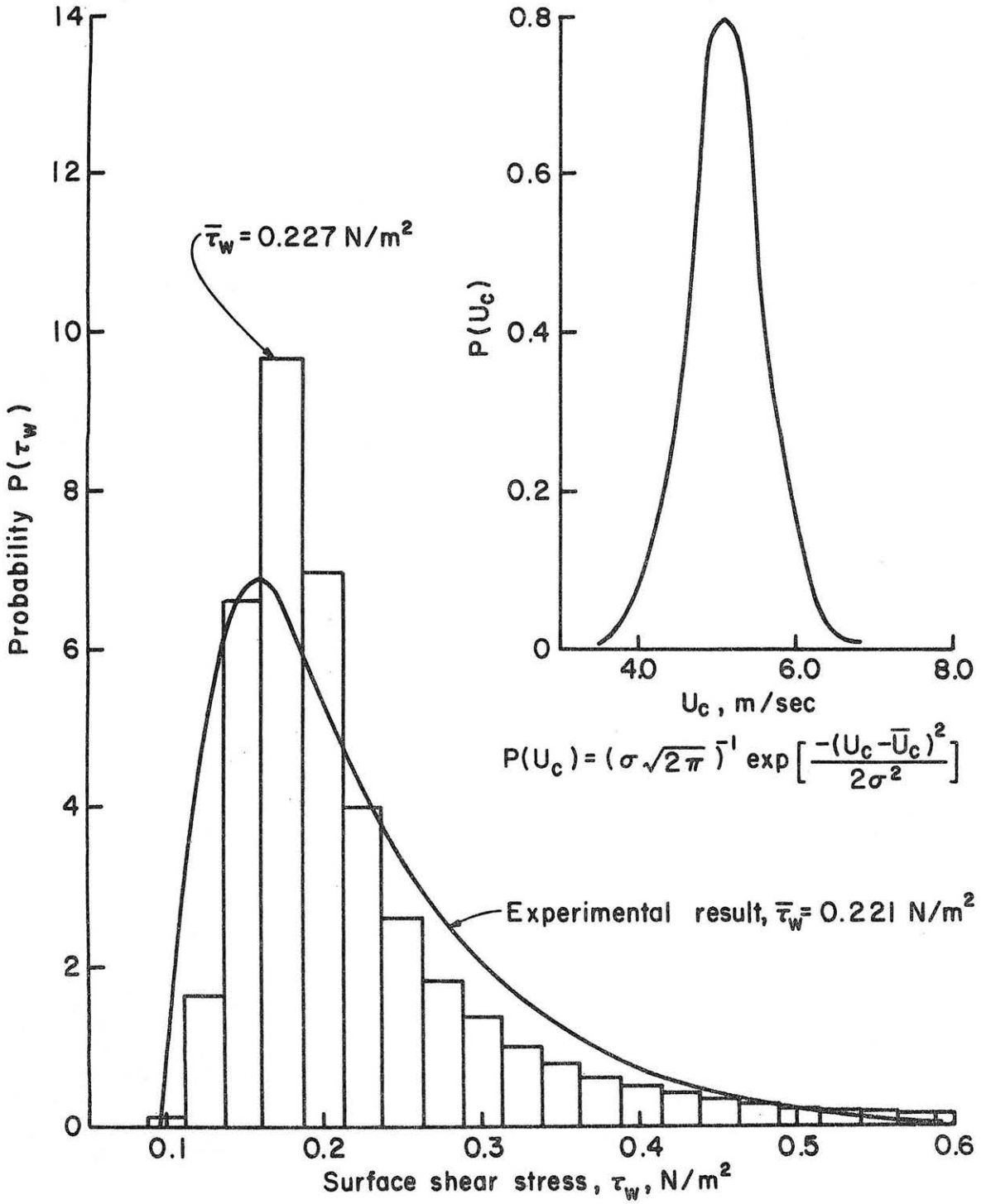

Figure 14d. Predicted probability distribution; Gaussian distribution $\bar{U}c$=5.1 m/sec, σ=0.5 m/sec.

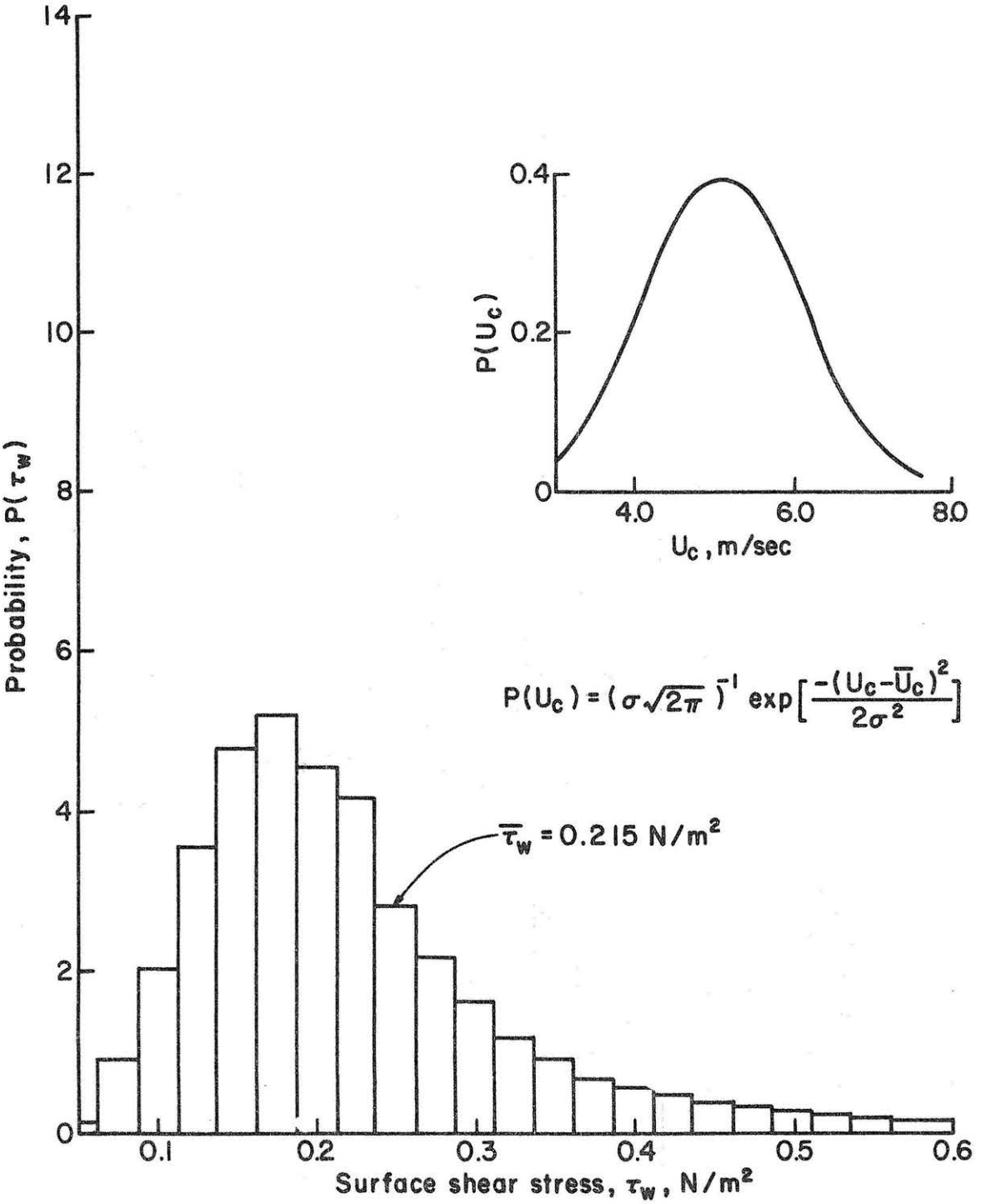

Figure 14e. Predicted probability distribution; Gaussian distribution $\bar{U}c$=5.1 m/sec, σ=1.0 m/sec.

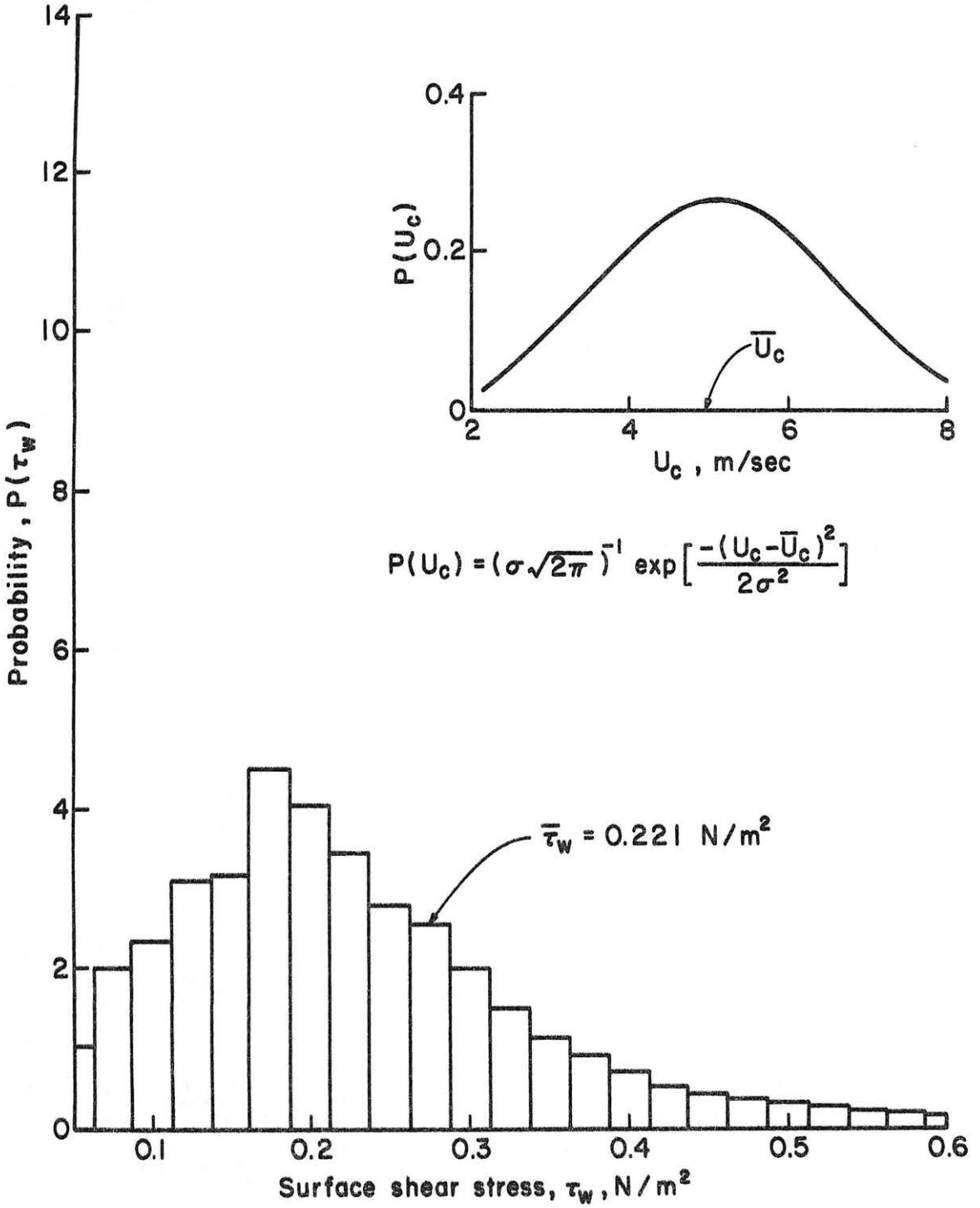

Figure 14f. Predicted probability distribution; Gaussian distribution $\bar{U}c$=5.1 m/sec, σ=1.5 m/sec.

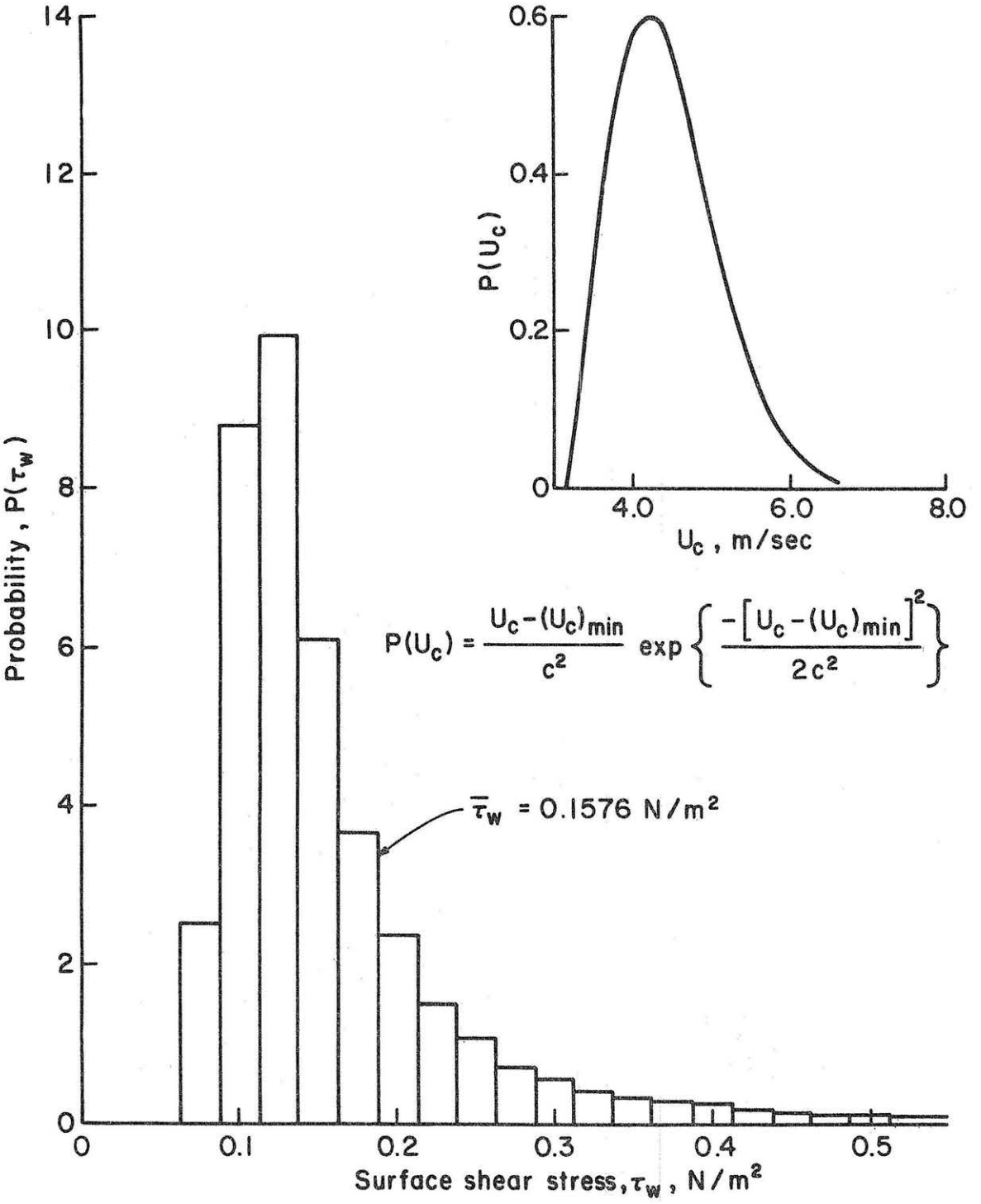

Figure 14g. Predicted probability distribution; Rayleigh distribution (Uc)min = 3.2 m/sec, c = 1.0 m/sec.

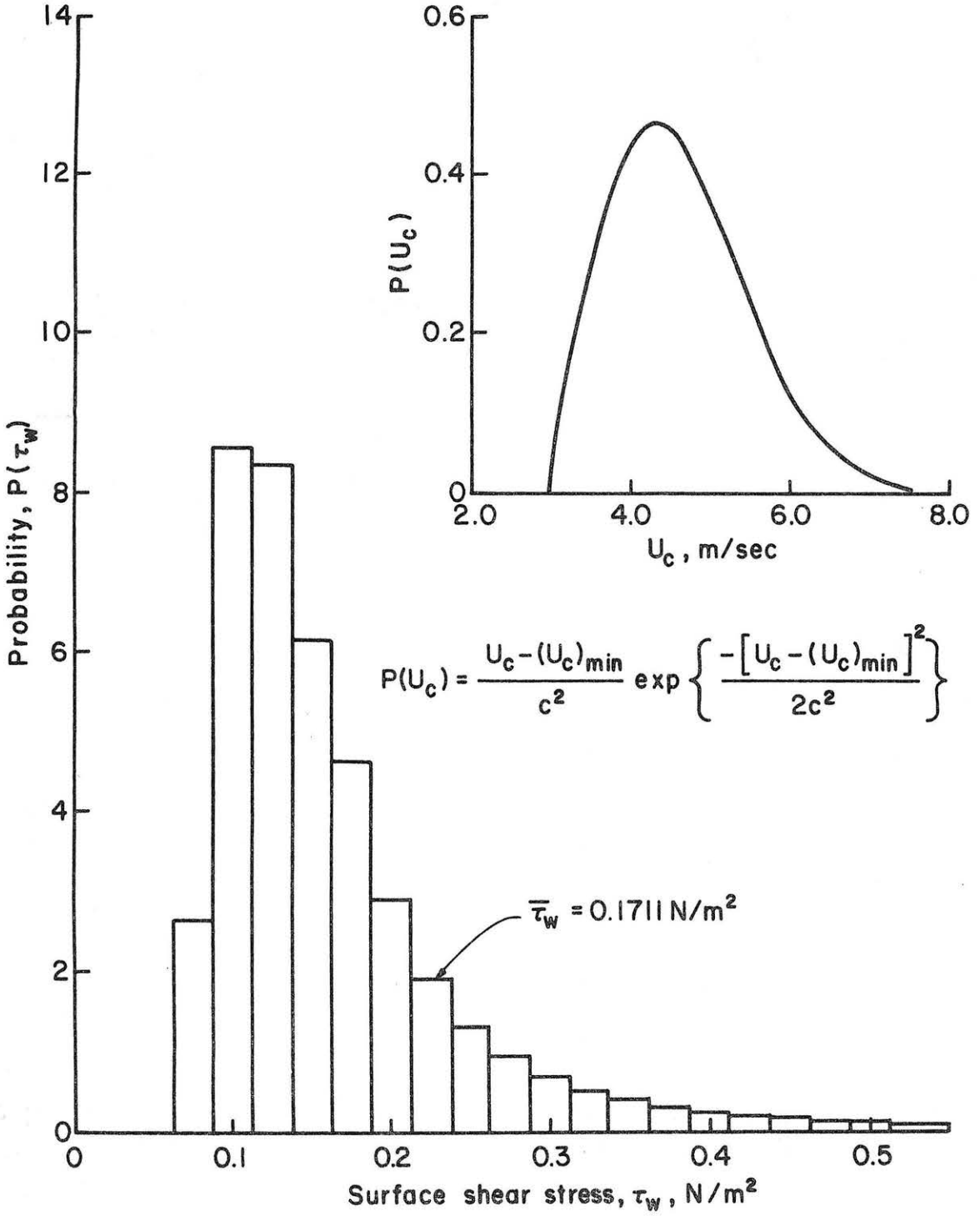

Figure 14h. Predicted probability distribution; Rayleigh distribution (Uc)min = 3.0 m/sec, c = 1.3 m/sec.

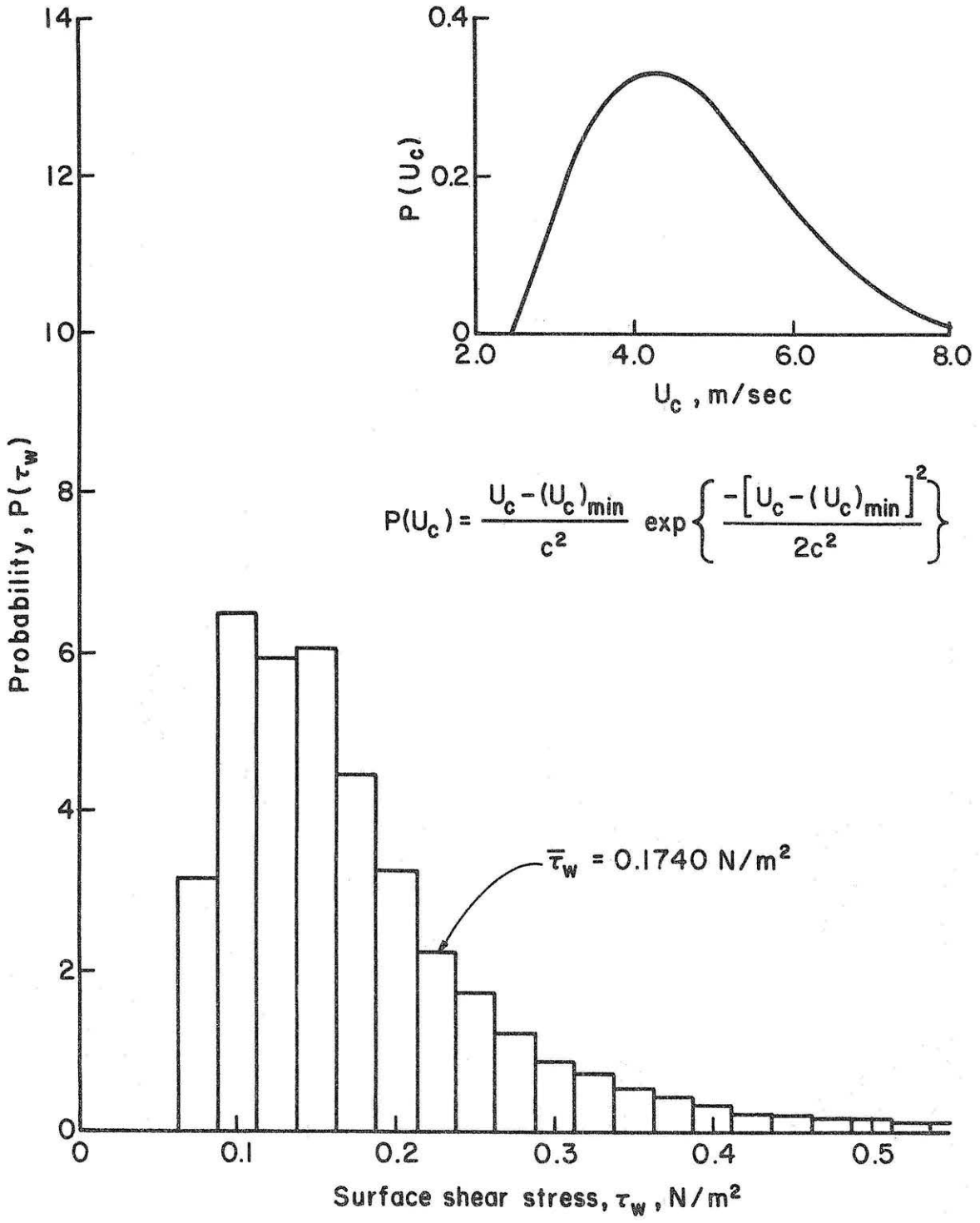

Figure 14i. Predicted probability distribution; Rayleigh distribution (Uc)min = 2.5 m/sec, c = 1.8 m/sec.

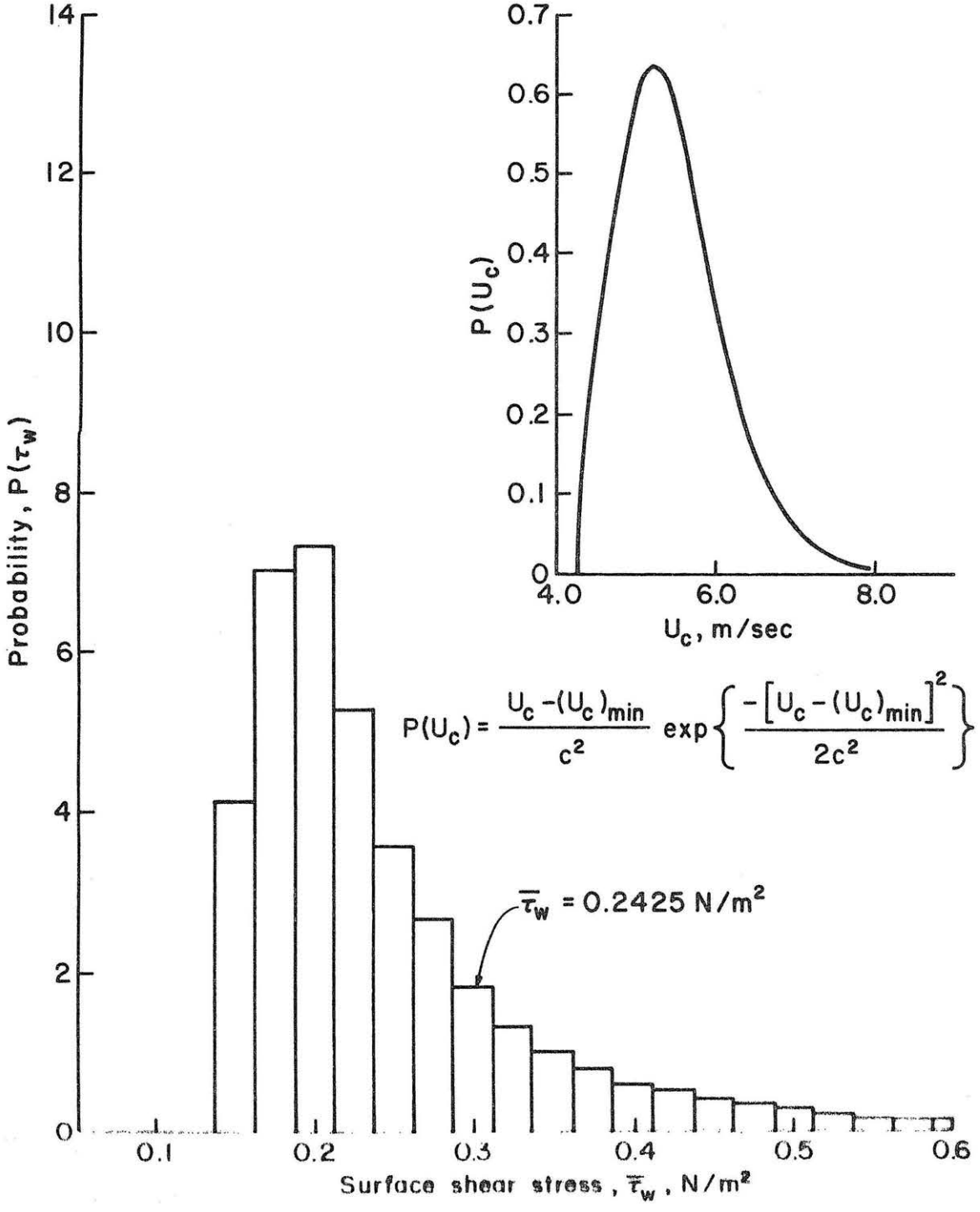

Figure 14j. Predicted probability distribution; Rayleigh distribution (Uc)min = 4.3 m/sec, c = 0.95 m/sec.

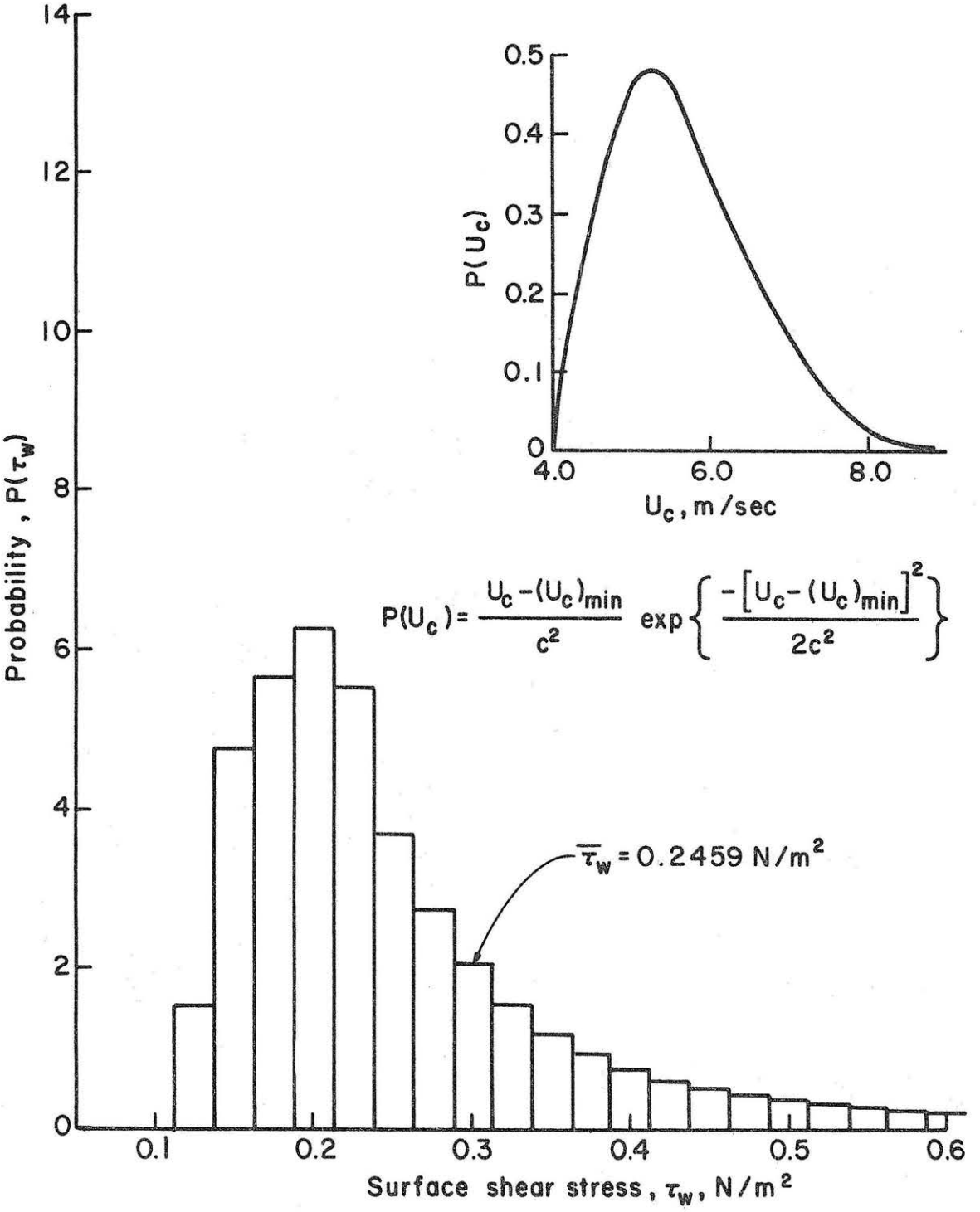

Figure 14k. Predicted probability distribution; Rayleigh distribution (Uc)min = 4.0 m/sec, c = 1.25 m/sec.

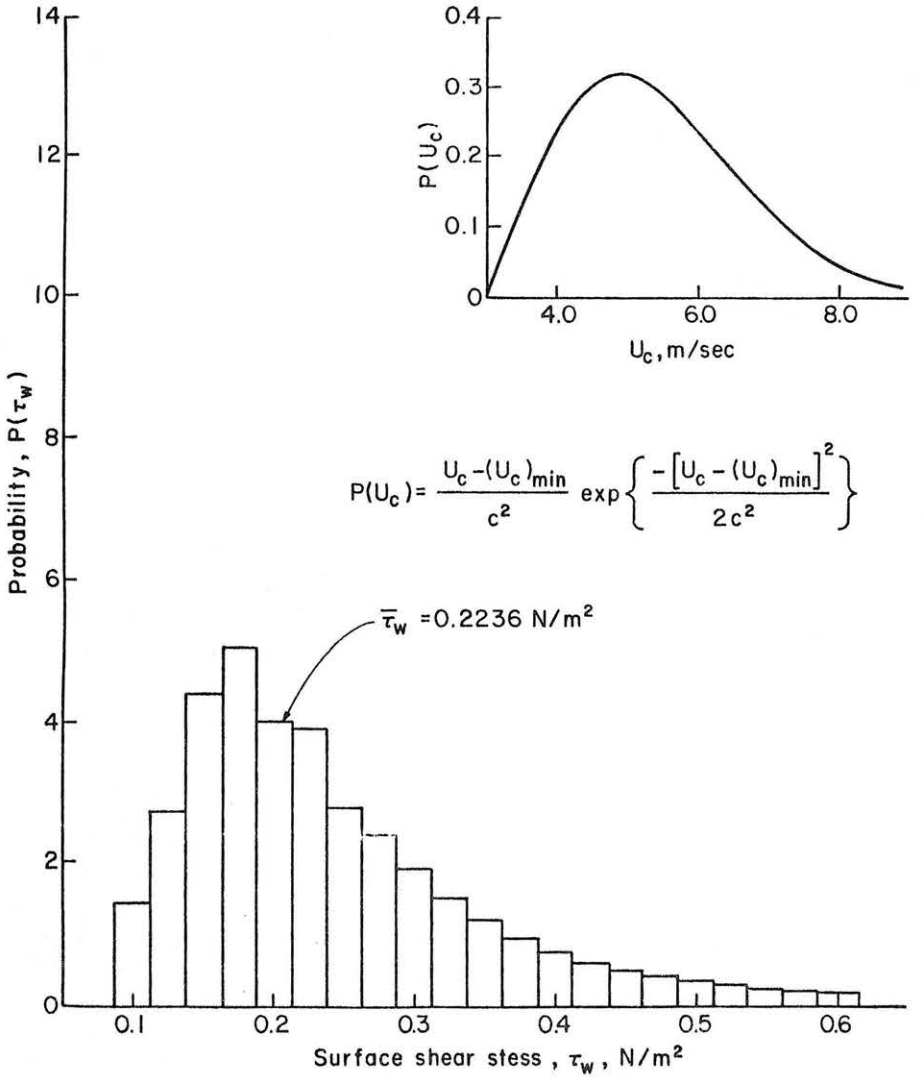

Figure 141. Predicted probability distribution; Rayleigh distribution (Uc)min = 3.0 m/sec, c = 1.9 m/sec.

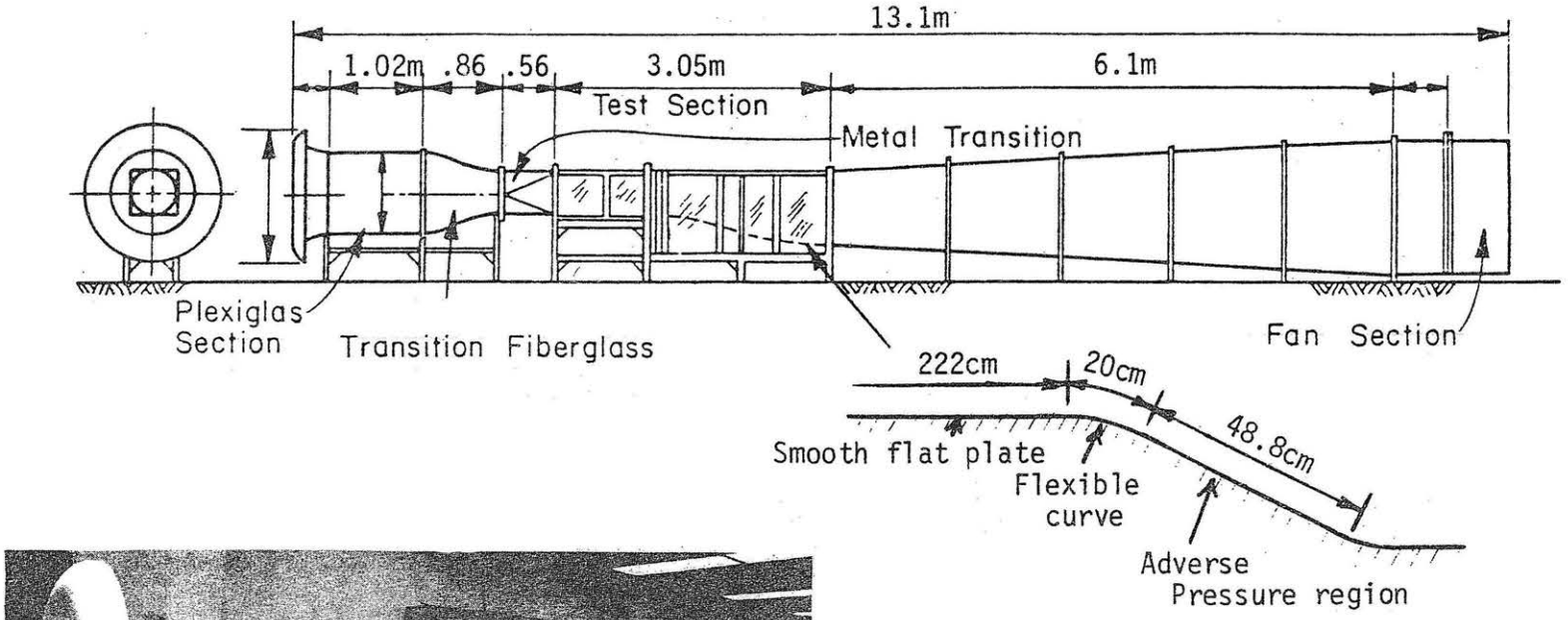

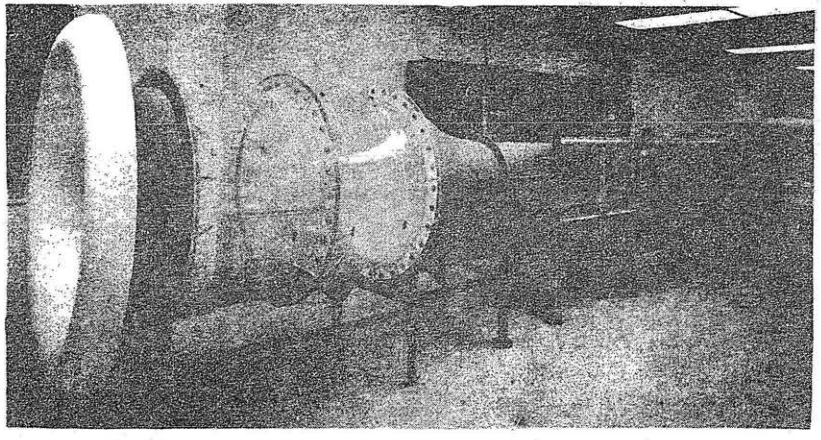

Figure 15. Wind tunnel facilities and steup of the test section.

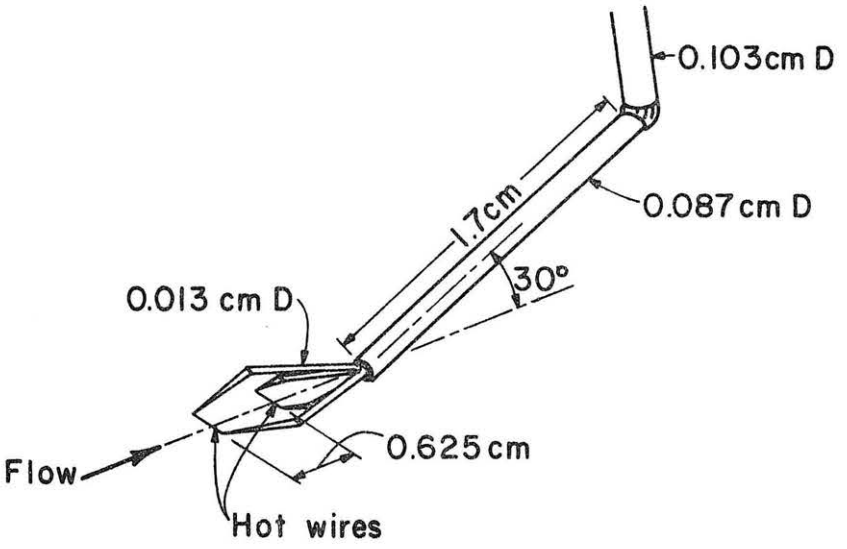

a) Dual wire probe.

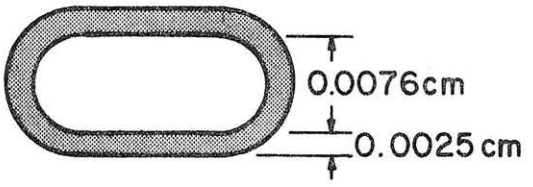

b) Small size pitot tube.

Figure 16. Probe dimensions.

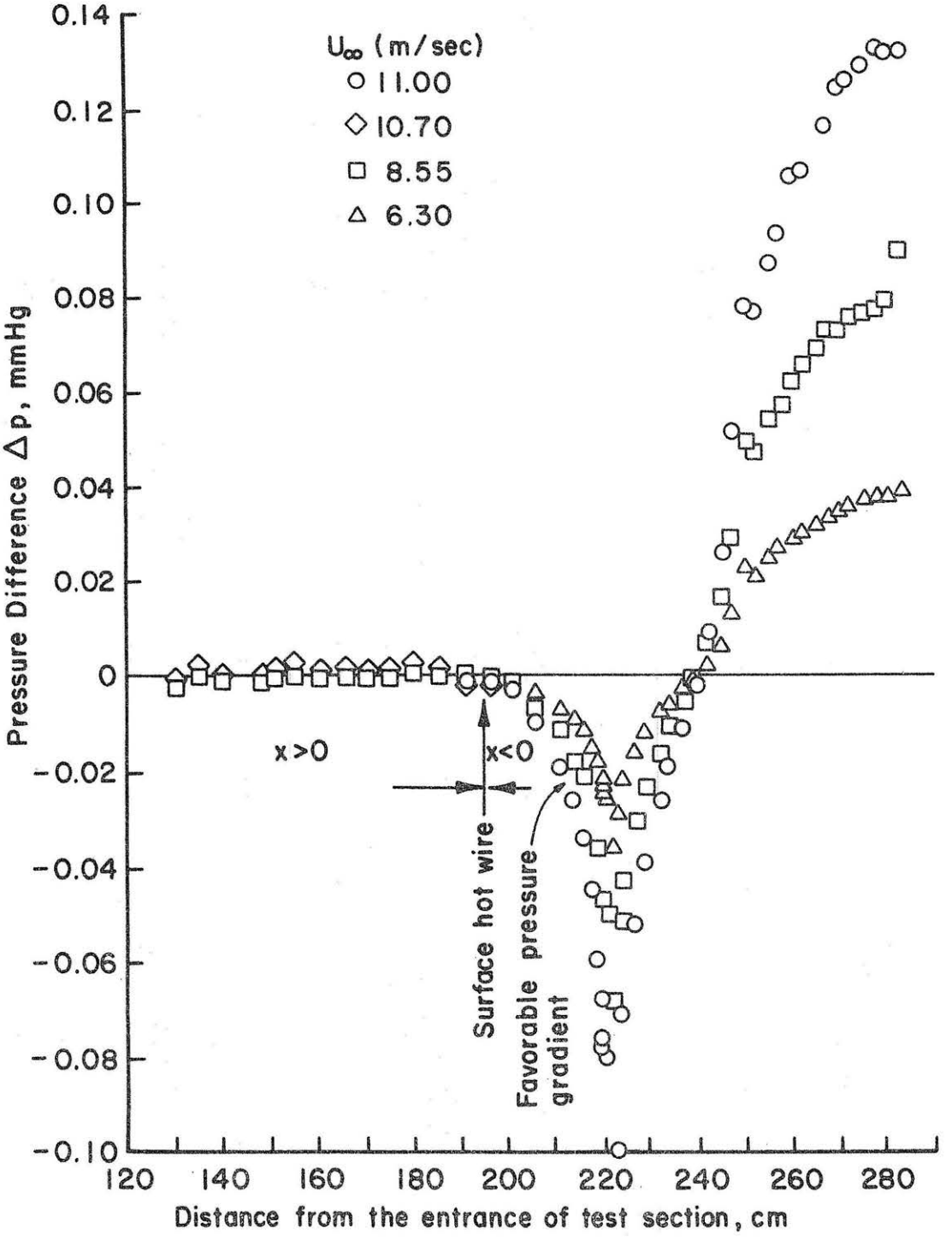

Figure 17. Static pressure distribution along the model surface.

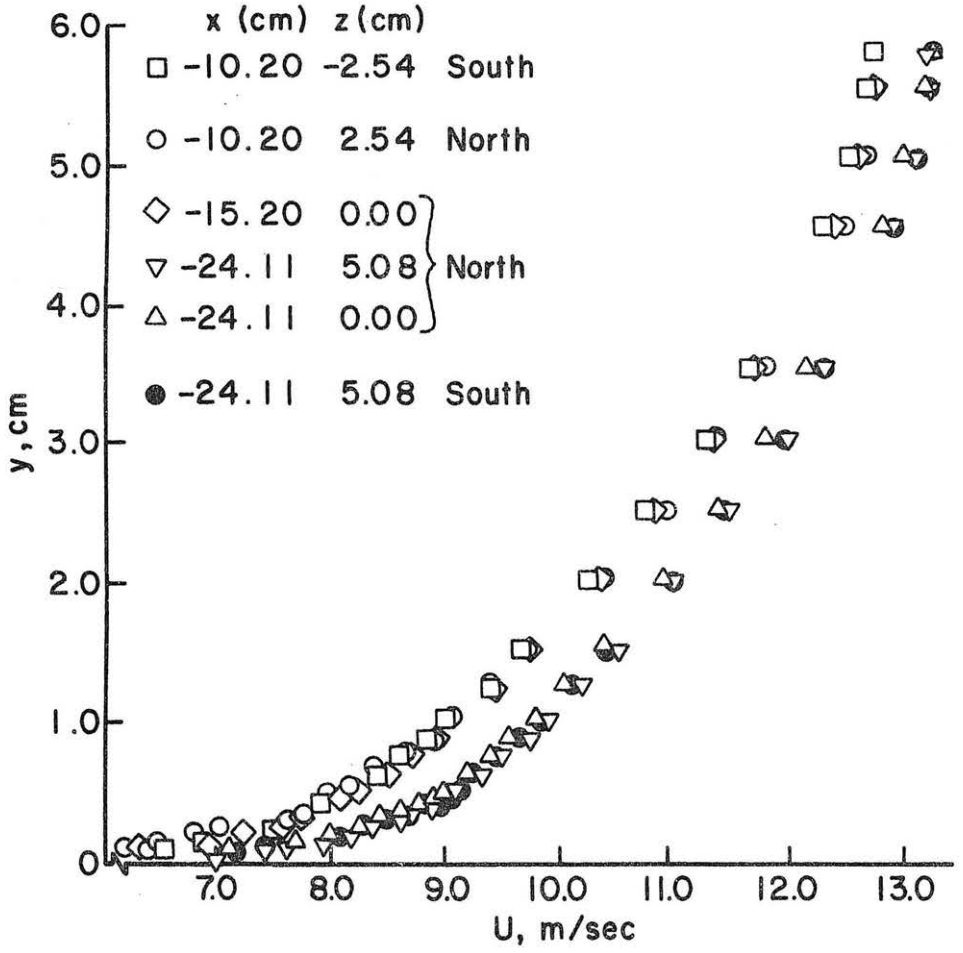

Figure 18. Mean velocity profiles measured for several lateral locations along the test model. U_∞ = 12.80 m/sec was measured at x = 0.0 cm.

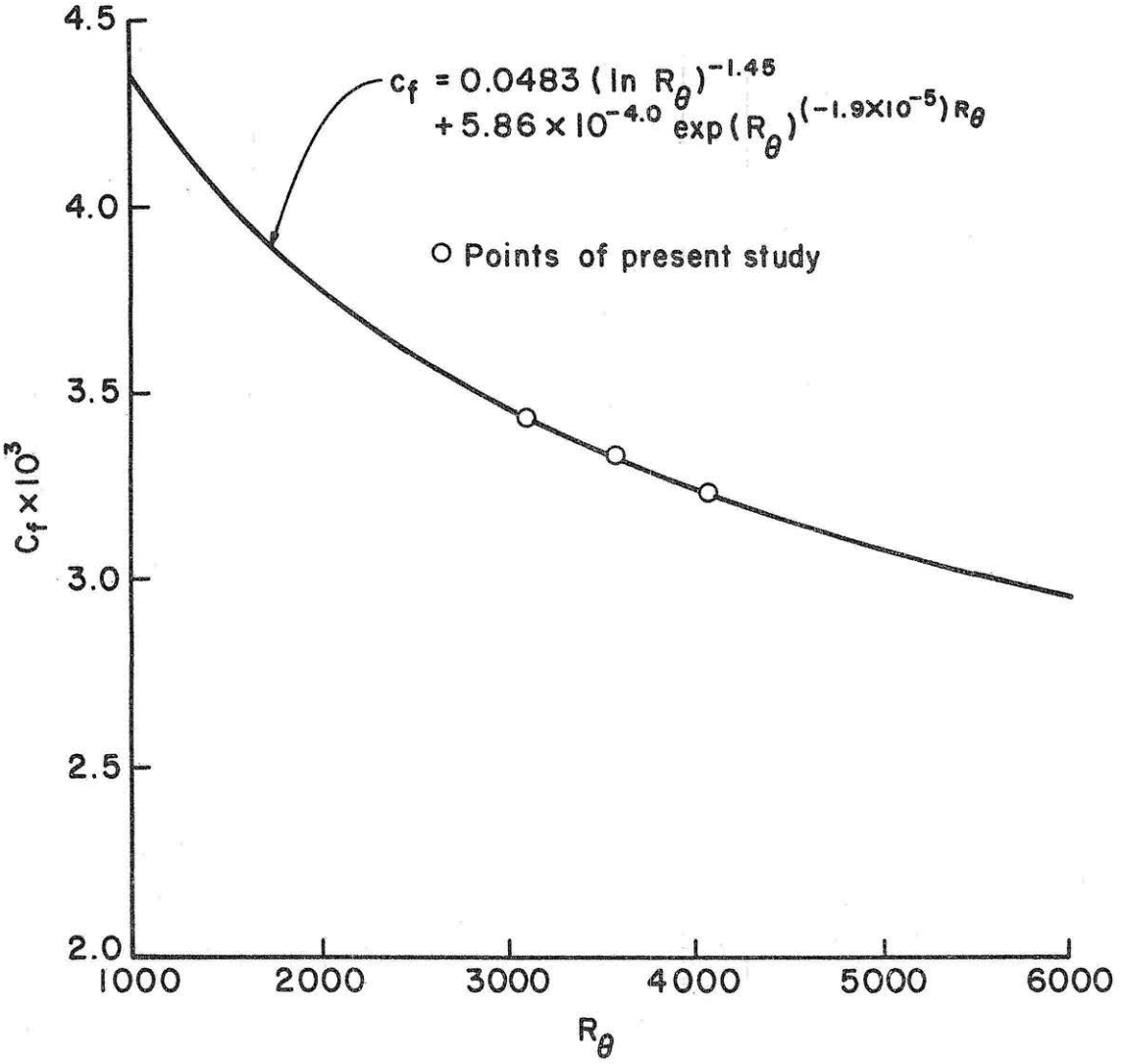

Figure 19. One parameter equation of Bell (1979) for the skin friction evaluation over a zero pressure gradient flat plate.

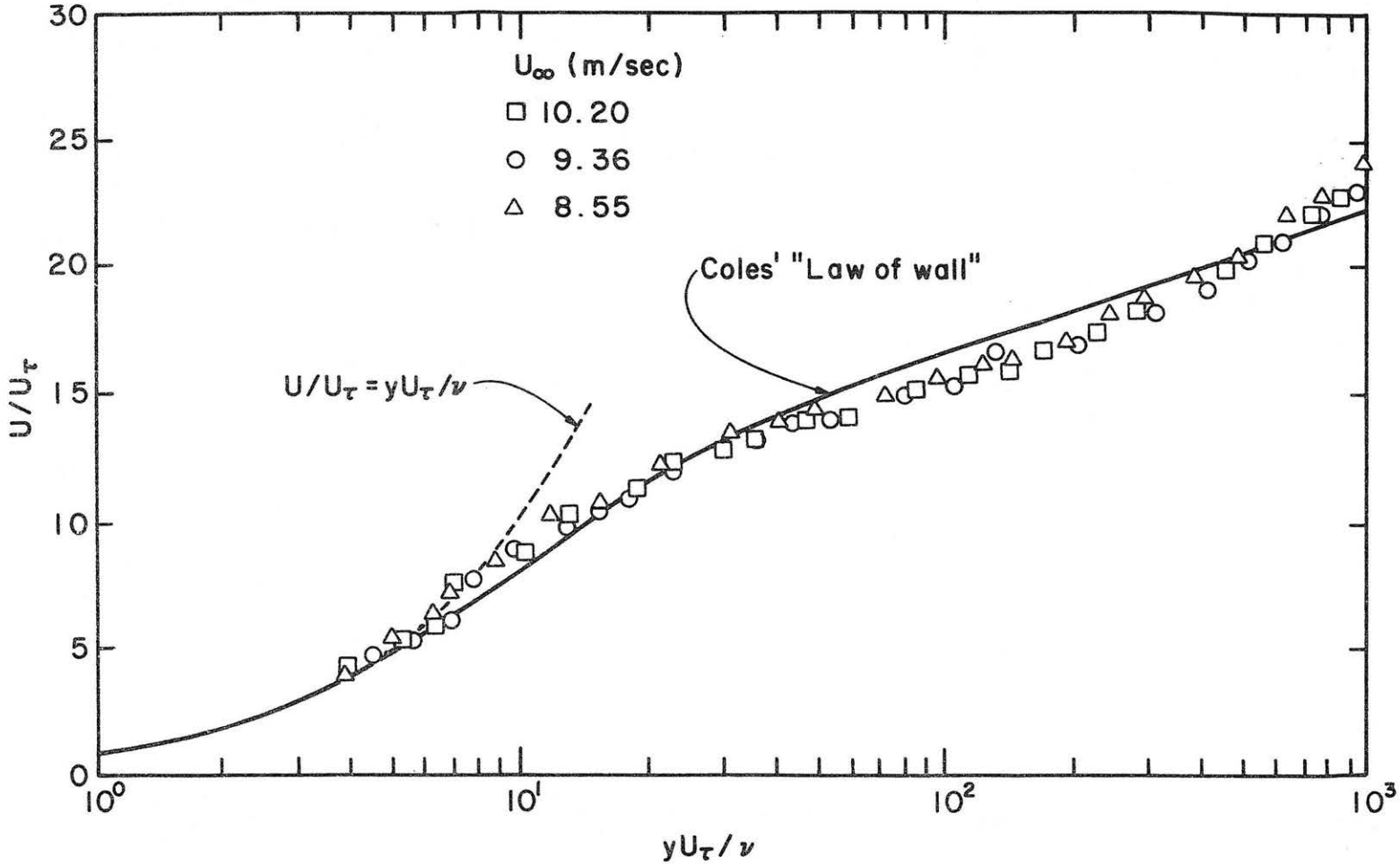

Figure 20. Similarity plots of mean velocity at x = 0.0 cm, z = 0.0 cm.

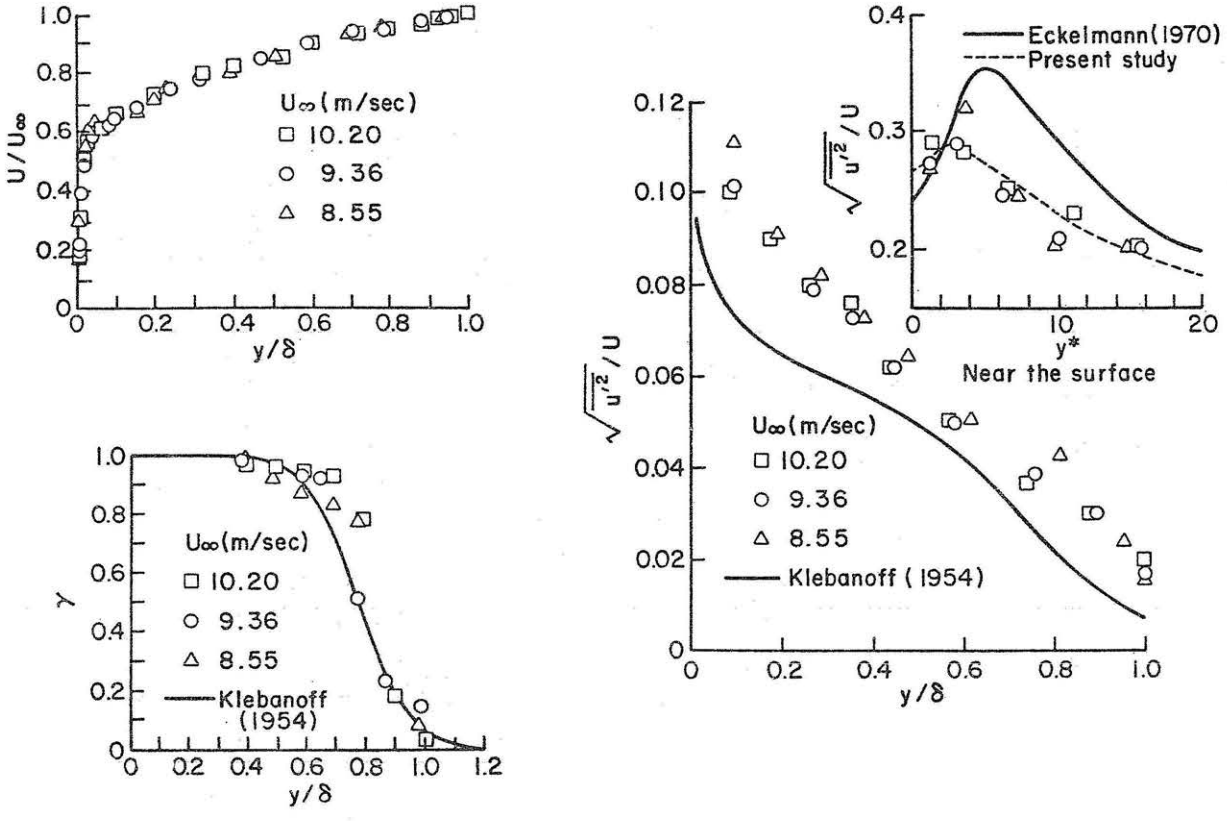

Figure 21. Boundary layer mean flow measurements.
a) Mean velocity profiles measured at x = 0.0 cm, z = 0.0 cm.
b) Turbulent intensity profiles measured at x = 0.0 cm, z = 0.0 cm compared with results of Klebanoff (1954) and Eckelmann (1970).
c) Intermittency profiles measured at x = 0.0 cm, z = 0.0 cm.

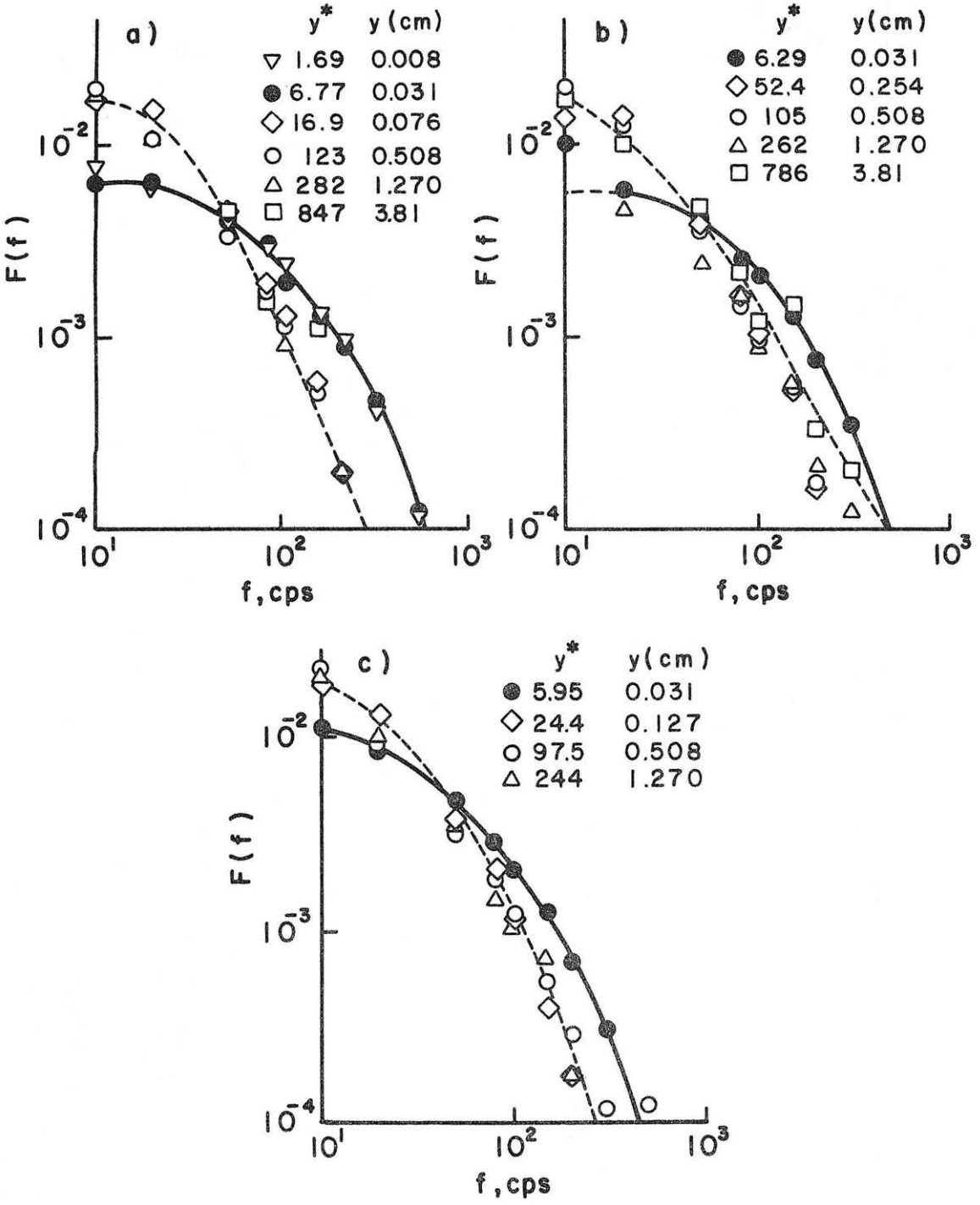

Figure 22. Energy spectrum at several heights across the boundary layer. Measured loction is x = 0.0 cm, z = 0.0 cm.
a) U_∞ = 10.20 m/sec.
b) U_∞ = 9.36 m/sec.
c) U_∞ = 8.55 m/sec.

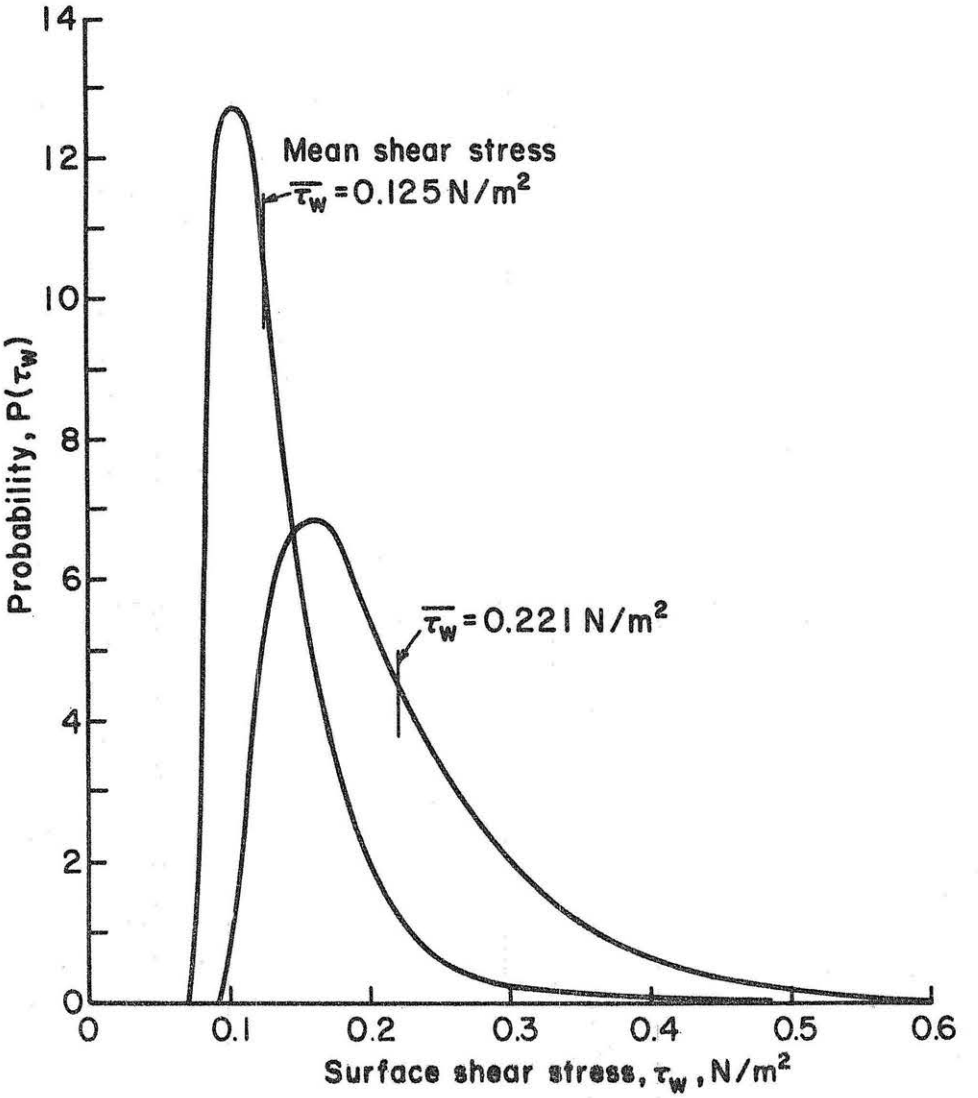

Figure 23. Probability density distribution of surface shear stress $P(\tau_w)$ measured at U_∞ = 8.55 m/sec ($\bar{\tau}_w$ = 0.125 N/m²) and U_∞ = 11.8 m/sec ($\bar{\tau}_w$ = 0.221 N/m²).

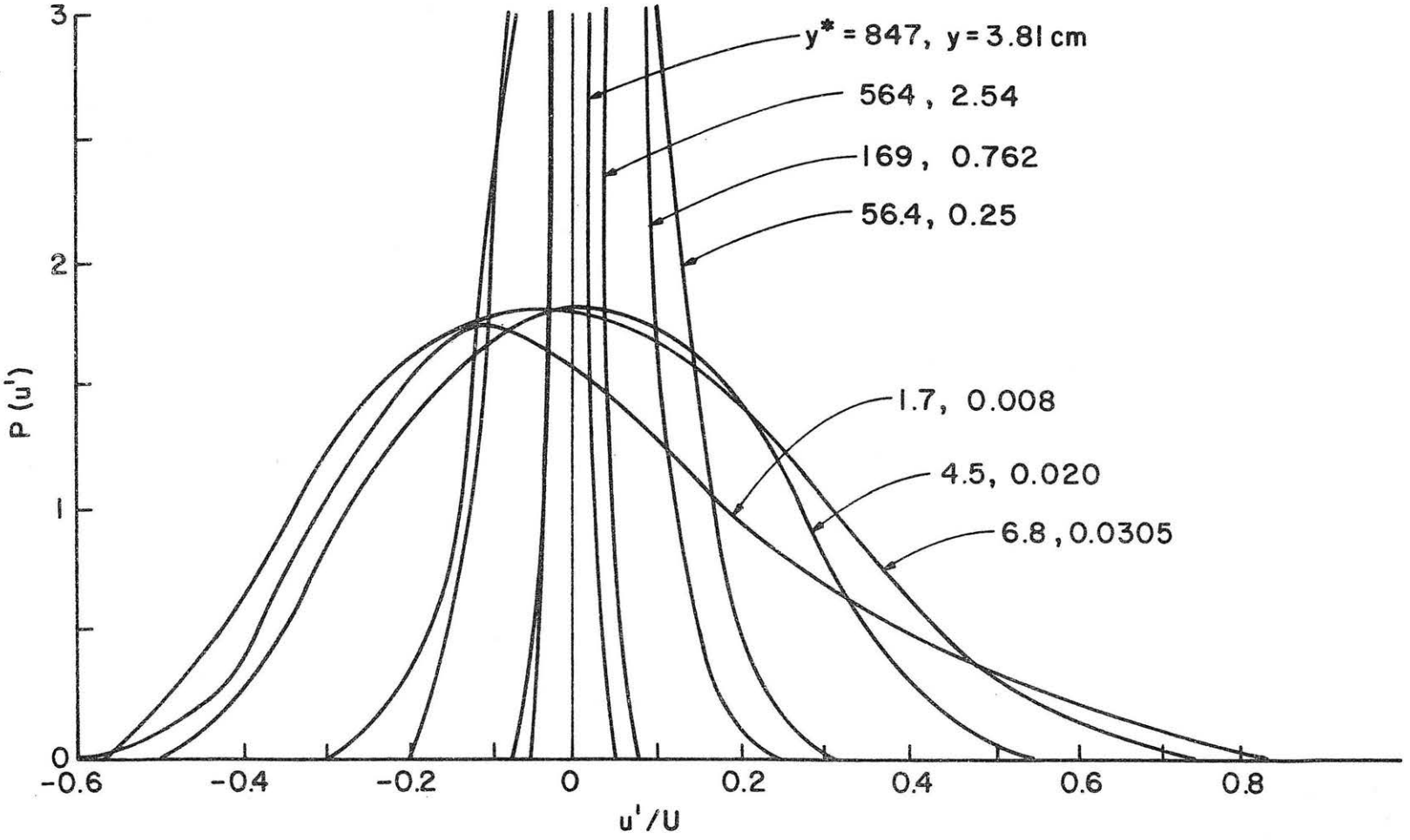

Figure 24a. Probability density function of the longitudinal turbulent velocity P(u); U_∞ = 10.20 m/sec, R_θ = 4050.

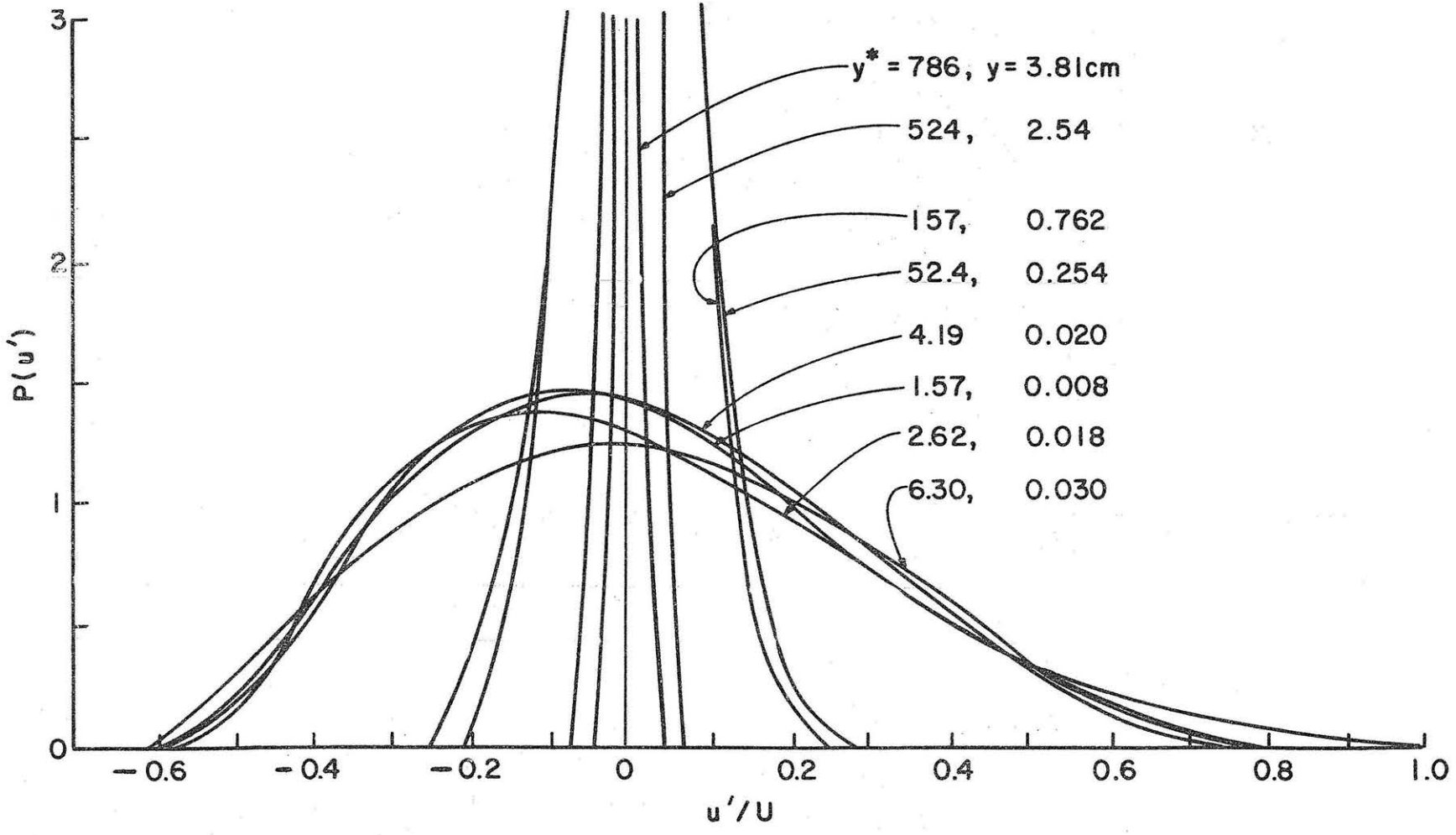

Figure 24b. Probability density function of the longitudinal turbulent velocity P(u); U_∞ = 9.36 m/sec, R_θ = 3500.

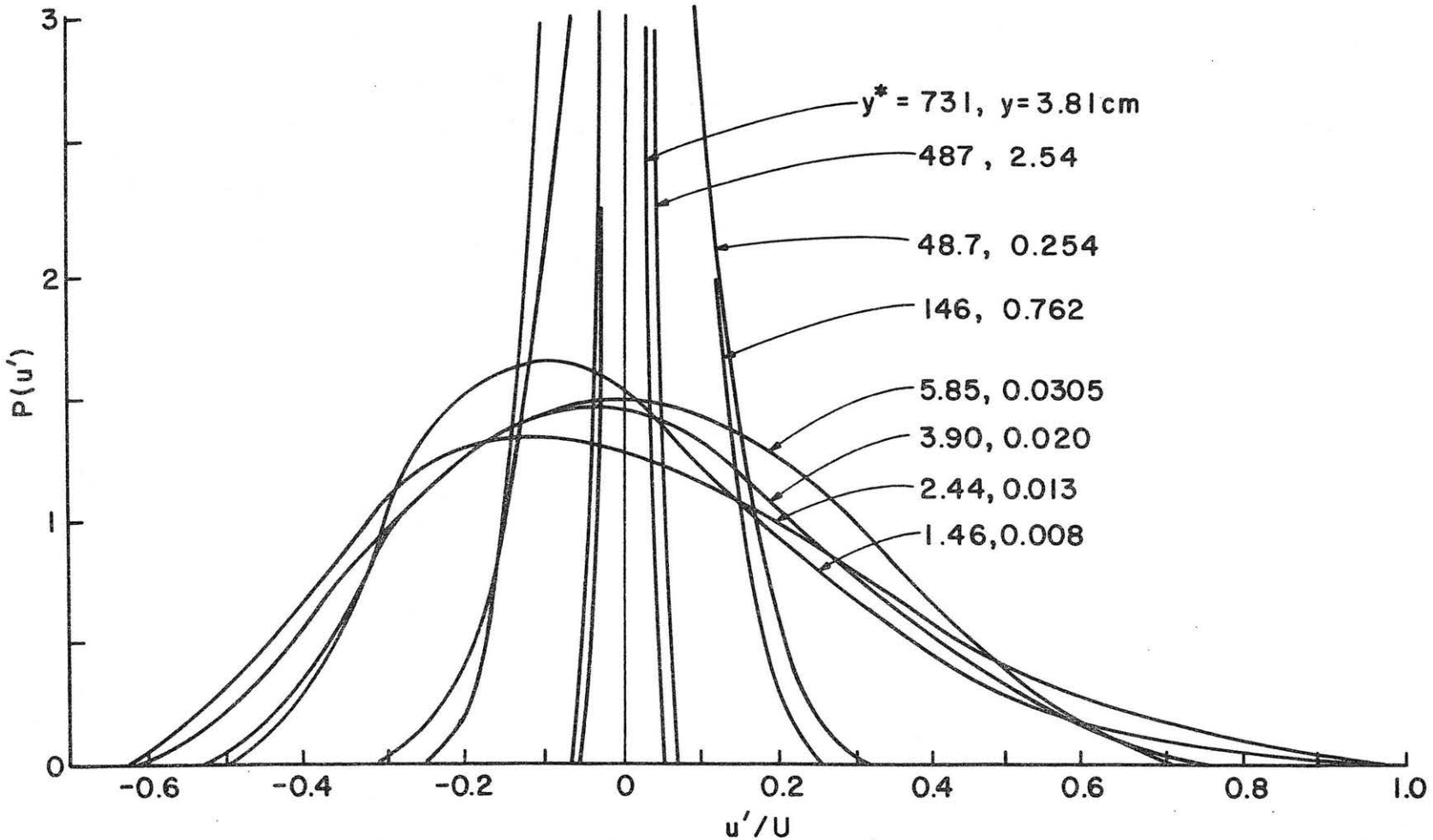

Figure 24c. Probability density function of the longitudinal turbulent velocity P(u); U_∞ = 8.55 m/sec, R_θ = 3080.

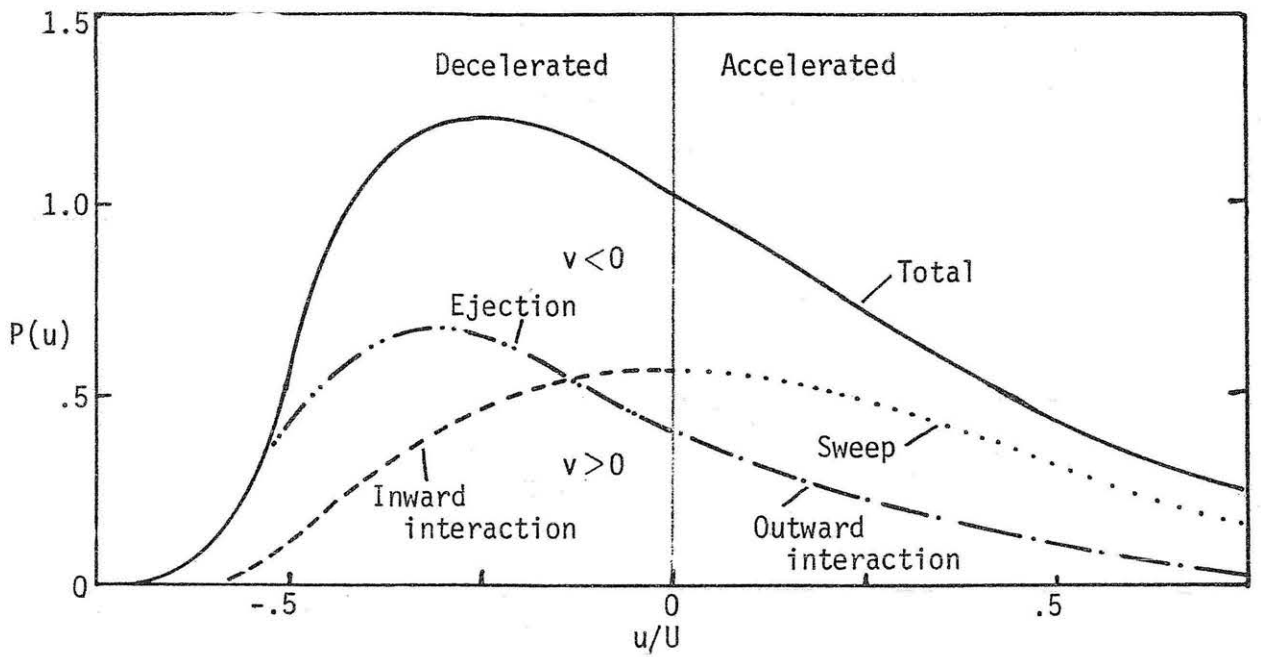

Figure 25. Probability density distribution of the longitudinal turbulent velocity and the contribution of individual motions involved in the bursting cycle at y* = 3.4, reported by Brodkey et al. (1974).

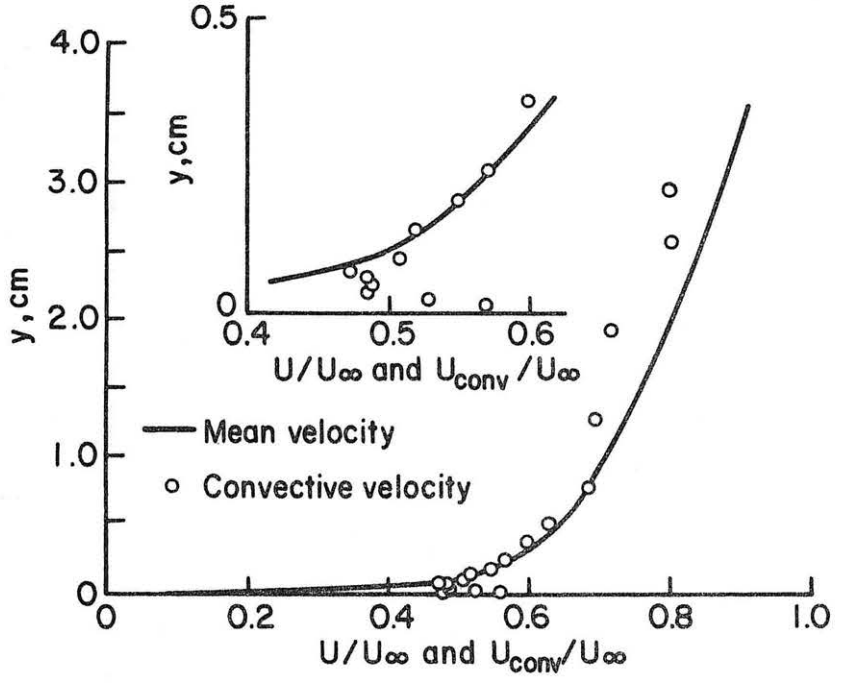

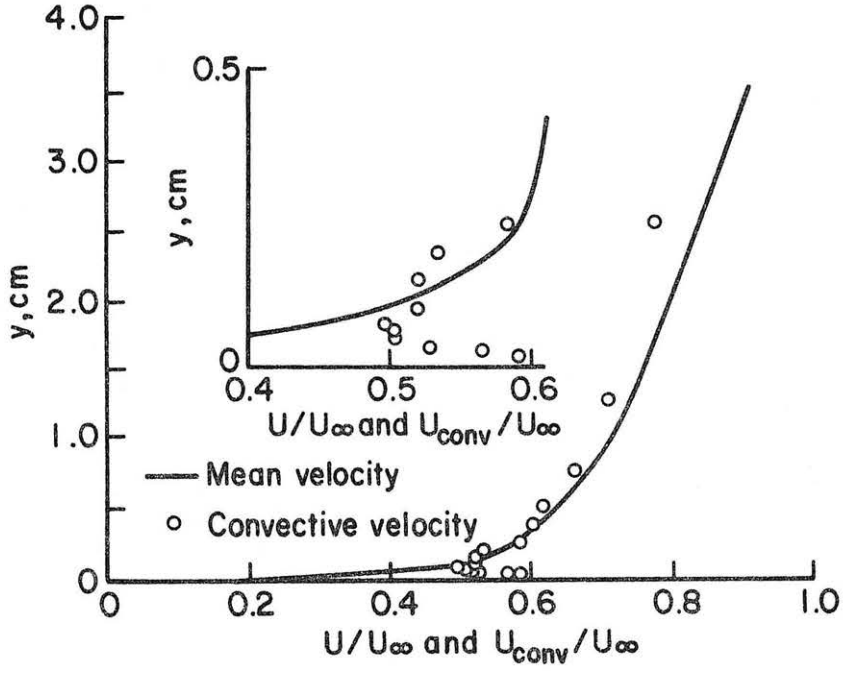

Figure 26. Comparison of mean-velocity and convective-velocity profiles.
a) For U_∞ = 10.20 m/sec.
b) For U_∞ = 8.55 m/sec.

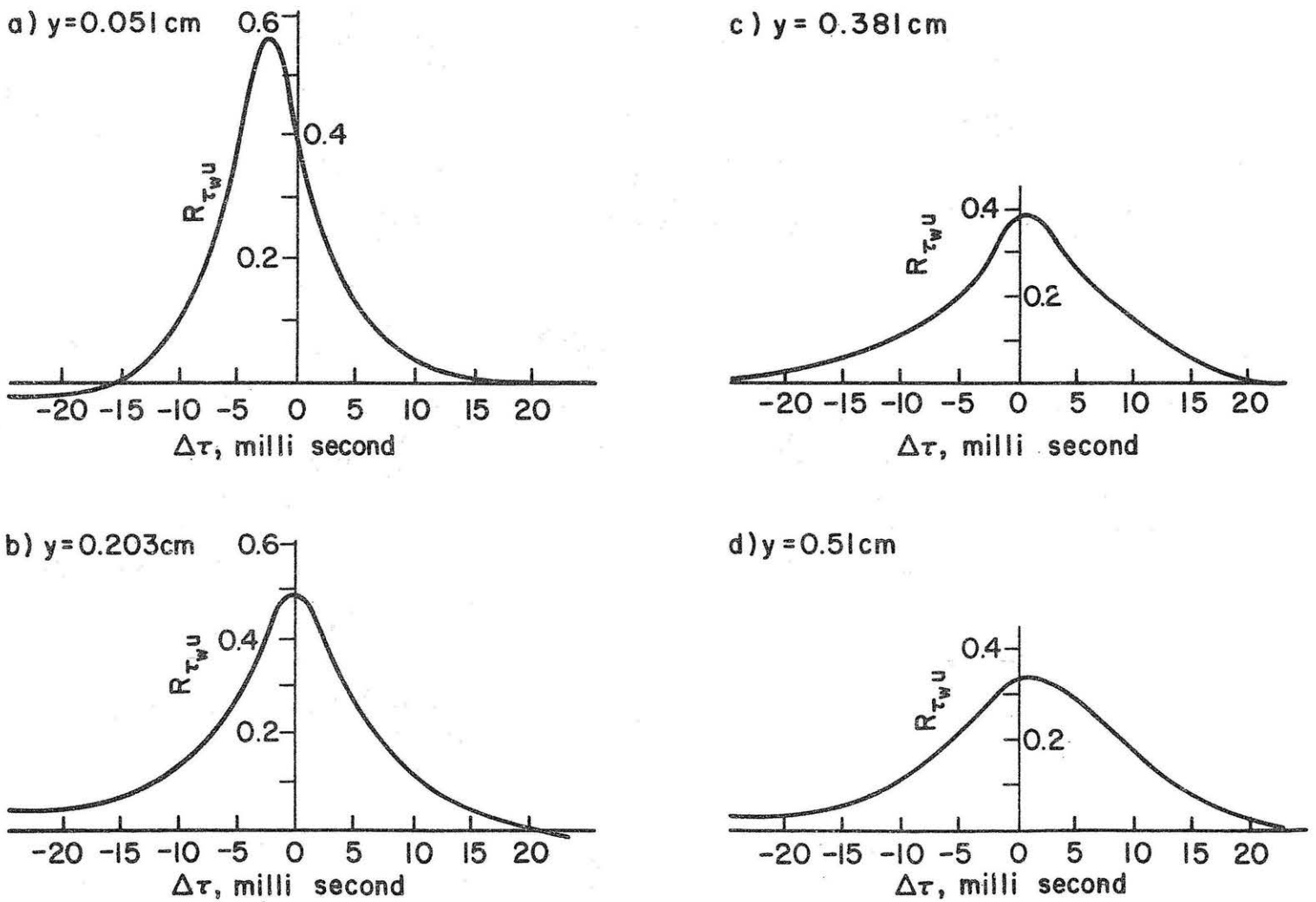

Figure 27. Cross-correlation curves measured at several heights for x = -1.5 cm, z = 0.0 cm.

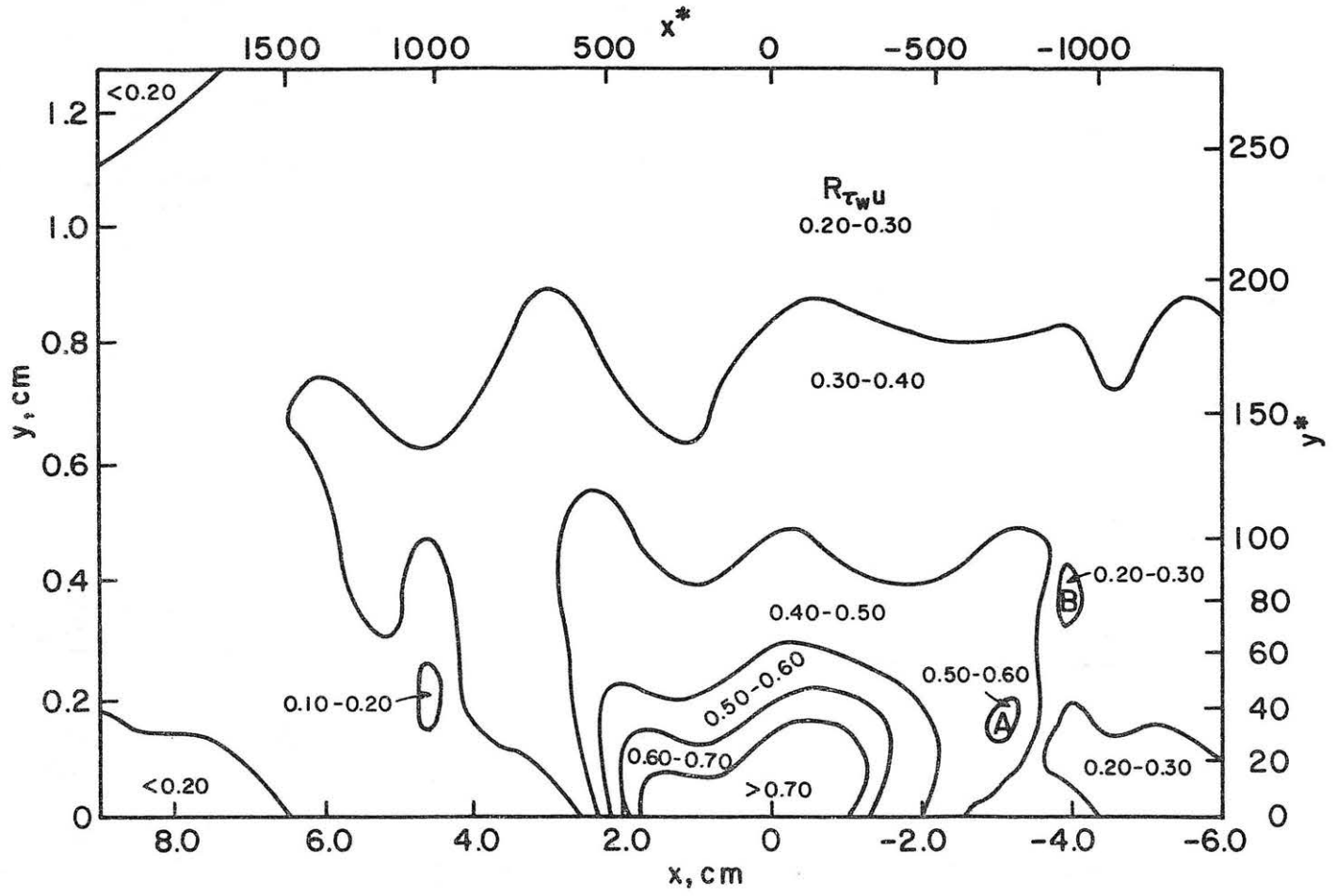

Figure 28a. Peak isocorrelation curves from the correlation of the boundary layer hot wire and the surface hot wire signals; freestream velocity 10.20 m/sec.

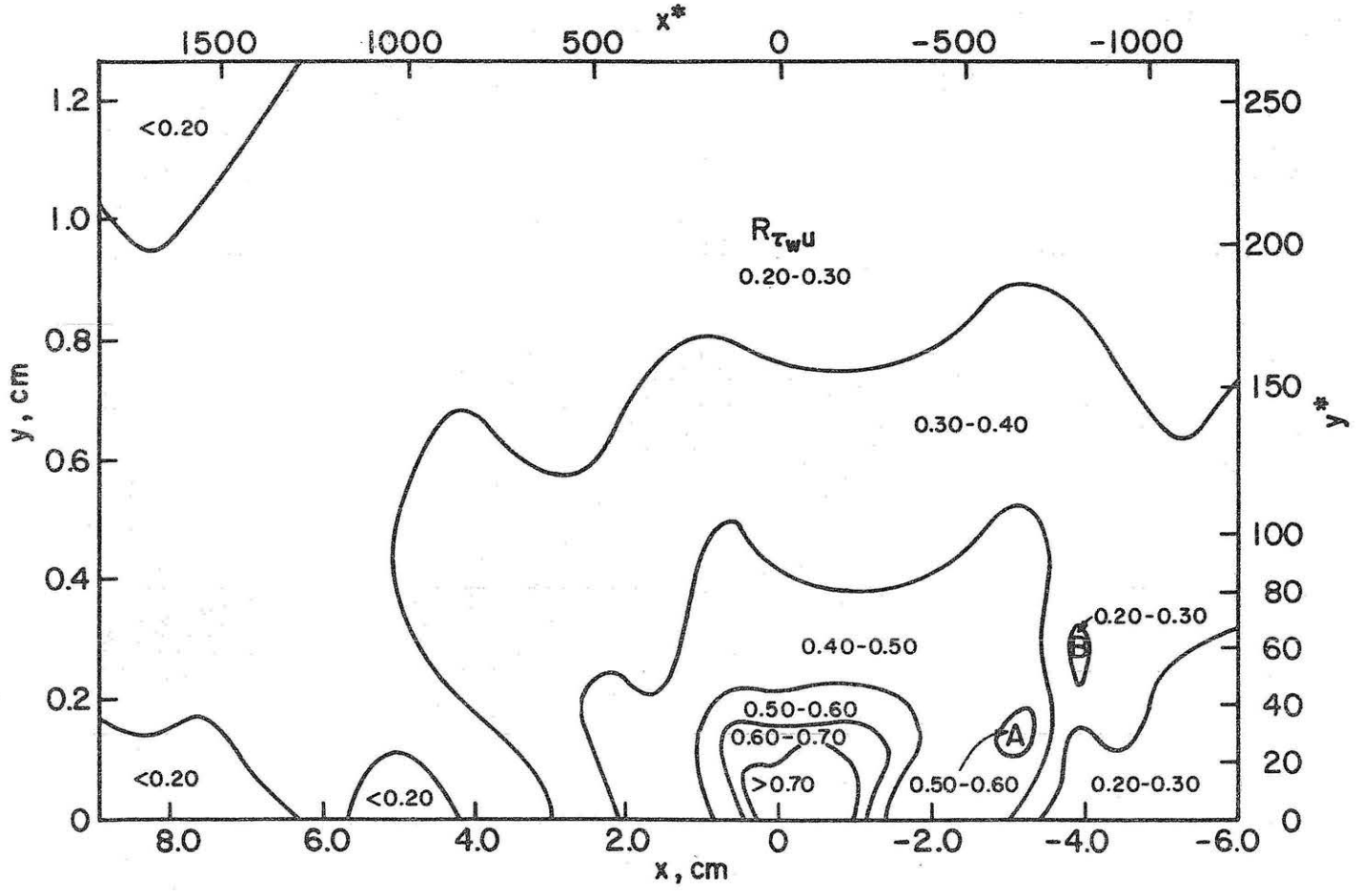

Figure 28b. Peak isocorrelation curves from the correlation of the boundary layer hot wire and the surface hot wire signals; freestream velocity 9.36 m/sec.

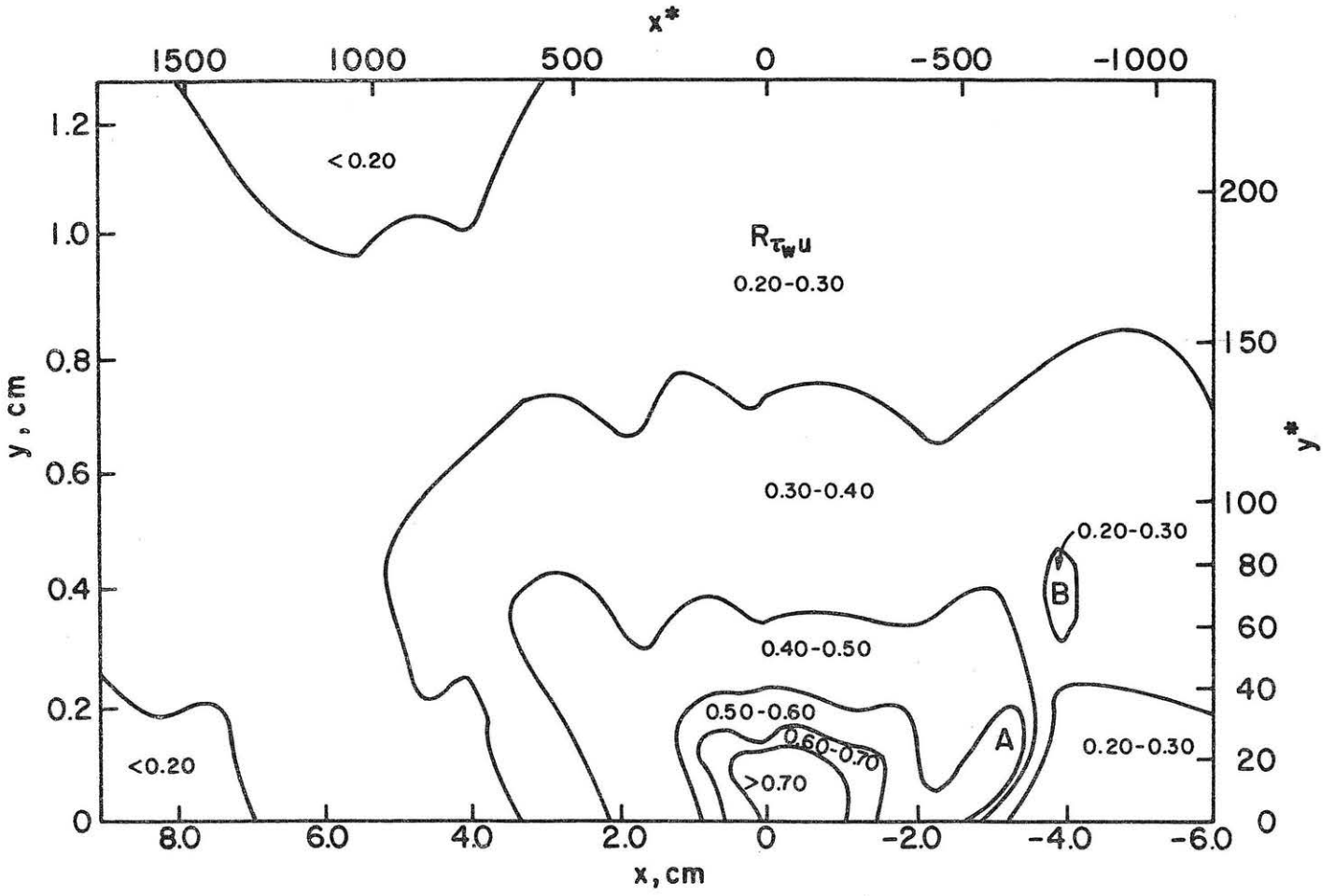

Figure 28c. Peak isocorrelation curves from the correlation of the boundary layer hot wire and the surface hot wire signals; freestream velocity 8.55 m/sec.

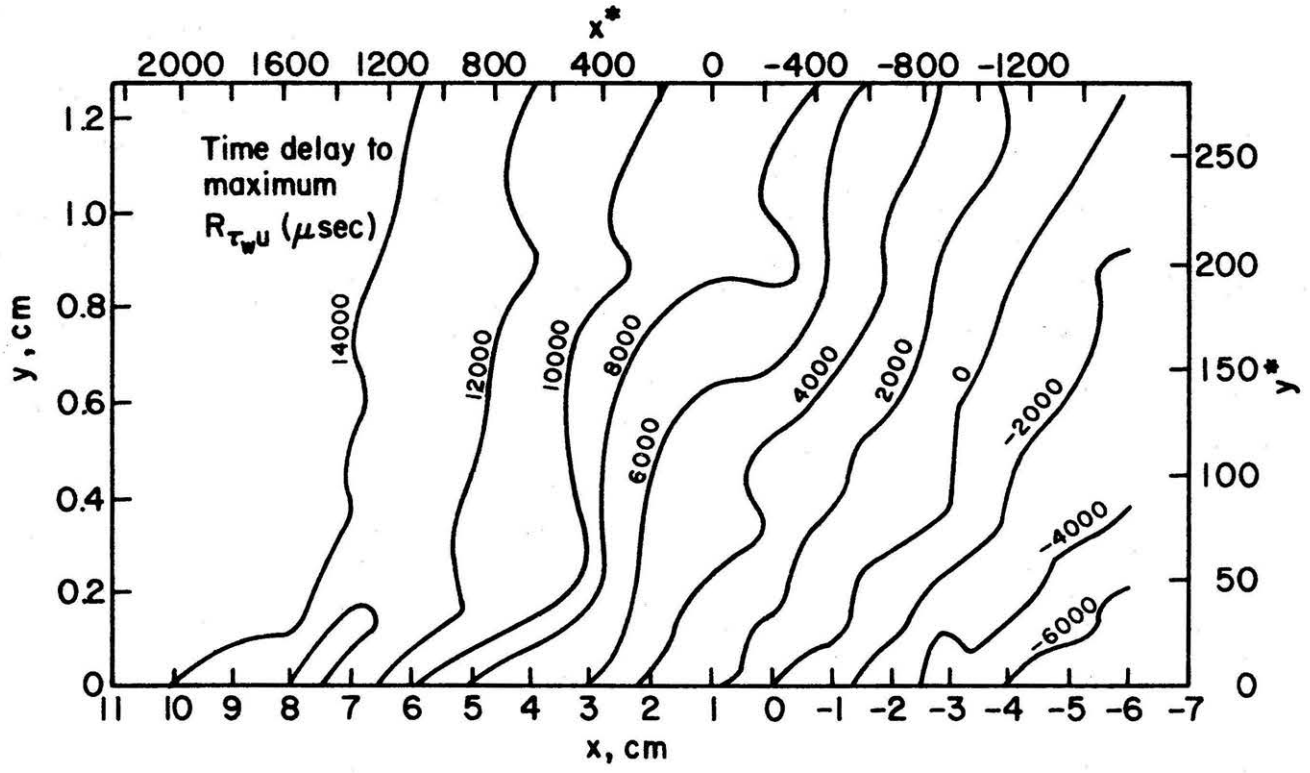

Figure 29a. Peak time delay lines for the correlation between a boundary layer hot wire and the surface hot wire signals; freestream velocity 10.2 m/sec.

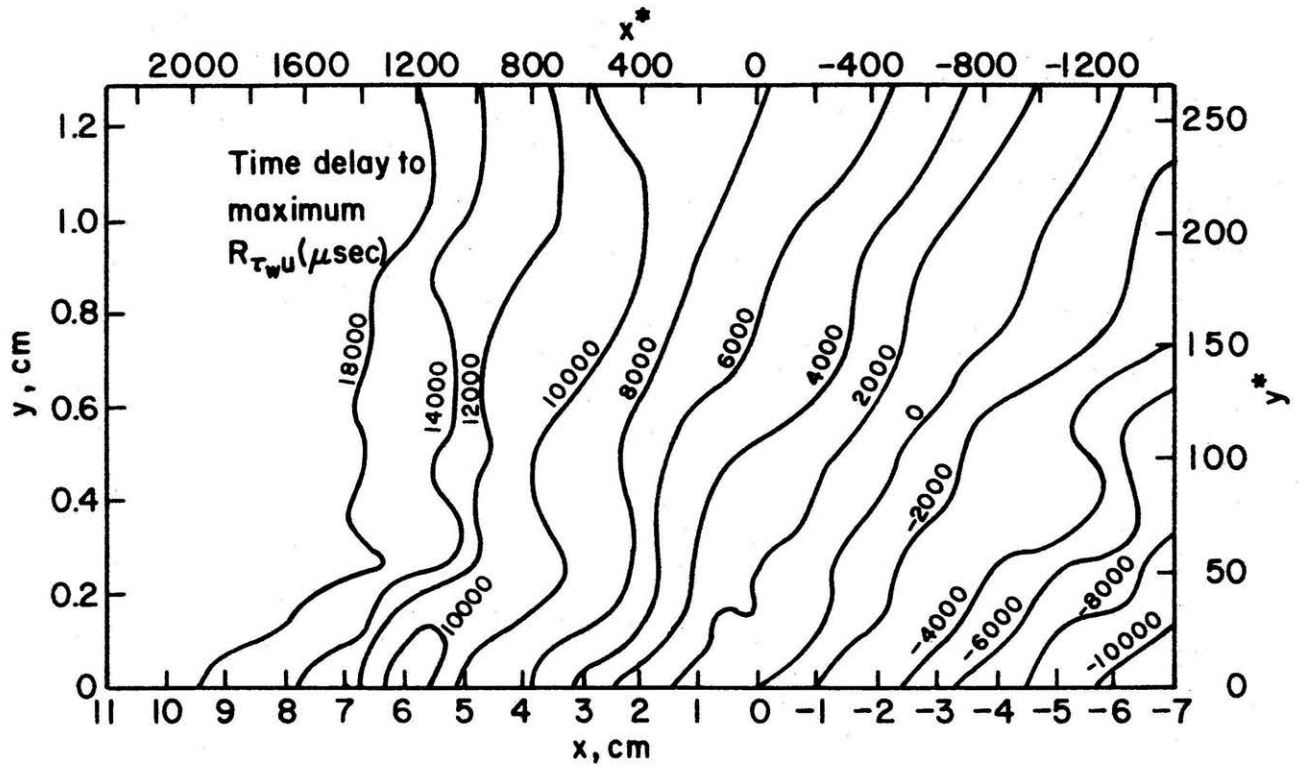

Figure 29b. Peak time delay lines for the correlation between a boundary layer hot wire and the surface hot wire signals; freestream velocity 9.36 m/sec.

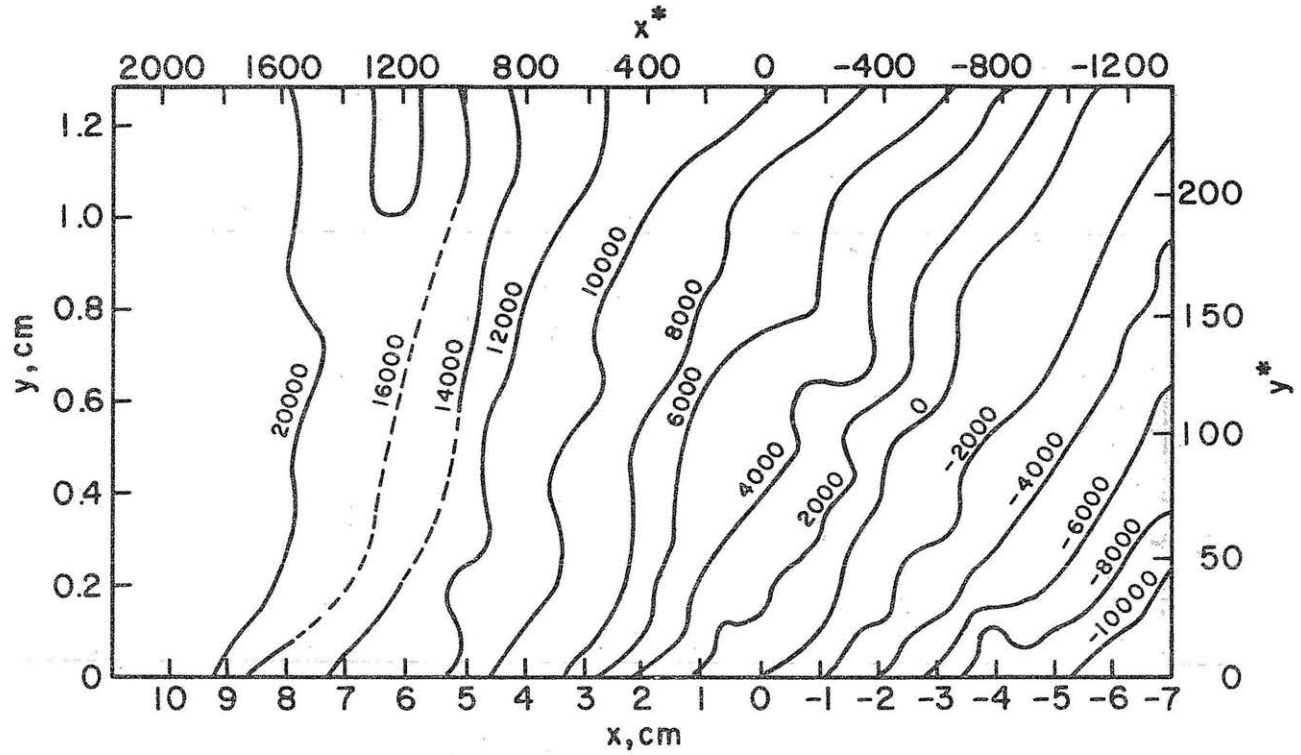

Figure 29c. Peak time delay lines for the correlation between a boundary layer hot wire and the surface hot wire signals; freestream velocity 8.55 m/sec.

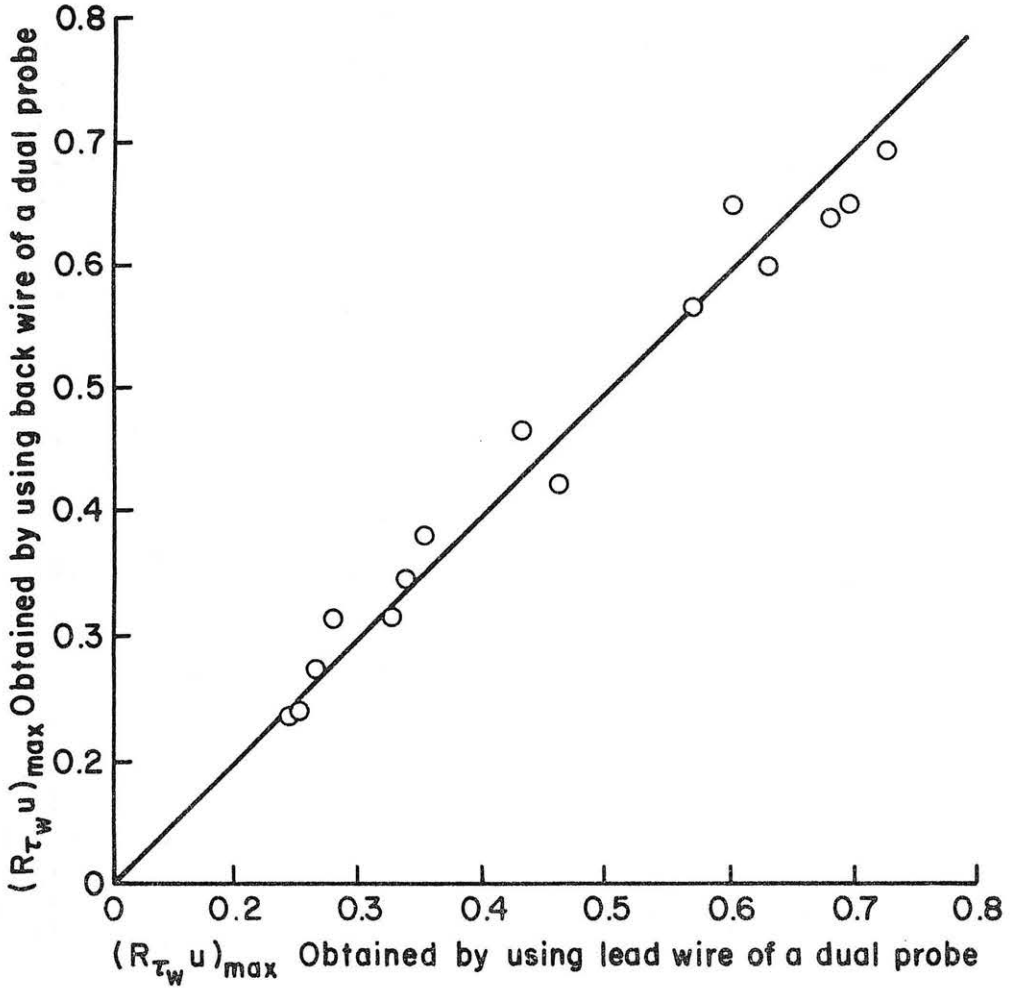

Figure 30. Repeatability of the maximum correlation $(R_{\tau_w u})_{max}$ evaluation.

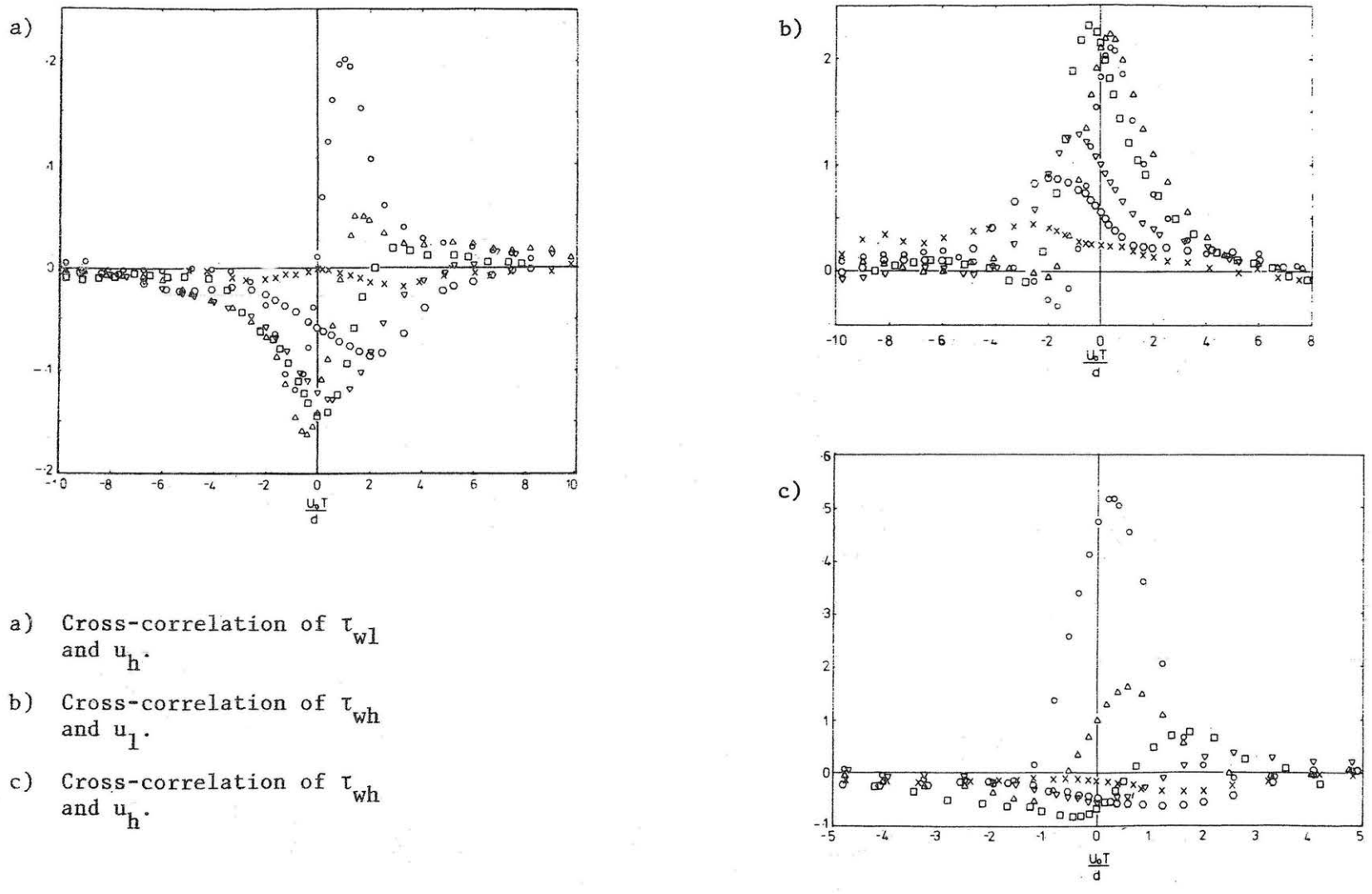

a) Cross-correlation of τ_{wl} and u_h.

b) Cross-correlation of τ_{wh} and u_l.

c) Cross-correlation of τ_{wh} and u_h.

Figure 31. Space-time correlation of surface shear stress and velocity fluctuations reported by Rajapopalan and Antonia (1980.

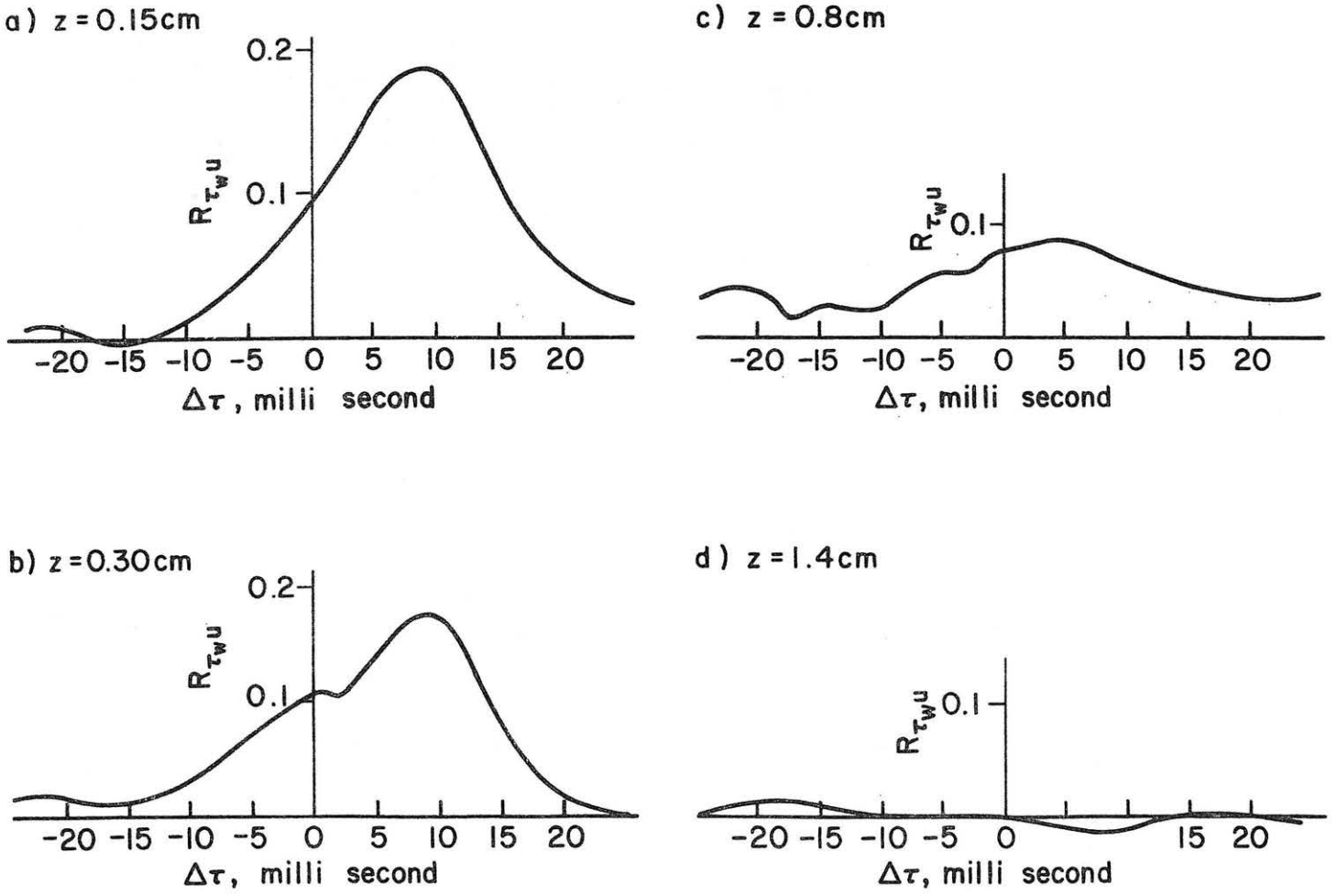

Figure 32. Cross-correlations measured at several lateral positions for x = 5.0 cm, y = 0.127 cm.

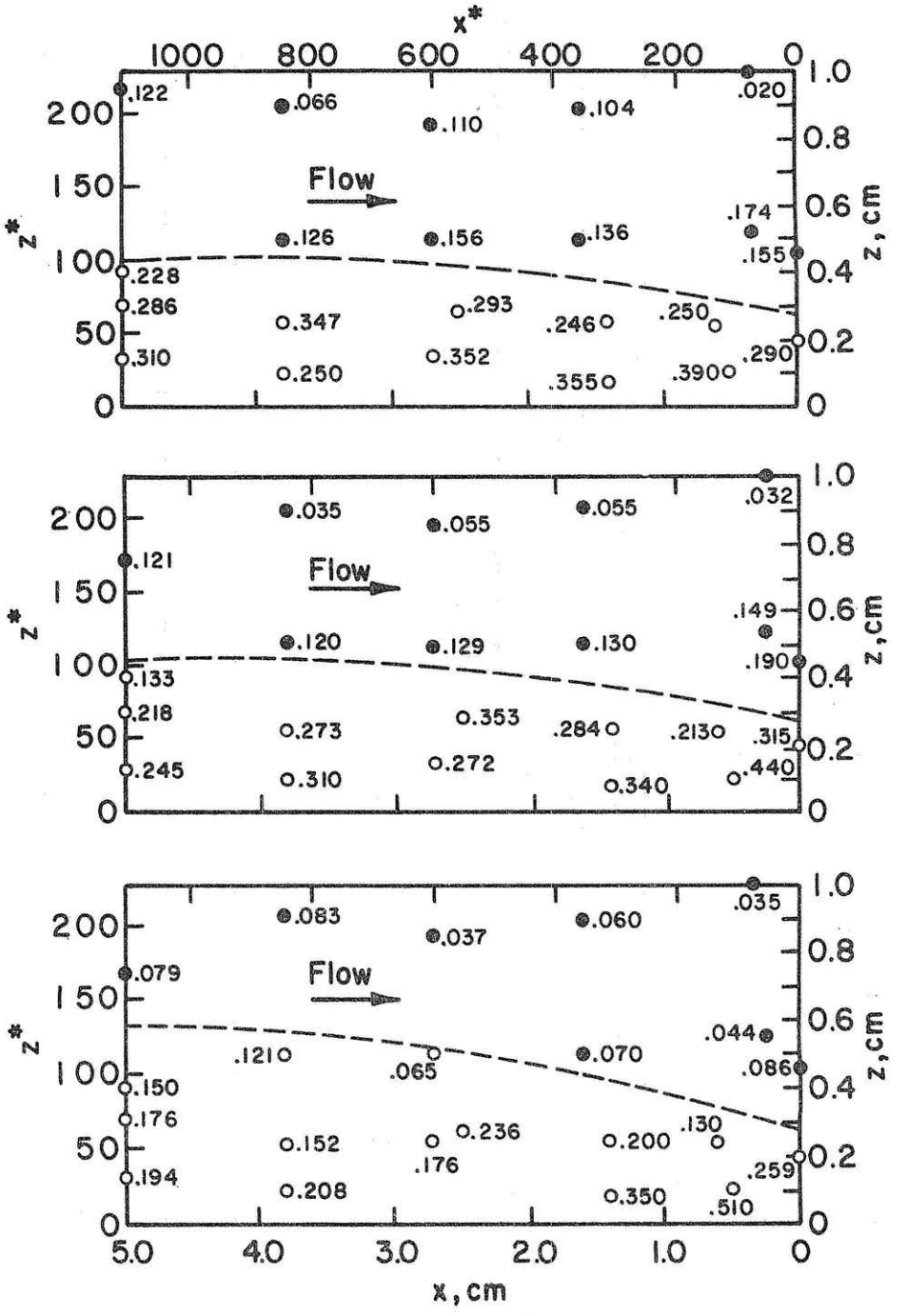

Figure 33. Measured values of $(R_{\tau_w u})_{max}$ in the lateral direction.

Solid circles and open circles represent multimaximum and single maximum points respectively.

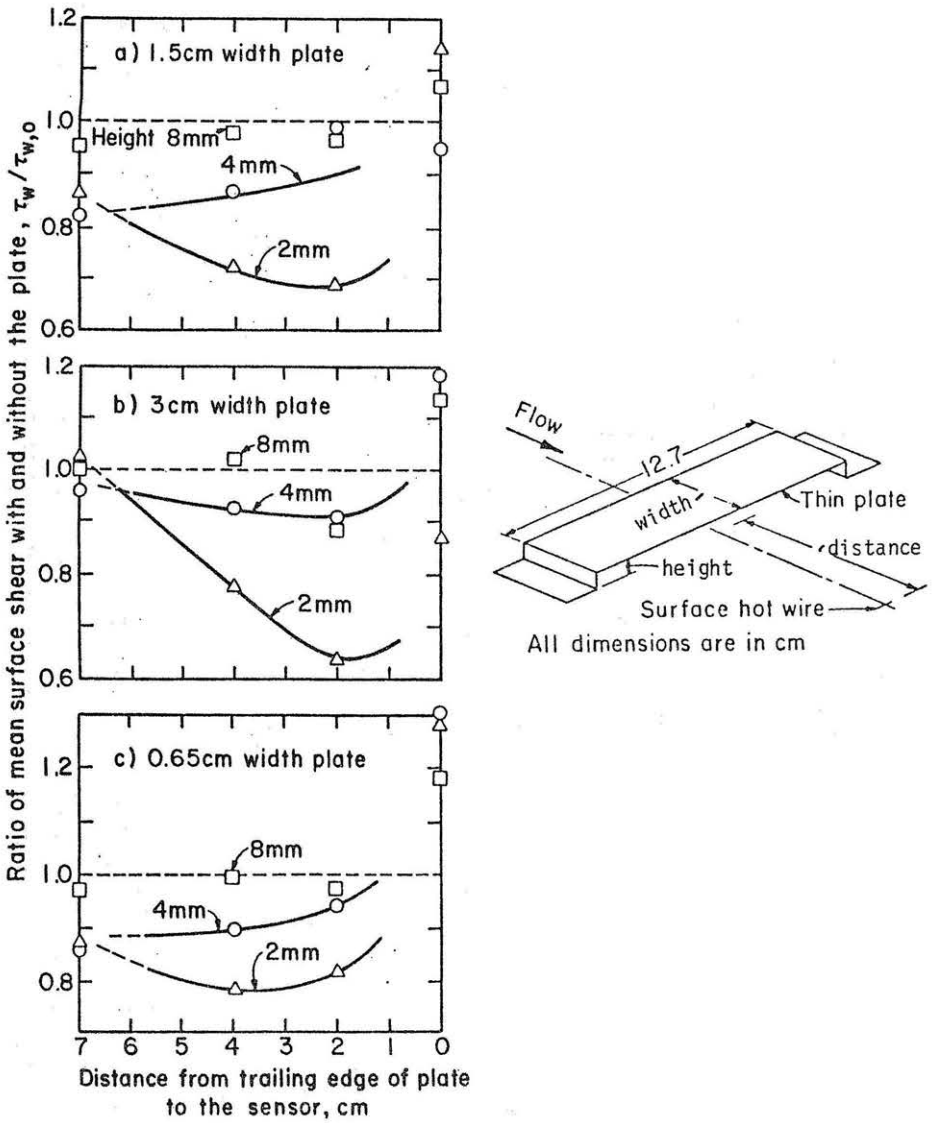

Figure 34. Measured reduction of surface shear stress for different sizes and locations of the thin metal plate.

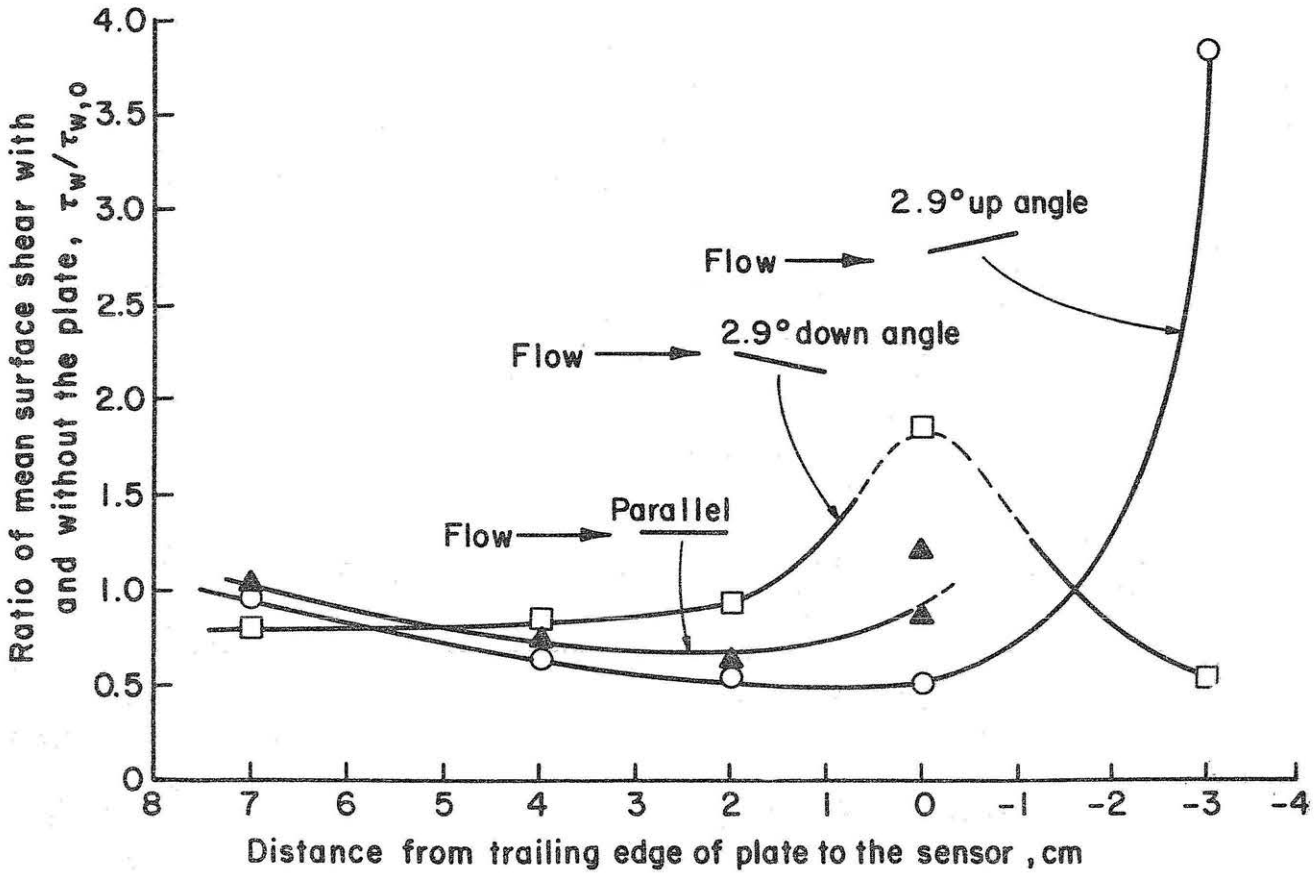

Figure 35. Effect of slight angle of attack of the plates on the surface shear stress. 3 cm wide plate, 2 mm height above the surface.

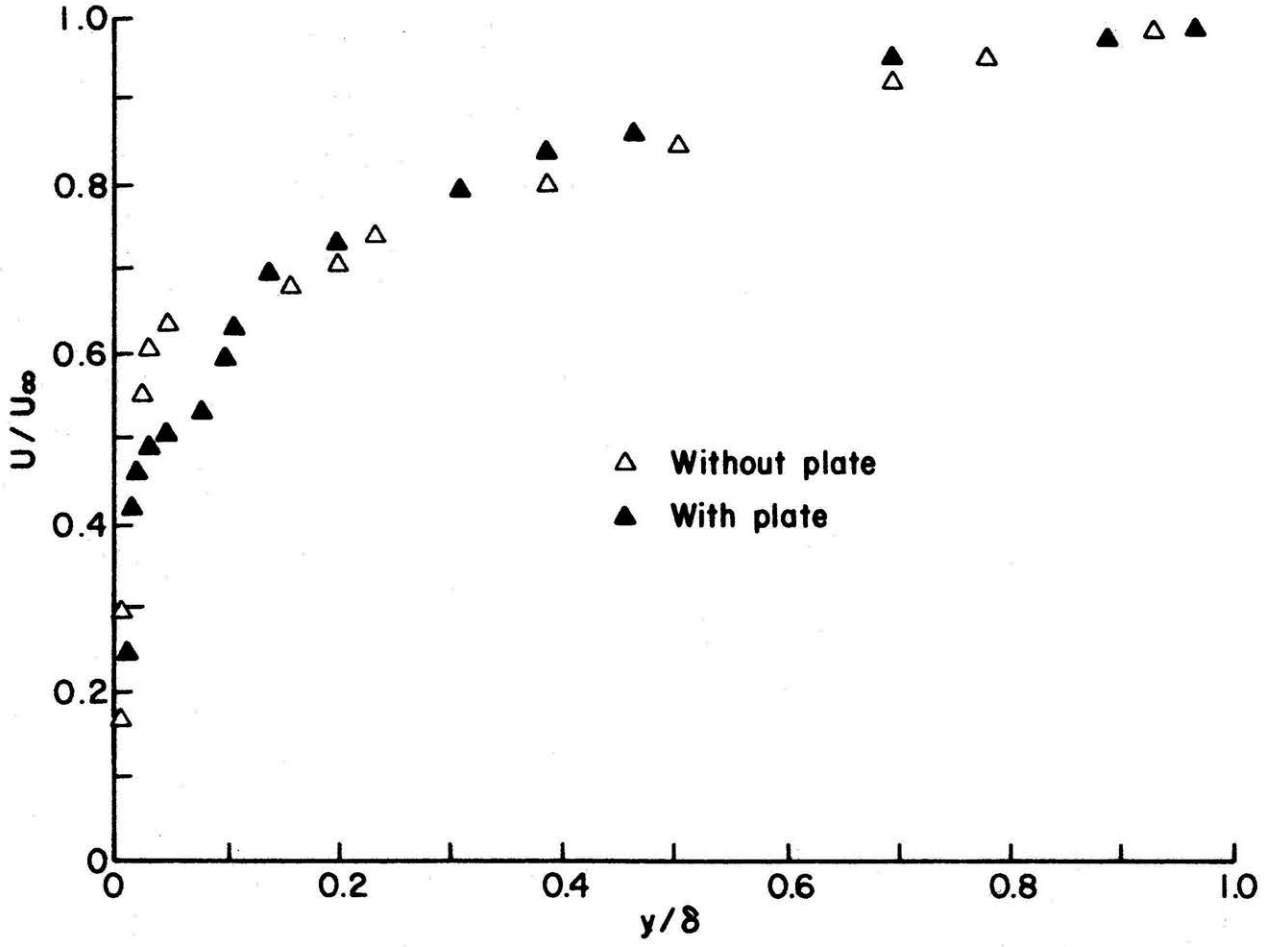

Figure 36. Velocity profiles measured with and without the thin plate placed upstream.

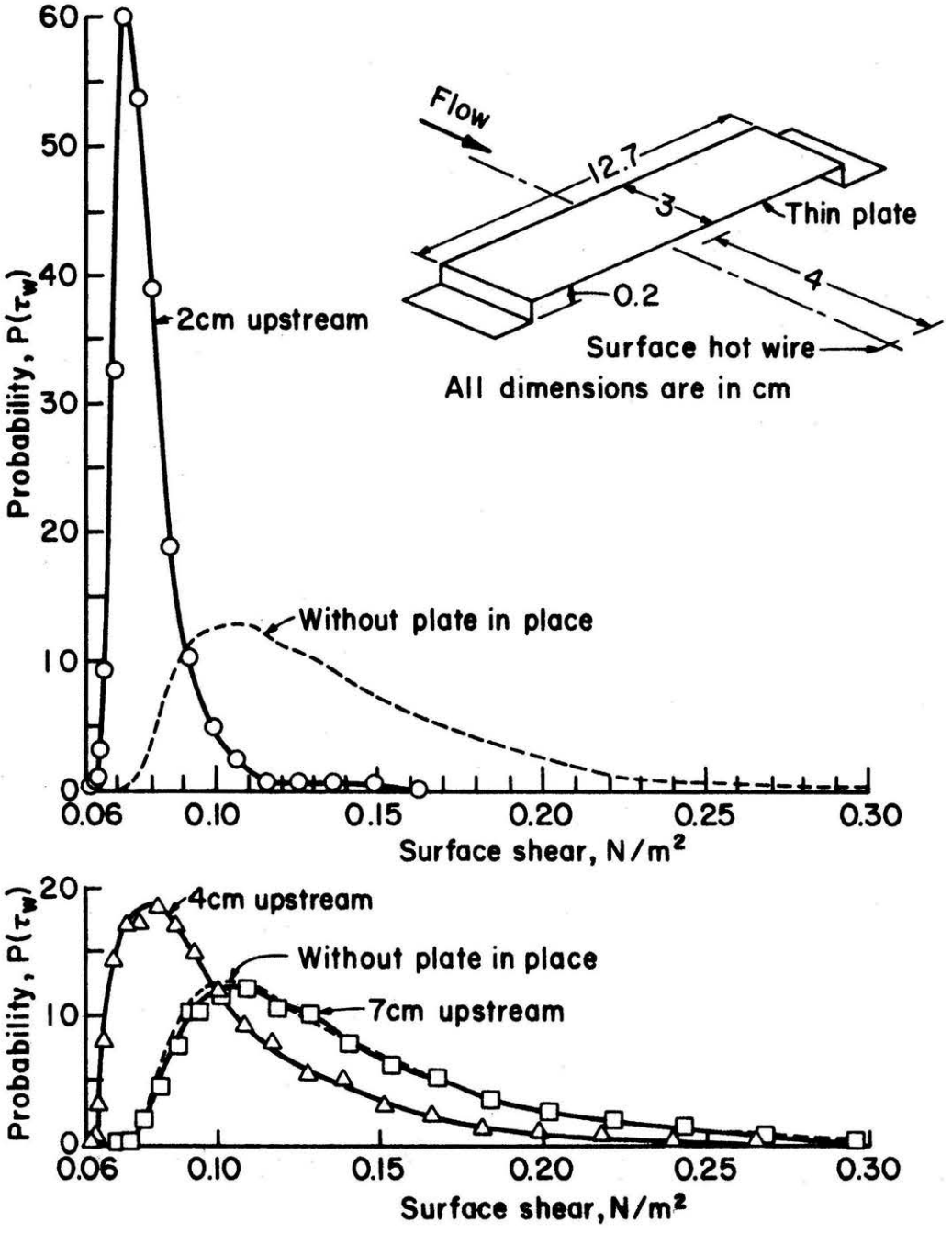

Figure 37. Probability distribution of surface shear stress due to a 3 cm wide plate placed at a height of 2 mm above the surface.

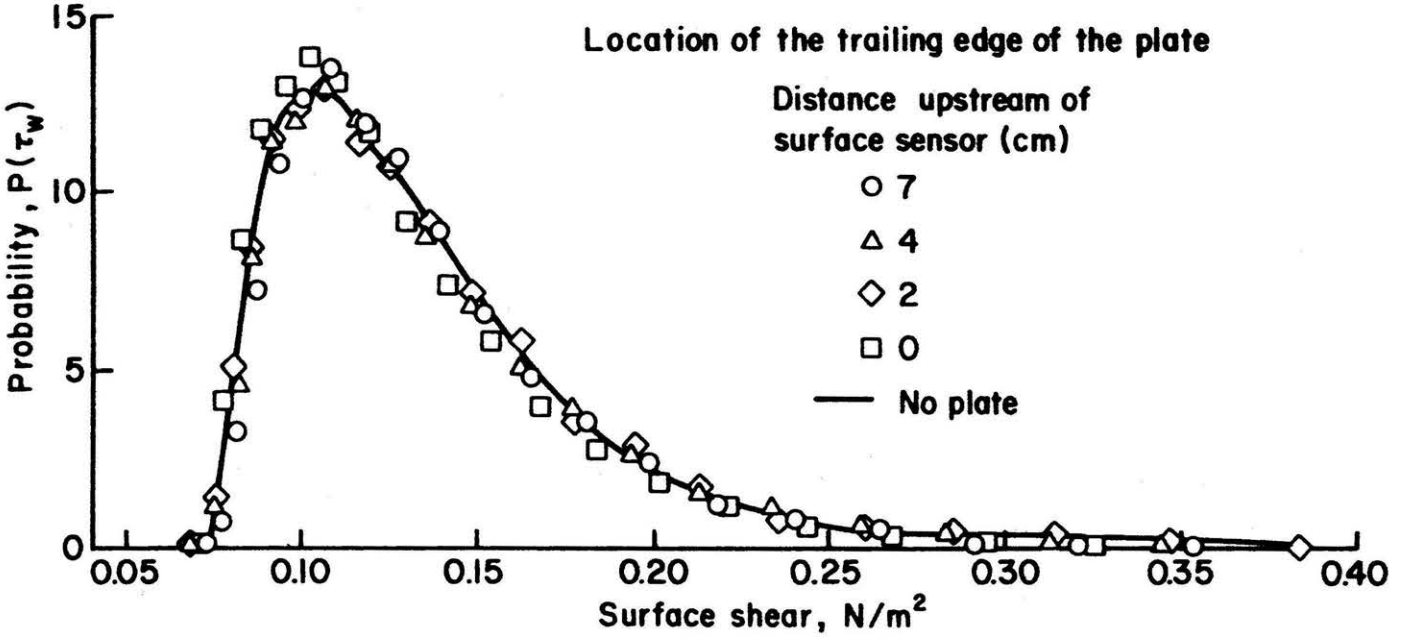

Figure 38. Probability distributions measured with a thin plate placed in the boundary layer 8 mm ($y^* \simeq 160$) above the surface.